CRUSTAL AND UPPER MANTLE STRUCTURE BENEATH THE GALÁPAGOS ARCHIPELAGO FROM SEISMIC TOMOGRAPHY

by

DARWIN R. VILLAGÓMEZ DÍAZ

A DISSERTATION

Presented to the Department of Geological Sciences
and the Graduate School of the University of Oregon
in partial fulfillment of the requirements
for the degree of
Doctor of Philosophy

December 2010

DISSERTATION APPROVAL PAGE

Student: Darwin R. Villagómez Díaz

Title: Crustal and Upper Mantle Structure Beneath the Galápagos Archipelago from Seismic Tomography

This dissertation has been accepted and approved in partial fulfillment of the requirements for the Doctor of Philosophy degree in the Department of Geological Sciences by:

Dr. Douglas R. Toomey	Chairperson
Dr. Eugene Humphreys	Member
Dr. Emilie Hooft Toomey	Member
Dr. Paul Wallace	Member
Dr. John Conery	Outside Member

and

Richard Linton	Vice President for Research and Graduate Studies/Dean of the Graduate School

Original approval signatures are on file with the University of Oregon Graduate School.

Degree awarded December 2010

DISSERTATION ABSTRACT

Darwin R. Villagómez Díaz

Doctor of Philosophy

Department of Geological Sciences

December 2010

Title: Crustal and Upper Mantle Structure Beneath the Galápagos Archipelago from Seismic Tomography

Approved: _____
Douglas R. Toomey

To explain the origin of several distinct aspects of the Galápagos volcanic hotspot, such as the broad geographical extent of recent volcanism and the unusual pattern of geochemical anomalies, we conducted seismic tomography studies of the upper mantle and crust beneath the Galápagos Archipelago. The studies combine measurements of group and phase velocities of surface waves and delay times of body waves. We find that upper mantle seismic velocities are lower than those beneath other regions of comparable age in the Pacific and consistent with an excess temperature of 30 to 150°C and ~0.5% melt. We attribute the excess temperature and presence of melt to an upwelling thermal mantle plume. Crustal seismic velocity is up to 25% lower than that of very young crust at the East Pacific Rise (EPR) and is comparable to that of Hawaii, which we attribute to heating by increased intrusive activity above the Galápagos plume and the construction of a highly porous volcanic platform. In addition, we find that the Galápagos hotspot is underlain by a high-velocity region whose thickness varies from 40 to 100 km. The tomographic images reveal that the upwelling mantle plume tilts

northward (towards the nearby Galápagos Spreading Center) as it rises and then spreads laterally when it reaches the bottom the lid. The lid, which we attribute to residuum from melting, is thickest where it is farthest from the spreading center, suggesting that ridge processes may affect the generation and amount of thinning of the residuum layer. In addition, the thickness of the lid correlates well with the geographical pattern of geochemical anomalies of erupted lavas, suggesting that the lid may control the final depth of decompression melting. We conclude that many of the distinct characteristics of the Galápagos can be attributed to the interaction of the upwelling plume with the lid and the nearby ridge. We further suggest that the ridge affects the geometry of plume upwelling in the upper mantle and also the pattern of lateral spreading of the plume due to its effect on the thickness of the residuum layer.

This dissertation includes previously published co-authored material.

CURRICULUM VITAE

NAME OF AUTHOR: Darwin R. Villagómez Díaz

GRADUATE AND UNDERGRADUATE SCHOOLS ATTENDED:

University of Oregon, Eugene
Escuela Politecnica Nacional, Quito, Ecuador

DEGREES AWARDED:

Doctor of Philosophy, 2010, Geological Sciences, University of Oregon
Engineer, Geology, 2000, Escuela Politecnica Nacional

AREAS OF SPECIAL INTEREST:

Seismic Tomography

PROFESSIONAL EXPERIENCE:

Senior Scientist, ID Analytics, San Diego, CA, 2007-2010

Teaching and Research Assistant, University of Oregon, Eugene, 2000-2007

Research Assistant, Instituto Geofisico, Quito, Ecuador, 1995-2000

GRANTS, AWARDS, AND HONORS:

Graduate Teaching Fellowship, Geology, 2000-2007

PUBLICATIONS:

Villagómez D., Toomey D., Hooft E., Solomon S. (2007) Upper mantle structure beneath the Galápagos from surface wave tomography, Journal of Geophysical Research, 112, B07303

ACKNOWLEDGMENTS

I thank Professors Douglas Toomey and Emilie Hooft Toomey for guidance and support. This research was supported by the National Science Foundation under grants OCE-9908695, OCE-0221549, and EAR-0651123 to the University of Oregon and OCE-0221634 to the Carnegie Institution of Washington.

For Caroline, who taught me about love and perseverance, and my children, Alex and Maya, who inspire me every day.

TABLE OF CONTENTS

Chapter Page

I. INTRODUCTION 1

II. UPPER MANTLE STRUCTURE BENEATH THE GALÁPAGOS ARCHIPELAGO FROM SURFACE WAVE TOMOGRAPHY 7

2.1. Introduction 7

2.2. Method 9

2.2.1. Imaging of Phase Velocity 9

2.2.2. Inversion for V_S 14

2.3. Results 16

2.3.1. Validity of the Two-Plane-Wave Approximation 16

2.3.2. Phase Velocity Inversion 19

2.3.3. Shear Wave Velocity Inversion 27

2.3.4. Model Resolution 37

2.3.5. Synthetic Inversions and Model Resolution 37

2.4. Properties of the Upper Mantle 43

2.4.1. Properties at 75-150 km Depth 43

2.4.1.1. Effect of Temperature 44

2.4.1.2. Effect of Melt Fraction 49

2.4.2. Porous Flow Model 51

2.4.3. Properties at Less Than 75 km Depth 52

2.5. Discussion 55

2.5.1. A Plume in the Shallow Upper Mantle 55

Chapter Page

2.5.2. The High-Velocity Lid 57

2.5.3. Gravitational Spreading of the Plume 58

III. CRUSTAL STRUCTURE BENEATH THE GALÁPAGOS ARCHIPELAGO FROM AMBIENT NOISE TOMOGRAPHY AND ITS IMPLICATIONS FOR PLUME-LITHOSPHERE INTERACTIONS 61

3.1. Introduction 61

3.2. Data and Methods 62

3.2.1. Imaging of Rayleigh-Wave Group Velocity 62

3.2.2. Inversion for Shear-Wave Velocity Structure 66

3.3. Results 68

3.3.1. Estimation of Group Velocity 68

3.3.2. Inversions for V_S 83

3.4. Discussion 92

3.4.1. Crustal Structure 92

3.4.2. Lithospheric Strength 98

3.4.3. Plume-lithosphere Interactions 101

IV. UPPER MANTLE JOINT INVERSION OF BODY AND SURFACE WAVES 107

4.1. Introduction 107

4.2. Tomographic Method 108

4.2.1. Forward Problem 109

4.2.2. Inverse Problem 110

Chapter Page

4.3. Synthetic Inversions of S-wave Slowness Perturbations 116

4.4. Results 118

4.4.1. Body Wave Delay Time Measurement 118

4.4.2. Phase Velocity Measurement and Inversion for Absolute V_S 121

4.4.3. Joint Inversions for Slowness Perturbations 125

4.5. Discussion 131

V. CONCLUSIONS 136

5.1. Crustal Structure between 3 and 13 km Depth 136

5.2. Mantle Structure between 20 and 300 km Depth 138

REFERENCES CITED 140

LIST OF FIGURES

Figure Page

1.1. Map of the Galápagos Islands and Seismic Network 2

2.1. Azimuthal Distribution of the Events Analyzed 8

2.2. Vertical Seismograms for Station PAYG 11

2.3. Normalized Two-Dimensional Phase Sensitivity Kernels 13

2.4. Results from the Two-Plane-Wave Approximation and Polarization Analysis 18

2.5. Grid Node Parameterization Used in the Phase Velocity Inversions 20

2.6. Average Phase Velocity as a Function of Period 22

2.7. Results from Inversions with Azimuthal Anisotropy 25

2.8. Results of Inversion for Two-Dimensional Isotropic Phase Velocity 26

2.9. Results of Inversions for Shear Wave Velocity. 30

2.10. One-Dimensional V_S Models and E-W Cross-Sections of the 3-D V_S Model ... 32

2.11. Shear Wave Velocity at Depths of 30, 50, 70, 90, 110, and 130 km 32

2.12. E-W Cross-Sections Through Three-Dimensional V_S Model 36

2.13. Results of Synthetic Inversion for Phase Velocity 39

2.14. Map Views and E-W Cross-Sections of the Results of Synthetic Inversion 40

2.15. Resolution of V_S Inversion for a Grid Node Located at 90.9°W and 0.4°S 42

2.16. Comparison of 1-D V_S Models with Models Calculated Using the Methodology of Faul and Jackson (2005) 46

2.17. Best Fitting Potential Temperatures as a Function of Grain Size 48

2.18. Depth to 0% V_S Change Contour (Squares) along an E-W profile at 0.2°S 54

Figure Page

3.1. Cross-Correlations of 26 Days of Seismic Ambient Noise Records 71

3.2. Nominal Model for V_P and V_S versus Depth and Sensitivity of Rayleigh Wave Group Velocity to Changes in V_S 72

3.3. Results of Multiple Filter Analysis (MFA) 74

3.4. Cross-Correlations of Ambient Noise Records between G08 and PAYG 75

3.5. Average Dispersion Curve for the Entire Archipelago 76

3.6. Smoothed Dispersion Curves for Selected Station Pairs 77

3.7. Maps of Paths Along Which Velocity Measurements Were Determined 78

3.8. Results of Velocity Inversions When Region Is Divided into Two Blocks 80

3.9. Average Value of Rayleigh-Wave Group Velocity for Each Station 82

3.10. Results of Inversions for V_S of the Regional Average Group Velocity 84

3.11. Results of Inversions for V_S of Rayleigh-Wave Group Velocity for the Regional Average and Eastern and Western Archipelagos 86

3.12. Effect on the Group Velocity of Adding Column of Water to Top of Model 87

3.13. Summary of Inversions for V_S When Water Layer Is Taken into Account 90

3.14. Synthetic Inversions for V_S 91

3.15. Comparison of Crustal V_P Models beneath the Galápagos with Estimates Along EPR, Western Carnegie Ridge, Southern Hawaii and Oahu 93

3.16. Free-Air Gravity Anomaly in the Galápagos Region 99

3.17. Isochron Map 100

3.15. Comparison of the Thickness of the Lid of High Mantle Seismic Velocities with the Geographic Variation in the $^{87}Sr/^{86}Sr$ Ratio of Sampled Basalts 105

4.1. Synthetic Inversion for S-wave Slowness Perturbation 118

4.2. S-wave Seismic Rays in W-E Projection 119

Figure Page

4.3. Distribution of Relative Delay Times for P-Waves and S-Waves..... 120

4.4. Distribution of Piercing Points of Seismic Rays at Bottom of Model Grid..... 122

4.5. Two-Dimensional (2-D) Maps of Δc 123

4.6. Inversion for 1-D Absolute V_S 124

4.7. Results of Inversions for S-Wave Slowness Perturbations..... 128

4.8. Results of Inversions for P-Wave and S-Wave Slowness Perturbations 130

LIST OF TABLES

Table Page

2.1. Comparison of Phase Velocity Inversions 19

3.1. Time Periods Used for Cross-Correlation of Ambient Noise Records 70

3.2. RMS Misfit of Inversions for V_S 88

CHAPTER I

INTRODUCTION

Hotspot volcanism is widely thought to be the result of upwelling and melting of hot, buoyant mantle (Morgan, 1971). Gravity and topography observations of hotspot swells and results from modeling suggest that these mantle upwellings or plumes rise to the base of the lithosphere where they spread laterally (e.g., Ribe and Christensen, 1994; Feighner and Richards, 1995; Sleep, 1996). Some plumes interact with nearby spreading centers and produce physical and chemical anomalies along some 15-20% of the global mid-ocean ridge system, although the precise mechanism and depth of transport of plume material to mid-ocean ridges are still matters of debate (Ito et al., 2003, and references therein).

The Galápagos hotspot is an excellent setting to study the dynamics of the interaction among hotspots, the lithosphere, and a mid-ocean ridge, because of the proximity of the hotspot to the Galápagos Spreading Center (GSC). The Galápagos Archipelago, located in the equatorial east Pacific, sits 100-200 km south of the GSC. It consists of 10 major volcanic islands and 21 emergent volcanoes (Fig.1.1). The islands sit on a shallow and broad submarine platform (the Galápagos swell) that is elevated more than 2000 m above the surrounding ocean floor. An oceanic fracture zone crosses the northern part of the Galápagos near 91°W and creates a ~5-My lithospheric age offset, with thinner lithosphere beneath the eastern part of the archipelago. The hotspot sits on the Nazca plate, which moves eastward with respect to the hotspot, in a direction approximately perpendicular to the north-south (N-S) spreading of the GSC.

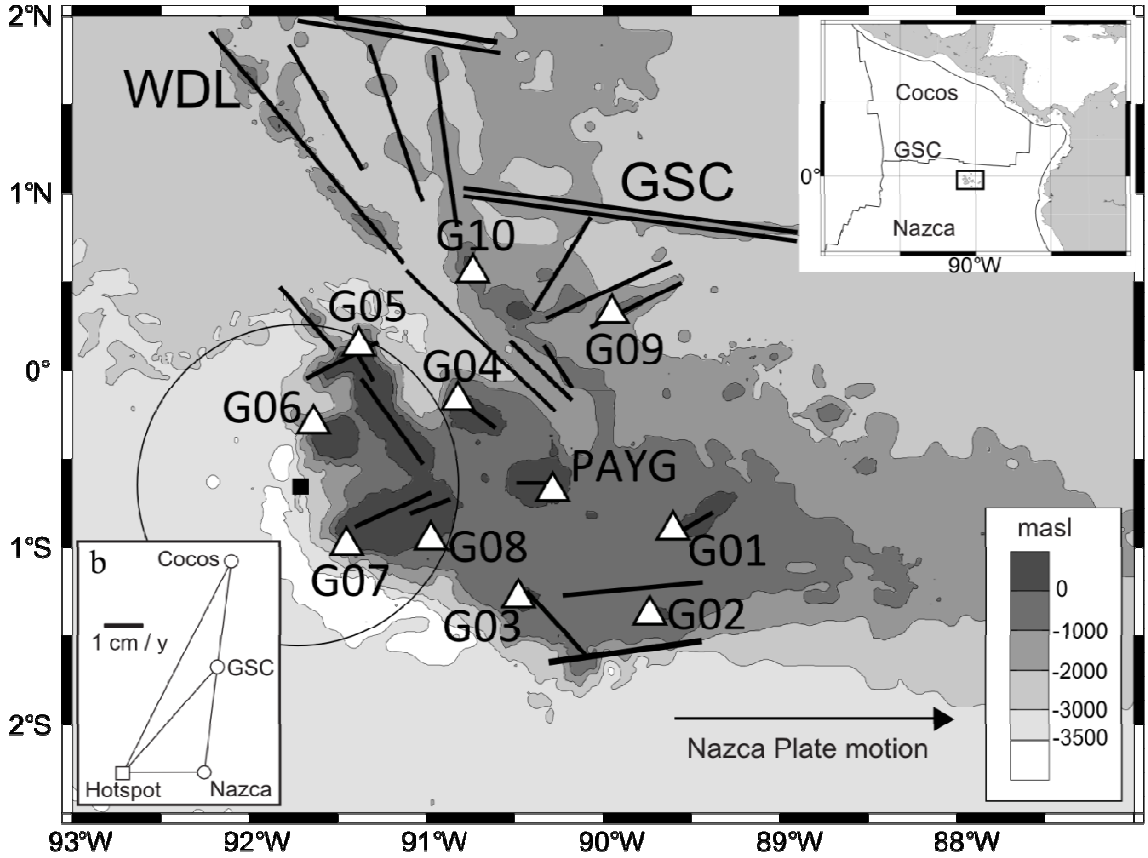

Fig. 1.1. (a) Map of the Galápagos Islands and seismic network. Triangles indicate seismic stations. The black square and solid circle with a 100-km radius indicate the approximate center and area of a region of anomalously thin mantle transition zone (Hooft et al., 2003). The black arrow indicates the direction of motion of the Nazca plate in a hotspot reference frame (Gripp and Gordon, 2002). Thick black lines show lineations and volcanic alignments from McBirney and Williams (1969), Feighner and Richards (1994), and Sinton et al. (2003). WDL is the Wolf-Darwin lineament. Bathymetry is from W. Chadwick (http://newport.pmel.noaa.gov/ ~chadwick/galapagos.html); 1000-m contour interval. (b) Vector velocities of plates and other features in the Galápagos region.

The Galápagos hotspot shares many of the characteristics of intraplate volcanic hotpots: (1) it is long-lived, with age estimates from ~20–22 Ma (Hey, 1977; Lonsdale and Klitgord, 1978) to 90 Ma (Hauff et al., 1997); (2) the composition and isotope ratios of the most recent lavas resemble those of other ocean island basalts (Geist et al., 1988; White et al., 1993); (3) two volcanic chains or hotspot trails, the Cocos and Carnegie

ridges, extend from the Galápagos in the directions of motion of the Cocos and Nazca plates, and (4) the seamounts of the Galápagos platform, and the Carnegie and Cocos ridges, generally increase in age with distance from the western edge of the archipelago (*Sinton et al.*, 1996; *Werner et al.*, 1999; *Hoernle et al.*, 2002). Moreover, seismic studies have resolved anomalously low seismic velocities indicative of higher than normal temperatures in the upper mantle beneath the western archipelago (Toomey et al., 2002; Hooft et al., 2003; Villagómez et al., 2007). The plume hypothesis (Morgan, 1972) successfully explains these observations.

Evidence of a plume origin for the Galápagos hotspot also includes basalts enriched in incompatible elements (e.g., higher $^{3}He/^{4}He$ and $^{87}Sr/^{86}Sr$ and lower $^{143}Nd/^{144}Nd$) (White and Hofmann, 1978; Geist et al., 1988; White et al., 1993; Kurz and Geist, 1999; Harpp and White, 2001), a general progression of the age of volcanism away from the hotspot in the direction of plate motion (McBirney and Williams, 1969; Sinton et al., 1996), and seismic images of anomalous upper mantle structure. Hooft et al. (2003) used receiver functions to show that the 410-km mantle discontinuity is deflected downward within an area approximately 100 km in radius centered beneath the southwestern corner of the archipelago (Fig. 1.1). This anomaly reflects higher temperatures (130±60 K) across that phase transition, consistent with upwelling from depths greater than 410 km (Hooft et al., 2003). Above the downward-deflected 410-km discontinuity, body wave tomography resolves low seismic velocities at depths of 50-250 km, consistent with upwelling of anomalously hot mantle (Toomey et al., 2002a).

However, two characteristics of the Galápagos archipelago suggest that the hotspot differs from otherwise similar features. First, the Galápagos hotspot includes a

spatially broad distribution of active volcanic centers (McBirney and Williams, 1969). Nine volcanoes have been active historically, and an additional four have erupted in the Holocene (White et al., 1993). In contrast, there are only four active volcanoes associated with the Hawaiian hotspot, and only one at the Reunion hotspot. Second, recent lavas show a considerable range in composition. Lavas from the central and eastern parts of the archipelago tend to have more depleted trace-element and isotopic signatures, whereas lavas erupted from the western and southern periphery have more enriched signatures (Geist et al., 1988; White et al., 1993). This pattern correlates with volcano morphology. The western volcanoes are young, large, central shield volcanoes with well-developed calderas, while the eastern volcanoes are generally older and smaller (White et al., 1993). Another distinctive characteristic of the Galápagos is that some volcanic centers and seamounts are aligned mostly along northeast- and northwest-trending lineations (Darwin, 1860; McBirney and Williams, 1969) (Fig. 1.1).

Two general models of mantle upwelling for the Galápagos hotspot have been proposed. The first model is based on geochemical data from the archipelago and accounts for the Nazca plate moving eastward with respect to the hotspot. Richards and Griffiths (1989) and White at el. (1993) suggested that the particular spatial distribution of incompatible elements in the archipelago could be the result of thermal entrainment of depleted upper mantle, as a result of local convective overturn within the center of a deflected mantle upwelling or plume. In this view, the plume is deflected to the east in the shallow mantle in response to plate drag. However, this model does not take into account the observed geochemical and geophysical variations along the axis of the GSC. The second model is based on geodynamical modeling of hotspot-ridge interaction and

accounts for the effect of N-S sea-floor spreading (Ito et al., 1997). The model includes northward migration of the GSC relative to the hotspot but does not account for eastward Nazca plate motion. Hotspot-derived material is transported to the ridge symmetrically to the east and west, accounting for the symmetrical along-axis geochemical variations, but the model does not consider the asymmetrical geochemical patterns observed within the archipelago. To date, no model can account for all of the geophysical and geochemical observations at both the GSC and the Galápagos Archipelago.

To study the upper mantle and crustal seismic structure beneath the Galápagos and test models of plume-ridge-lithosphere interaction we conducted a broadband seismic experiment. Seismic stations were deployed on nine islands of the archipelago between September 1999 and March 2003. The network consisted of 10 portable broadband stations and the Global Seismographic Network station PAYG (Fig. 1.1). The station spacing was between 50 and 70 km. Three-component Streckeisen STS-2 sensors were used at all portable stations; two Guralp CMG-3ESP instruments were initially deployed but were replaced after the first year. Data loggers were PASSCAL-equivalent Reftek units recording continuously at 20 samples per second. The seismic network spanned an area approximately 200 km in diameter.

In this dissertation, we present the results of 3 different tomography studies of the crust and upper mantle beneath the Galápagos Archipelago. Taken together, these results image detailed seismic velocity structure between 3 and 300 km depth. The results presented in this dissertation are organized in the following manner:

1) Chapter II presents the methods, results and implications of a Rayleigh wave tomographic study of the uppermost mantle, from the bottom of the crust (~20 km

depth) to approximately 150 km depth. Data for this study consisted of phase and amplitude measurements of teleseismic Rayleigh waves at periods between 20 and 125 s. This chapter was co-authored by Doug Toomey, Emilie E.E. Hooft and Sean Solomon, and was published in the Journal of Geophysical Research as Villagómez et al. (2007).

2) Chapter III presents the method, results and implications of a high-frequency Rayleigh wave tomographic study of the crust from 3 to 13 km depth. Data for this study, which consisted of Rayleigh-wave group velocities between 3 and 10 s of period, were obtained from records of ambient seismic noise. This chapter was co-authored by Doug Toomey, Emilie E. E. Hooft and Sean Solomon, and has been accepted for publication in the Journal of Geophysical Research.

3) Chapter IV presents the method, results and implication of a joint tomographic study of body and Rayleigh waves from the bottom of the crust to 300 km depth. We present a novel approach to jointly invert body and surface waves observations. Data for this study consisted of the Rayleigh waves phase velocity measurements obtained in chapter 2, augmented with teleseismic body waves (P and S) relative delay time observations.

4) Chapter V summarizes the combined conclusions of the 3 different studies.

CHAPTER II

UPPER MANTLE STRUCTURE BENEATH THE GALÁPAGOS ARCHIPELAGO FROM SURFACE WAVE TOMOGRAPHY

This chapter was coauthored by Douglas R. Toomey, Emilie E.E. Hooft and Sean C. Solomon.

Villagómez D. R., D. R. Toomey, E. E. E. Hooft, and S. C. Solomon S. C. (2007), Upper mantle structure beneath the Galápagos Archipelago from surface wave tomography, J. Geophys. Res., 112, B07303.

2.1. Introduction

Although regional seismic tomography has provided compelling evidence for plume-like upwelling in the upper mantle (e.g., Granet et al., 1995; Wolfe et al., 1997; Ritter et al., 2001; Allen et al., 2002; Li and Detrick, 2003), the resolution of images of off-axis hotspots in the uppermost mantle has not been adequate to provide clear tests of models of plume spreading and plume-ridge interaction. To address these issues we present a surface wave tomographic study of the uppermost mantle beneath the Galápagos Archipelago. The main goal of our study is to characterize the upwelling, spreading, and melting of the shallow mantle beneath the Galápagos hotspot. The Galápagos Archipelago is an excellent setting to study the dynamics of the interaction among hotspots, the lithosphere, and a mid-ocean ridge, because of the proximity of the

hotspot to the Galápagos Spreading Center (GSC) and because the direction of plate drag over the hotspot (eastward) is approximately perpendicular to the relative spreading direction of the GSC (north-south).

For this study we use three-component recordings of Rayleigh waves generated by 186 teleseismic events with $M_S > 5.9$ at epicentral distances ranging between 40° and 140° (Fig. 2.1).

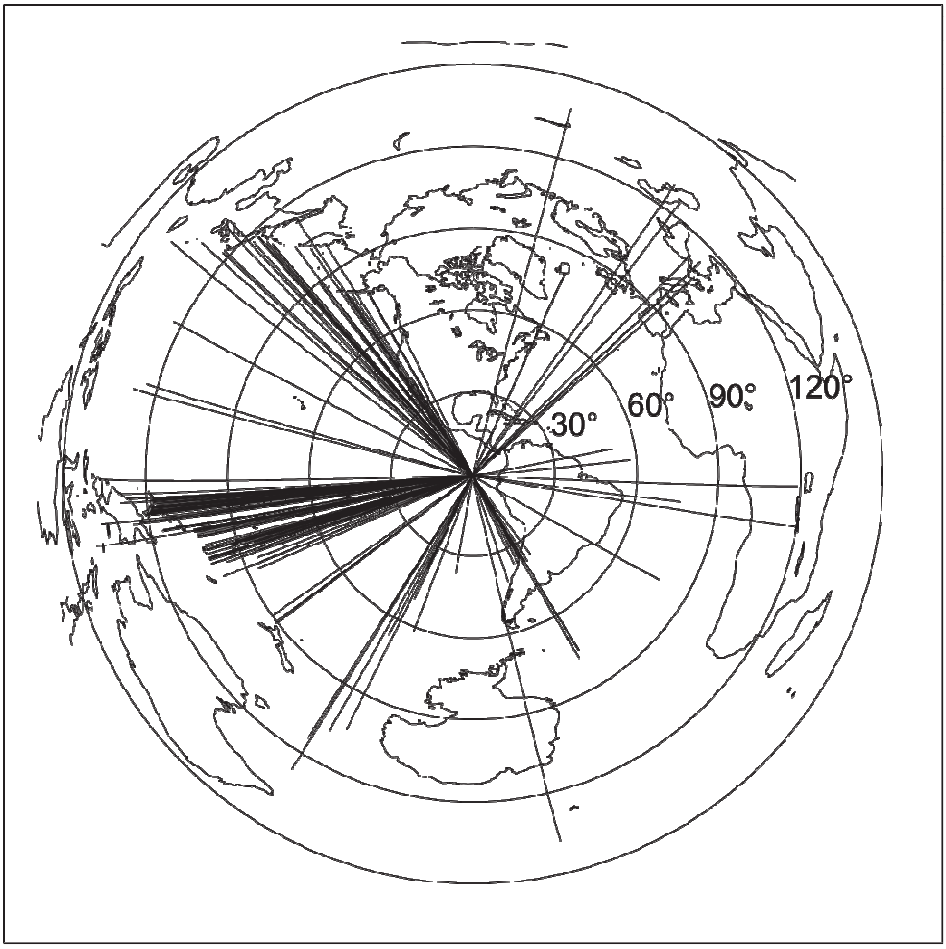

Fig. 2.1. Azimuthal distribution of the 189 events ($M_S > 5.9$) for which Rayleigh waves were analyzed in this study. Epicentral distance varies from 40° to 140°. Solid lines correspond to great circle paths. Azimuthal equidistant projection centered at 0°N, 90°W.

2.2. Method

2.2.1. Imaging of Phase Velocity

The seismic data are first used to derive one- and two-dimensional images of Rayleigh wave phase velocity. We obtain phase and amplitude information from the vertical-component seismograms. After correcting for instrument response, the data are windowed and filtered into 12 different frequency bands using a 10-mHz-wide, 4^{th}-order, zero-phase Butterworth filter. The center frequencies are between 8 and 50 mHz, or 20-125 s period (Fig. 2.2), corresponding to seismic wavelengths of ~80-500 km. Fundamental Rayleigh waves are sensitive to structure to a depth of approximately one wavelength, with peak sensitivity in depth at about 1/3 of the wavelength (Fig. 2.2c). We measure the amplitude and phase of each bandpassed-filtered seismogram using the discrete Fourier transform. To ensure data quality we select Rayleigh waves having amplitudes at least 2.5 times greater than that of the preceding body waves. Further, we use seismograms only from events for which the waveforms from station to station are similar, i.e., for which the average normalized cross-correlation coefficient is greater than 0.9.

Propagation effects outside the network, as well as heterogeneous structure within the network, can affect Rayleigh waves. In order to account for wave-propagation effects outside the network, such as multipathing, we use a two-plane-wave approximation

technique (Forsyth and Li, 2005). At each frequency ω, the incoming wavefield of a particular event is represented as the sum of two plane waves of the form

$$U_z(\omega) = A_1(\omega) \exp(-i\,(\mathbf{k_1}\cdot\mathbf{x} - \omega t)) + A_2(\omega) \exp(-i\,(\mathbf{k_2}\cdot\mathbf{x} - \omega t)), \quad (2.1)$$

where U_z is vertical displacement, A_i is the amplitude of each incoming plane wave, $\mathbf{k_i}$ is the horizontal wavenumber vector, $\mathbf{x}$ is the position vector, and t is time. Li et al. (2003) showed that when this method was used in Rayleigh wave tomography in eastern North America it provided 30-40% variance reduction compared with the standard one-plane-wave method.

To characterize the heterogeneous structure within the network, the target volume is parameterized using a grid of nodes. The phase velocity is defined at each of these nodes by

$$V(\omega,\theta) = B_0(\omega) + B_1(\omega) \cos(2\theta) + B_2(\omega) \sin(2\theta), \quad (2.2)$$

where B_0 is the azimuthally averaged phase velocity, B_i are the anisotropic phase velocity coefficients, θ is the azimuth of propagation, and ω is frequency. We assume that higher-order azimuthal terms (4θ terms) are small for Rayleigh waves (Smith and Dahlen, 1973). The direction of fast propagation is ½ arctan (B_2/B_1), and the peak-to-peak amplitude or degree of anisotropy is $2(B_1^2+B_2^2)^{1/2}/B_0$. We invert the frequency-dependent phase and amplitude data separately for each period band.

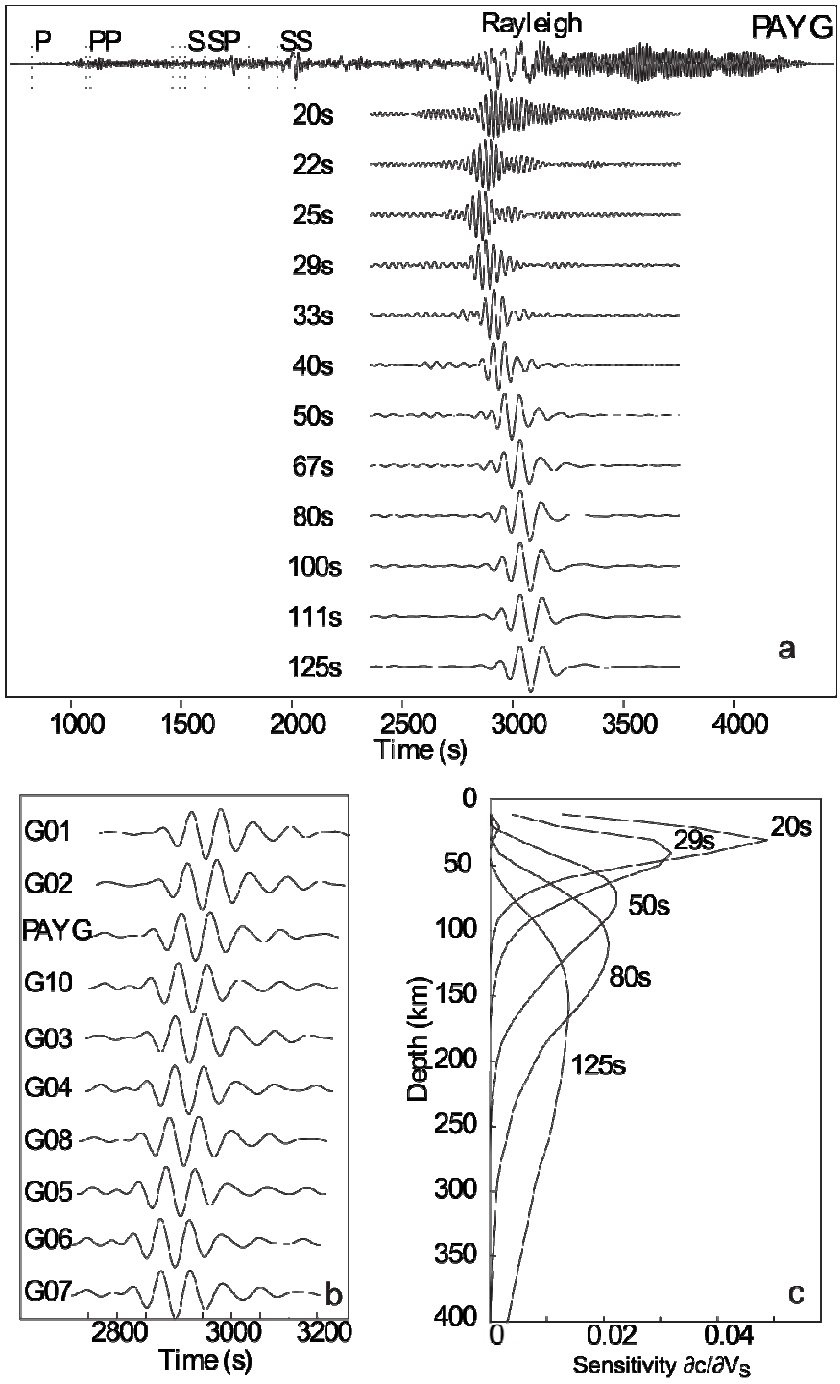

Fig. 2.2. (a) Vertical seismograms for station PAYG for an event that occurred in the Vanuatu Islands on 26 November 1999 (M_S 7.3, epicentral distance 100°, back azimuth 253°). Unfiltered seismogram on top and bandpass-filtered Rayleigh waves for periods 20 to 125 s below. (b) Rayleigh waves filtered at 50-s period, on vertical seismograms for all recording stations. (c) Sensitivity kernels for Rayleigh waves as functions of depth for periods of 20, 29, 50, 80, and 125 s.

Because of their finite frequency, surface waves are sensitive to two-dimensional (2-D) structure near the propagation path. To account for these effects we calculate 2-D sensitivity kernels for fundamental Rayleigh waves by means of a single-scattering (Born) approximation (Zhou et al., 2004; Yang and Forsyth, 2006). For each frequency band, the phase and amplitude sensitivity kernels are calculated for phase velocity perturbations and are incorporated into the isotropic phase velocity inversions (Fig. 2.3).

The solution of the non-linear inverse problem for plane wave and phase velocity parameters is performed as a two-stage iteration process (Forsyth and Li, 2005). In the first stage of each iteration, velocity is held fixed and the best fitting parameters for the two-wave approximation are found for each using the downhill simplex method of simulated annealing (Press et al., 1992). In the second stage, corrections to the velocity model and wave parameters are determined using the linearized inversion technique of Tarantola and Valette (1982). The observed data, the real and imaginary components at a single frequency, are initially assigned equal variance. Experience shows that a typical misfit to the normalized real and imaginary terms is on the order of 0.1, which we choose as an initial a priori estimate of standard deviation.

We also assume that the solution (velocity parameters) is not too far from an initial estimate, so we penalize changes from this starting model. This penalty is achieved by introducing non-zero terms in the diagonals of the a priori model covariance matrix. The amount of penalization is controlled by the parameter $\sigma_{o,}$ which is the a priori value of the standard deviation for the velocity terms in the inversion. This parameter is an estimation of the allowed variations with respect to the starting model. In addition, we position a set of nodes surrounding the region of interest, for which we allow more

variation; this outer ring of nodes absorbs additional travel-time variations not accounted for by structure inside the target volume.

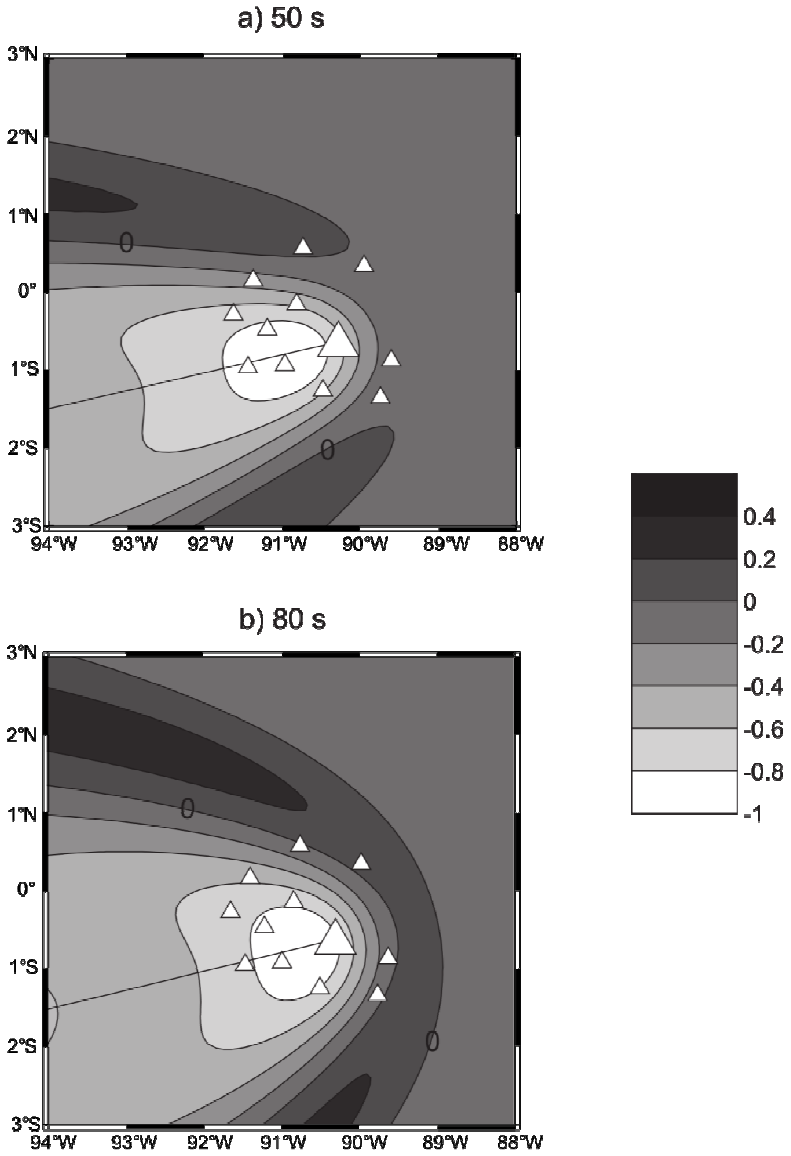

Fig. 2.3. Normalized two-dimensional phase sensitivity kernels to local phase velocity perturbation showing the first negative and positive sensitivity regions for the event depicted in Fig. 3 and station PAYG at (a) 50-s period and (b) 80-s period. White triangles represent seismic stations, the larger triangle denotes station PAYG, and the black line indicates the great circle path.

To remove the influence of events that are not well described by the two-plane-wave approximation, each inversion is performed in two sets of iterations. In the first set, all the observations are assigned equal variance or weight, as expressed above. Then, in the second set of iterations, the observations are assigned variances based on the resulting standard deviations found after the first set of iterations. This sequence ensures that poor wavefield models are given less weight and do not bias the inversion. To describe the quality of fit to the data we use the root-mean-square (RMS) misfit of the phase in seconds, which represents the misfit that is most directly related to travel times and the velocity structure.

2.2.2. Inversion for V_S

The estimates of isotropic phase velocity are in turn used to constrain the shear wave velocity (V_S) structure. Changes in the phase velocity of a Rayleigh wave are mainly sensitive to perturbations in shear wave velocity and less to perturbations in compressional wave velocity (V_P) or density. We perform inversions for one-dimensional (1-D) V_S structure at each grid node by finding the best fit between the observed phase velocities and those predicted by the code DISPER80 (Saito, 1988), which calculates normal modes for laterally homogeneous media. This technique yields predicted isotropic phase velocities from a given shear wave velocity model, as well as sensitivity kernels for V_S, V_P, and density. These sensitivity kernels are used in the inversion for V_S perturbations from a starting model in an iterative process using the linearized inversion technique of Tarantola and Valette (1982). The inversion results are values of V_S as a function of depth and estimates of standard deviation.

Because the inversion for shear wave velocity is underdetermined we must assume some a priori information about the model parameters. We use an a priori model covariance matrix of the form (e.g., Tarantola and Valette, 1982):

$$Cm_{i\,j} = \sigma_i^2 \exp(-(D_i-D_j)^2/(2\,\Delta^2)), \qquad (2.3)$$

where D is depth, Δ is the characteristic length of smoothing, and σ_i is the a priori estimate of the standard deviation of the ith velocity term in the inversion. We assume that the resulting shear wave velocities are not too far from an initial estimate, so we penalize changes from this starting model by introducing non-zero terms in the diagonals of Cm. The amount of penalization is controlled by the parameter σ_i. A lower value of σ_i represents a higher penalty and greater damping of the solution. Using different values of σ_i for different layers allows us to constrain selectively the different parts of the model. Additionally, we introduce the assumption that the resulting velocity model is smooth. We impose smoothness on the model for the ith parameter by penalizing differences in velocity with respect to neighboring points, through the introduction of non-zero terms to the off-diagonals of the a priori model covariance matrix weighted using the characteristic distance Δ.

A three-dimensional (3-D) V_S model is constructed by merging all the 1-D V_S results obtained at each node. This 3-D model is generally smoother in the vertical direction than laterally, and so we apply horizontal smoothing within each depth layer using a two-dimensional moving average of neighboring points. When smoothing laterally, we allow changes only up to a small fraction of the standard deviation, usually 10-20%. The resulting model is thus smooth in both the vertical and lateral directions,

and in our experience the maximum magnitude of a typical velocity anomaly is somewhat decreased but its spatial extent is preserved.

2.3. Results

We first present results concerning the validity of the two-plane-wave approximation method and a comparison with estimates of the direction of propagation obtained independently from polarization analysis. Second, we show results of inversions for one- and two-dimensional phase velocity, for cases with and without anisotropy. Third, we present images of three-dimensional V_S structure derived from the two-dimensional isotropic phase velocity inversions.

2.3.1. Validity of the Two-Plane-Wave Approximation

Results of the two-plane-wave approximation show that in general the primary wave is much larger in amplitude than the secondary wave. The average ratio of the primary wave amplitude to the secondary wave amplitude decreases with frequency from 7.9 at 8 mHz (125 s period) to 2.8 at 50 mHz (20 s period). This decrease is expected because higher frequency waves are more strongly affected by focusing and multipathing. Further, deviations from great circle path are less than 30° for the primary waves.

To test the validity of the two-plane-wave approximation we compare the two-plane-wave results with those obtained independently from polarization analysis (Vidale, 1986). To ensure measurement quality we use the cutoff parameters of Larson and

Ekström (2002) for Rayleigh waves. Measurements of the direction of propagation of Rayleigh waves using polarization analysis confirm that deviations from great circle paths are small (less than 30°). Moreover, polarization analysis and the two-plane-wave approximation are generally in good agreement on the primary direction of propagation (Fig. 2.4).

To investigate if local topography affects the propagation of Rayleigh waves, we measure the scattering of the arrival angles for all events at each station from polarization analysis. If there is a local topographic effect, there should be noticeable scattering of the individual arrival angles. Moreover, if topographic effects are important, scattering should be frequency dependent, because higher-frequency waves are more sensitive to topography than lower-frequency waves. The amount of scattering is quantified using the standard deviation of the individual measurements. We found that the scattering of measurements is relatively small (averaging 8.4 ± 5.1° for all events), and that there is no frequency dependence at the 95% confidence level. We conclude that the effect of local topography on the propagation of Rayleigh waves is not significant and that the incoming wavefield can be accurately described by the two-plane-wave approximation.

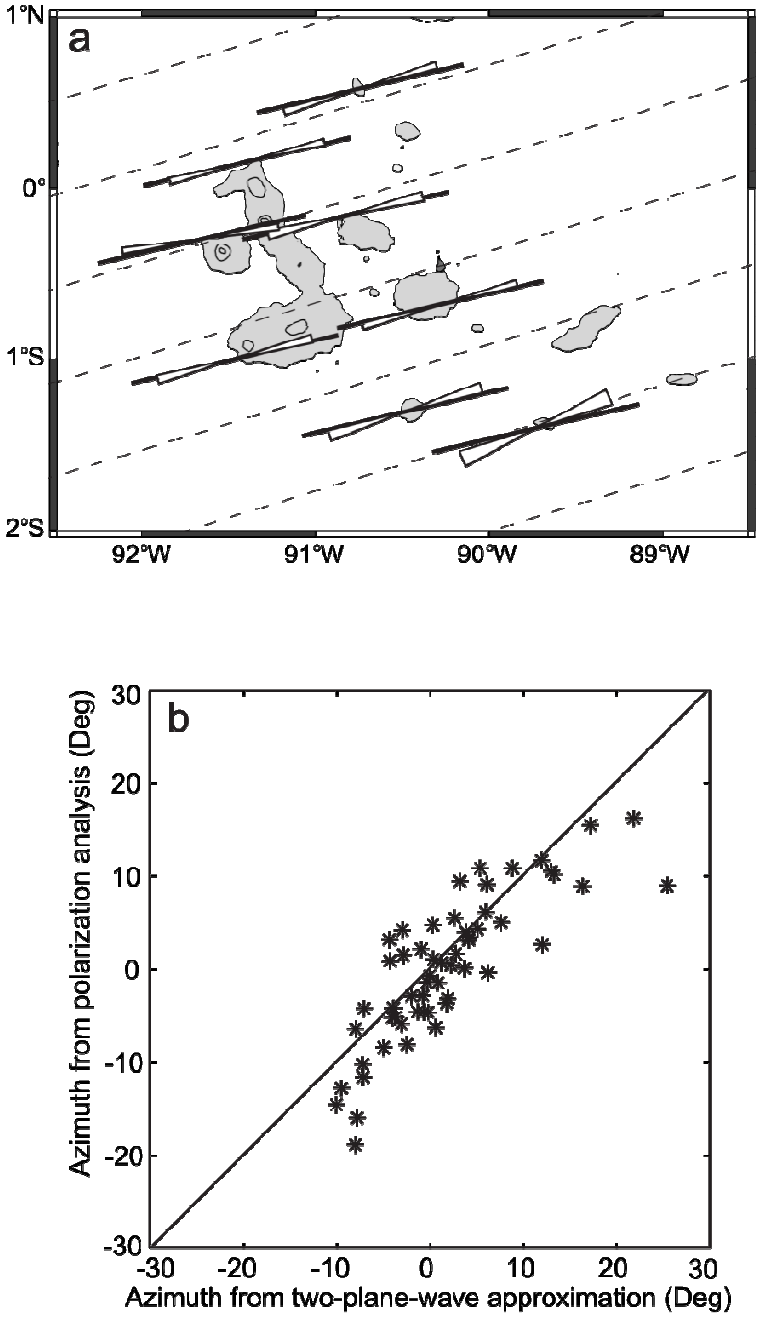

Fig.2.4. Results from the two-plane-wave approximation and polarization analysis. (a) Polarization direction of Rayleigh waves for the event shown in Fig. 3. Filled white bars indicate the direction from polarization analysis and its uncertainty. Dashed lines show great circle paths, and solid lines indicate the direction of the primary wave from the two-wave approximation. (b) Deviation from great circle path of the first plane wave from the two-wave approximation compared with the mean deviation from great circle path from polarization analysis for a 29-s period and events with an amplitude ratio of primary to secondary waves of greater than 4.

2.3.2. Phase Velocity Inversion

We present results from four sets of inversions for frequency-dependent phase velocity. In all inversions we use a regular grid of nodes separated by 0.2° in latitude and longitude (Fig. 2.5a); this grid is encompassed by a set of nodes with larger prior uncertainties. Figure 2.5b shows the typical path coverage used for the phase velocity inversions. Table 2.1 shows the number of events and observations and the resulting RMS phase misfits for all inversions.

Period (s)	Number of events	Number of observations	RMS phase misfit (s)		
			Uniform velocity No anisotropy	Uniform velocity Uniform anisotropy	2-D velocity No anisotropy
20 s	94	1330	0.64	0.62	0.51
22 s	110	1498	0.58	0.53	0.51
25 s	123	1636	0.71	0.62	0.59
29 s	119	1584	0.89	0.78	0.69
33 s	118	1660	0.68	0.63	0.62
40 s	120	1564	0.79	0.72	0.68
50 s	120	1540	0.85	0.80	0.77
67 s	110	1394	0.93	0.87	0.86
80 s	88	1114	0.83	0.81	0.83
100 s	76	912	0.82	0.82	0.78
111 s	69	828	0.92	0.88	0.86
125 s	63	734	1.01	0.97	0.92

Table 2.1. Comparison of phase velocity inversions

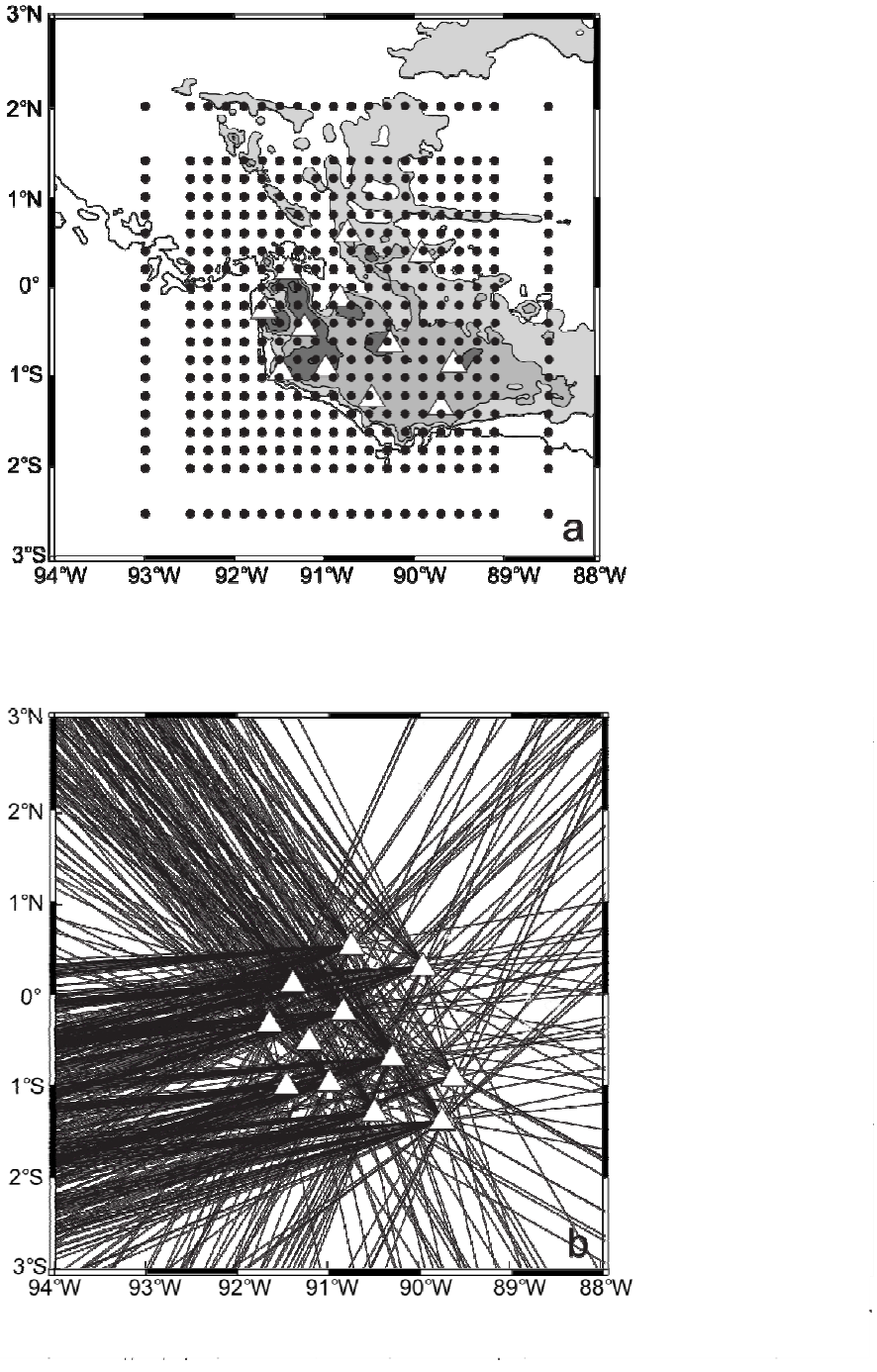

Fig. 2.5. (a) Grid node parameterization used in the phase velocity inversions. (b) Path coverage for 50-s phase velocity inversion. White triangles denote seismic stations.

In the first set of inversions we solve for the isotropic component of phase velocity, B_0, which is kept constant at all grid nodes. These results provide a uniform isotropic phase velocity for the entire region for each period. We use an initial value of phase velocity of 3.8 km/s and σ_o=0.1 as the a priori value of the standard deviation for the phase velocity.

Results of the inversion show that phase velocity increases with period from 3.625 ±0.005 to 4.05±0.02 km/s for periods from 20 s to 125 s (Fig. 2.6). These values are consistently lower than values for Pacific lithosphere of comparable age (Nishimura and Forsyth, 1989), although this difference is less pronounced at longer periods. At periods of 20 to 67 s the phase velocity is 2 to 2.5 % lower than for Pacific lithosphere 0-4 My old (0-4NF89) and 4.5 to 8% lower than for Pacific lithosphere 4-20 My old (4-20NF89). At longer periods, 80 to 125 s, phase velocities are 0 to 2% lower than for 0-4NF89 and 2.5 to 4% lower than for 4-20NF89. Phase velocities are 1-2% higher than values for Iceland (Li and Detrick, 2006), except at periods 25 to 50 s where they are similar, and are comparable to young Pacific lithosphere near the East Pacific Rise (EPR) (Forsyth et al., 1998) (Fig. 2.6).

In a second set of inversions, we add uniform azimuthal anisotropy and solve for the phase velocity parameters (B_0, B_1 and B_2), which are kept constant at all grid nodes. We use σ_o=0.1 as an a priori value of standard deviation for the velocity and anisotropy terms. Results from the inversion show that the coefficient B_0 changes by less than 0.3% from the previous isotropic inversion. From the coefficients B_1 and B_2 we obtain average values of the fast direction of propagation and amplitude of 2θ anisotropy for the entire region. Measurements of seismic anisotropy provide an important constraint on mantle

flow. Finite strain induces lattice-preferred orientation (LPO) of minerals, such as the alignment of the olivine a axis (e.g., Christensen, 1984). Because olivine, the most abundant mineral in the upper mantle, is seismically anisotropic, the alignment of crystallographic a axes caused by mantle flow can produce measurable anisotropy.

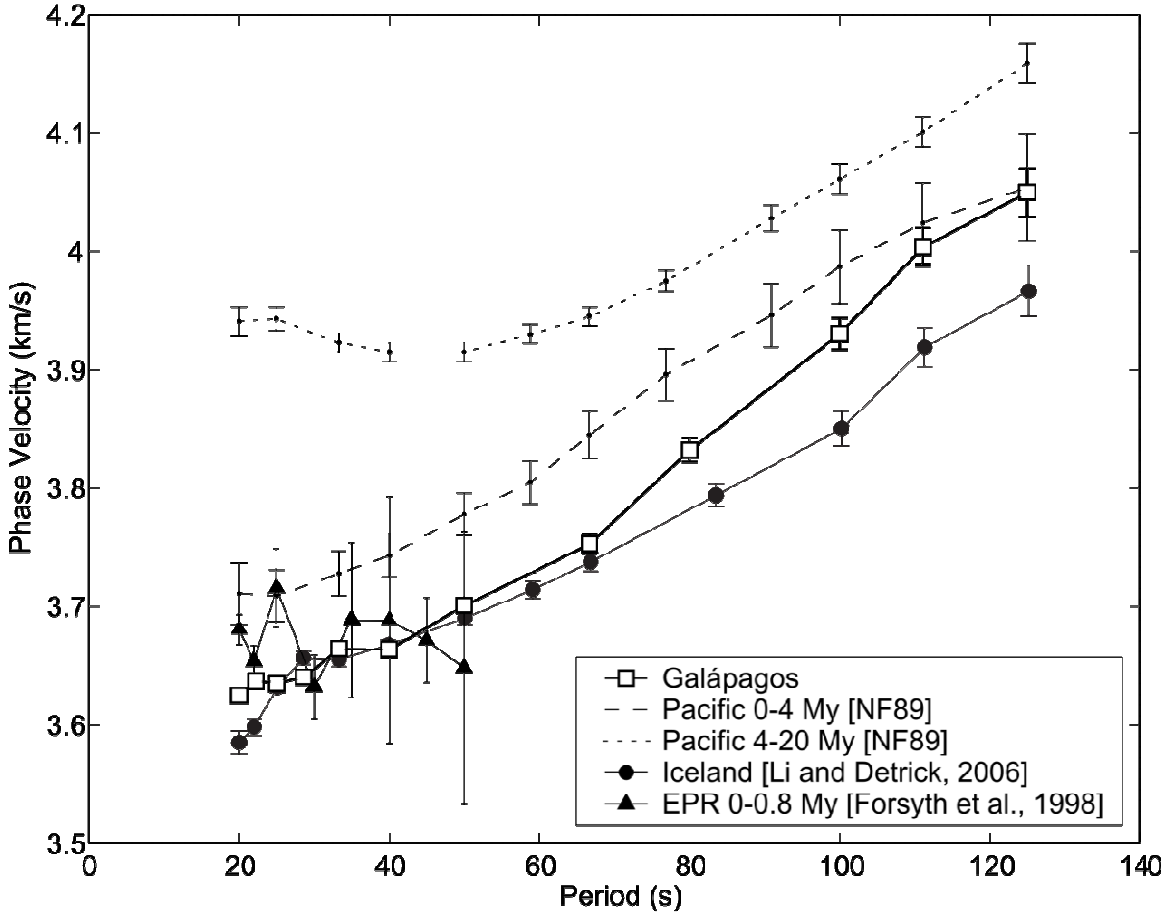

Fig. 2.6. Average phase velocity as a function of period for the Galápagos Archipelago (white squares and bold line). Dashed and dotted lines indicate results from Nishimura and Forsyth *(*1989*)* for Pacific Ocean lithosphere of age 0-4 My and 4-20 My old, respectively. Circles indicate results from Li and Detrick *(*2006*)* for Iceland. Triangles indicate results from Forsyth et al. *(*1998*)* for the East Pacific Rise. All error bars represent one standard deviation.

The peak-to-peak amplitude of azimuthal anisotropy varies between 0.2 and 1% (0.3-0.5% standard deviation) for periods 20-50 s, and between 1.2 and 3% (0.6-1.4% standard deviation) for periods 67-125 s (Fig. 2.7a). The values at 100-s period have been omitted because of the large uncertainties associated with the resulting parameters, and because we did not achieve a misfit reduction relative to the isotropic inversion (see Table 1). However, because of the relatively high uncertainties we cannot reject the null hypothesis of isotropy at the 95% confidence level, especially for periods 20-50 s. This result suggests that at shallower depths the magnitude of the regional azimuthal anisotropy is small or variable in direction so that effective anisotropy is low. Significant seismic anisotropy is observed at periods longer than 50 s, indicating that its source is likely located at depths greater than ~100 km (see Fig. 2.2c). For periods greater than 50 s, a degree of anisotropy of about 1-3% agrees with regional estimates of Nishimura and Forsyth (1988) that show azimuthal variations of 1-2%.

The direction of fast Rayleigh wave propagation is generally close to east-west (73-101°), comparable with the easterly direction of Nazca plate motion in the hotspot reference frame (90.1° azimuth at 0°N, 91°W, for HS3-NUVEL1A) (Gripp and Gordon, 2002). At 25- and 29-s period the fast direction of propagation changes to almost N-S (14 ± 9° and 9 ± 51°, respectively), close to the direction of Nazca-Cocos spreading (7.15° at 1°N, 91°W, for NUVEL-1A) (DeMets et al., 1994). However, because only two period bands show this anomalous direction, and because of the high uncertainty of the measured azimuth for the 29-s band and the low degree of anisotropy at lesser periods, we consider that the predominant direction of azimuthal anisotropy in the region is east-west (E-W). We could not resolve lateral variations of anisotropy, and thus our results are

average estimates of azimuthal anisotropy for the entire region, which includes the Galápagos platform and its surroundings (Fig. 2.5). However, SKS splitting indicates that anisotropy within the Galápagos platform varies laterally, with isotropy in the center of the archipelago and anisotropy with nearly E-W fast directions along the western edge (81-109° at seismic stations G05, G06, G07, and G10) (Fontaine et al., 2005). Regional observations of Rayleigh wave 2θ azimuthal anisotropy across the eastern Pacific also indicate an E-W fast direction of anisotropy (Nishimura and Forsyth, 1988; Montagner and Tanimoto, 1990). We suggest that the observed Rayleigh wave azimuthal anisotropy represents an average between an E-W direction of regional mantle flow and isotropy beneath the center of the archipelago.

In a third set of inversions, we obtain lateral variations in phase velocity, but we do not allow for azimuthal anisotropy. We solve for isotropic phase velocity, B_0, at each grid node, while including 2-D sensitivity kernels. We use the value of B_0 from the uniform velocity inversions as the initial value in the 2-D inversions. We also tested the use of a 2-D perturbational model resulting from adopting the inversion solution at one period as the initial model for nearby periods (e.g., Weeraratne et al., 2007), and we confirmed that our results are independent of the starting model. The results of 2-D inversions show significant improvement (up to 40% variance reduction) when compared with the uniform isotropic and anisotropic phase velocity inversions, suggesting that lateral variations of phase velocity are required by the data. The resulting phase velocities vary laterally by up to ± 1.5% with respect to the uniform phase velocity model (Fig. 2.8). However, phase velocities are consistently lower than values for Pacific lithosphere of comparable ages: 0 to 3% lower than 0-4NF89, and 2 to 9% lower than 4-20NF89. By

examining the a posteriori model covariance matrix and the values of uncertainties in model parameters we define an area of best path coverage and resolution, which is used to plot the phase velocity maps in Fig. 2.8.

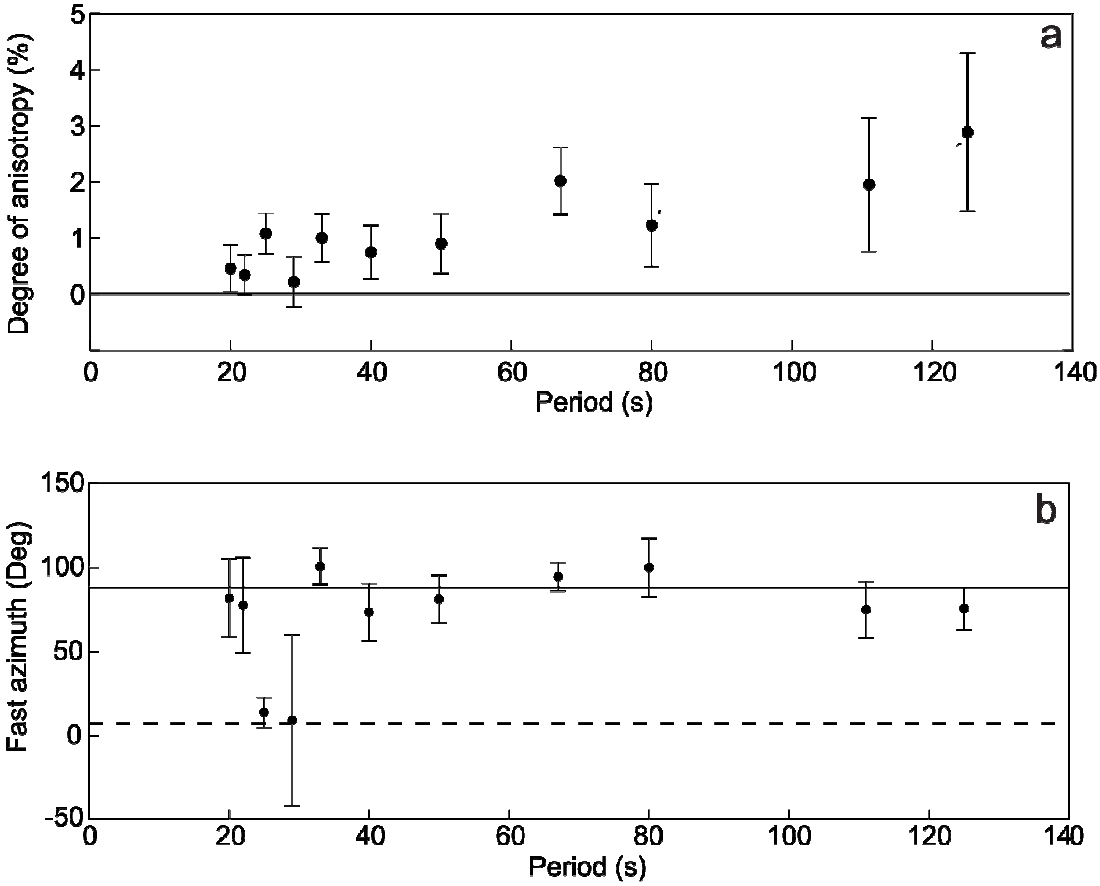

Fig. 2.7. Results from inversions with azimuthal anisotropy. (a) Amplitude of anisotropy as a function of period and 1-σ error bars. (b) Azimuth of fast direction of propagation and 1-σ error bars. The solid horizontal line indicates the direction of plate motion in a hotspot reference frame (89.4° at 0°N, 91°W, for HS3-NUVEL1A) *(*Gripp and Gordon, 2002*)*. The dashed horizontal line indicates the direction of Nazca-Cocos spreading (7.15° at 1°N, 91°W, for NUVEL-1A) *(*DeMets et al., 1994*)*.

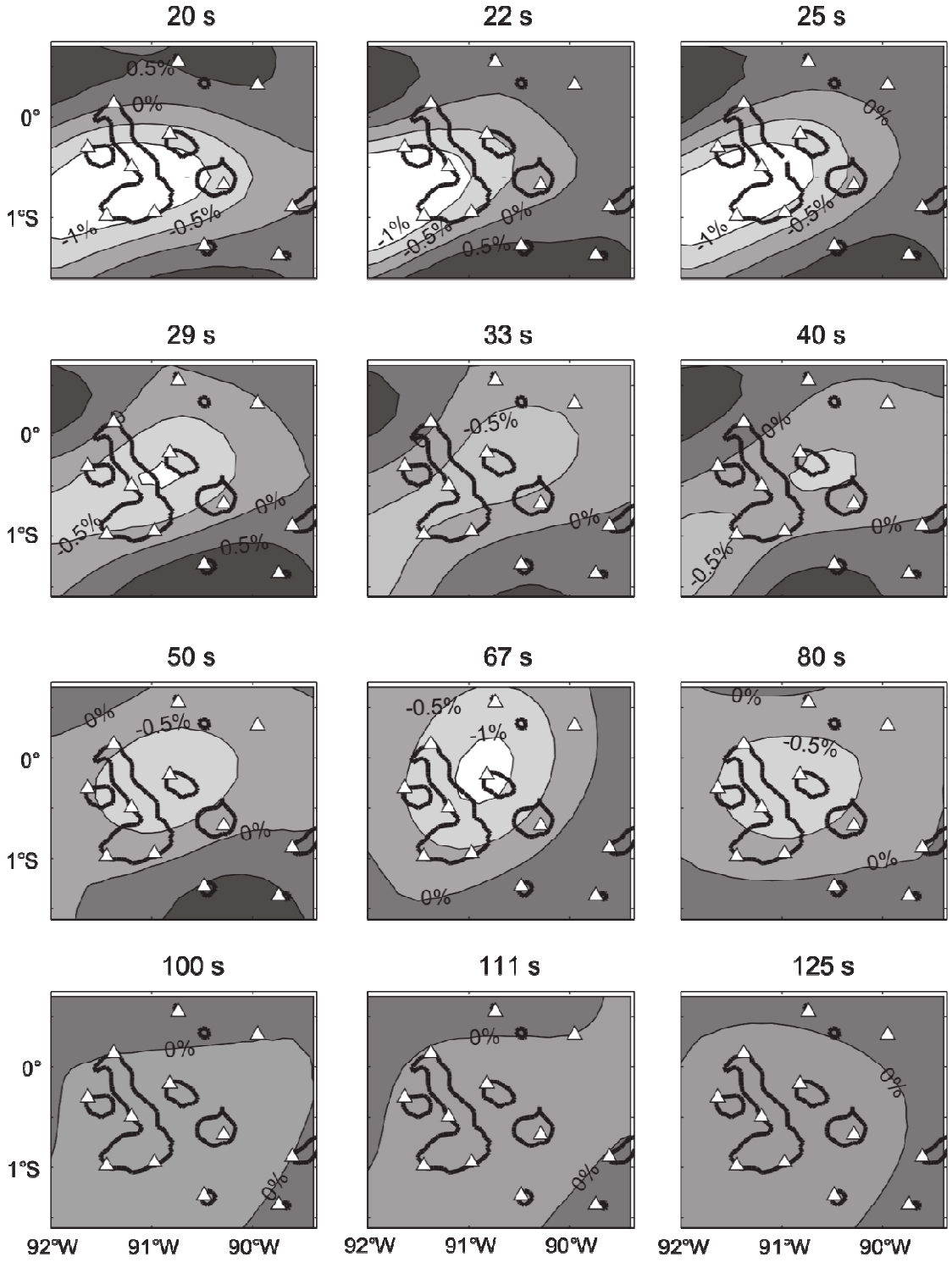

Fig. 2.8. Results of inversion for two-dimensional isotropic phase velocity for all period bands. Units are percent variation with respect to the frequency-dependent value of the isotropic uniform phase velocity (from Fig. 7). Contours shown are –1, -0.5, 0, and 0.5%. Thick lines outline the Galapagos Islands (0-m isobath), and white triangles indicate the locations of seismic stations.

There are two main regions of anomalously low phase velocity. The first is near the southwestern corner of the archipelago, beneath the volcanoes of Fernandina and southern Isabela. The anomaly is more evident at shorter periods, especially 20-25 s. The second low-velocity region is centered near 0.5°S, 90.5°W, beneath Santiago and Santa Cruz and is evident in the phase velocity maps from 29 to 80 s period. At 100 to 125 s period, the second anomaly decreases in intensity and moves slightly southward.

In a fourth set of inversions, we assume uniform anisotropy but allow for lateral variation in phase velocity. The 2-D phase velocities (B_0) vary by less that 0.3% compared with the isotropic case. The amplitude of anisotropy and the direction of fast propagation are also very similar to those obtained in the inversions with uniform phase velocity: the direction of fast propagation varies between 71 and 93°, except at 25-s and 29-s periods, where the direction of anisotropy is 19±7° and 11±74°, respectively, and the peak-to-peak amplitude of anisotropy varies between 0.15 and 2.9%. However, the results of these inversions do not provide significant variance reduction with respect to the isotropic case.

2.3.3. Shear Wave Velocity Inversion

We use the 2-D isotropic phase velocities (third set of inversions) to construct 3-D images of shear wave velocity structure. Phase velocity data at each grid node are first inverted for 1-D V_S. We then parameterize a 1-D model (0 to 410 km depth) in layers of 5-km thickness and use σ_i=0.1, Δ=10 km. Lastly, we merge all the resulting 1-D V_S models to obtain the 3-D velocity structure following the procedure described in section

2.2.2. We apply lateral smoothing while allowing for changes of less than 10% of the standard deviation.

The smooth form of the phase velocity kernels (Fig. 2.2c) shows that surface waves cannot resolve sharp vertical velocity changes, including the expected variations at the crust-mantle interface. Crustal velocity structure and thickness estimates are, however, available for the Galápagos platform (Feighner and Richards, 1994; Toomey et al., 2001). We tested the results of the inversion with three different assumptions about the crustal structure. Under the first assumption we use a constant crustal thickness of 15 km and an average crustal velocity profile (Toomey et al., 2001) as our initial model. Changes with respect to these initial crustal velocities are penalized more than changes of mantle velocities in the inversion (σ_i=0.01 versus σ_i=0.1, respectively). Because we expect bathymetric depth to be negatively correlated with crustal thickness, under the second assumption we assign different crustal thicknesses to different grid nodes as a function of bathymetry: crustal thickness is taken to be 5 km if bathymetric depth is greater than 2000 m, 10 km if bathymetric depth is between 2000 and 1000 m, and 15 km otherwise. Again, changes with respect to the initial crustal velocities are penalized more than changes of mantle velocities in the inversion (σ_i=0.01 versus σ_i=0.1, respectively). The third assumption is that crustal thickness and velocities are nowhere constrained (σ_i=0.1 everywhere). We find that changing the assumption about crustal structure has no significant an effect on velocities deeper than ~40 km; at shallower depths the magnitudes of the velocity anomalies change but their locations remain stable.

We also tested the dependence of the inversion on the mantle starting model by performing inversions using several different initial mantle velocity profiles: the isotropic

part of V_S from 4-20NF89 and models constructed from different mantle adiabats and lithospheric ages using the methodology of Faul and Jackson (2005). As an example, Fig. 10a shows the range of resulting 1-D V_S models we obtain using two different initial models (gray and hatched areas). In general we find little dependence of the results on the initial velocity model, especially for the depth range from 60 to 150 km. In what follows we discuss only those aspects of structure that are insensitive to the initial crustal and mantle velocity models.

The results of the 1-D V_S inversions with bathymetry-dependent crustal thickness are shown in Fig. 2.9. The hatched area in Fig. 2.9a corresponds to the range of models obtained using the isotropic part of V_S from 4-20NF89 as an initial model. The gray area in Fig. 2.9a-d corresponds to the range of models obtained using an initial model resulting from a 1350°C mantle adiabat, 10-My-old lithosphere, and 2-mm grain size (Faul and Jackson, 2005). For this range of 1-D models, the lowest V_S is 3.9 km/s at 65 km depth. This value is lower than those estimated beneath most young regions in the Pacific: 0-4NF89, 4-20NF89 (Fig. 2.9b), and 2-3-My-old lithosphere near the northern East Pacific Rise (EPR) or GSC (Gu et al., 2005) (Fig. 2.9c). However, it is ~4% higher that V_S at 50-60 km depth beneath 2-3-My-old lithosphere near the southern EPR (Gu et al., 2005) (Fig. 2.9c). Nonetheless, the estimates of Gu et al. (2005) for the southern EPR were made in a direction parallel to the ridge, in the slow direction of wave propagation (Wolfe and Solomon, 1998). Thus it is possible that the some of the anomalously low velocities imaged at 50-60 km depth near the southern EPR represent the effects of seismic anisotropy, and that the mean V_S is higher.

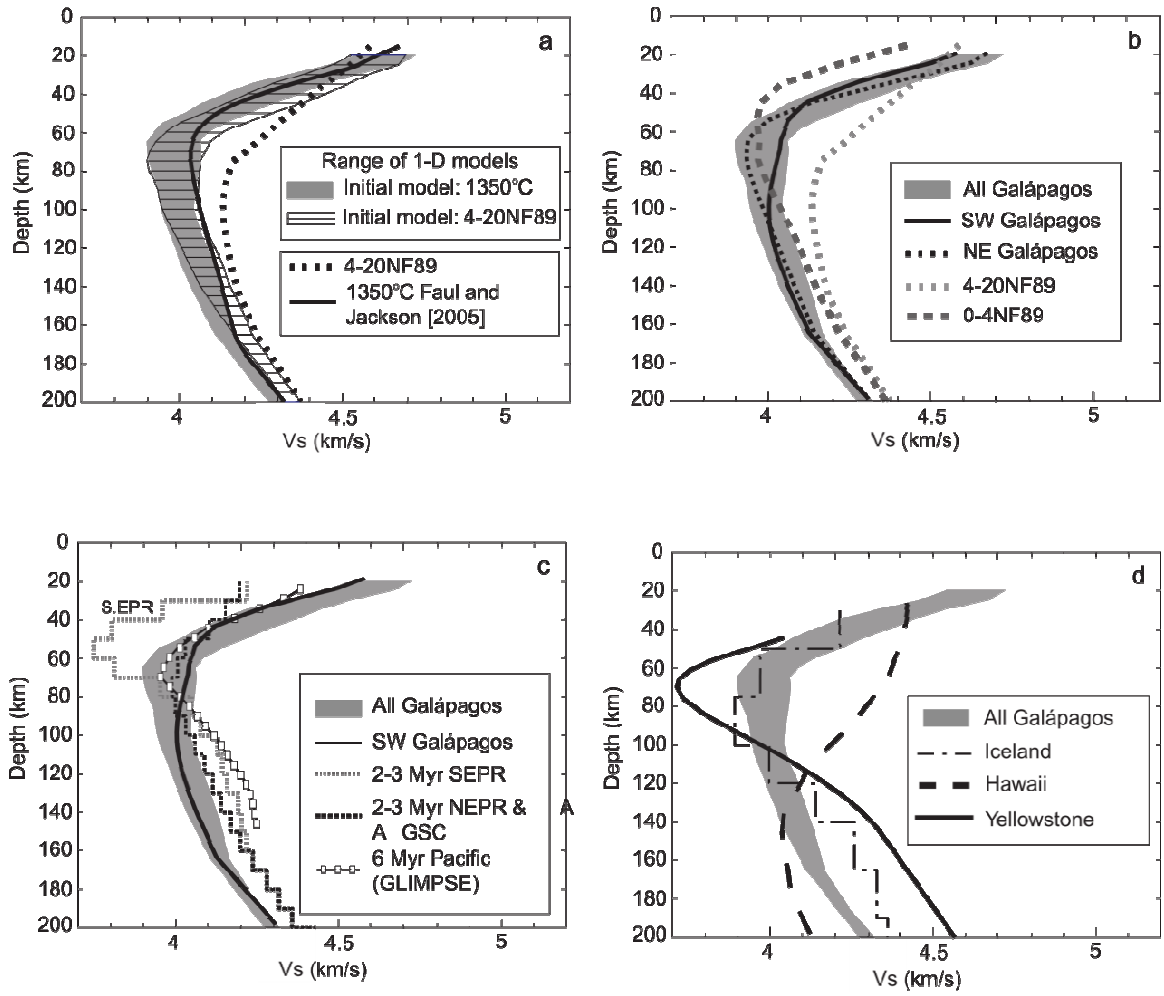

Fig. 2.9. Results of inversions for shear wave velocity. (a) Range of 1-D V_S models as a function of depth for two inversions using different initial models. Gray area indicates 1-D V_S range for an initial model derived from a 1350°C adiabat *(*Faul and Jackson, 2005*)* (solid line). Hatched area represents 1-D V_S range with 4-20NF90 (dotted line) as the initial model. (b) Comparison of Galápagos 1-D V_S models (gray area from a) and average velocities for the southwestern (black solid line) and northeastern (black dotted line) parts of the archipelago with 0-4NF89 (dashed gray line) and 4-20NF89 (dotted gray line). (c) Comparison of Galápagos 1-D V_S models (gray area from a) with Pacific V_S models. Solid lines indicate 2-3-My-old EPR and GSC from Gu et al. *(*2005*)*. White squares show a model for the mantle beneath intraplate volcanic ridges on 6-My-old south Pacific seafloor *(*Weeraratne et al., 2007*)*. (c) Comparison of Galápagos 1-D V_S models (gray area from a) with V_S models for other hotspot regions. Dash-dot line indicates the ICAV model for Iceland *(*Allen et al., 2002*)*, dashed line shows a V_S model for Hawaii *(*Priestley and Tilmann, 1999; Tilmann, 1999*)*, and solid line indicates a model for Yellowstone (Schutt et al., 2008).

Between 50 and 110 km depth, the average velocities in the southwestern part of the archipelago are up to 2.5% higher than those in the northeast (Fig. 2.9b). The average velocities in the southwestern Galápagos are also higher than those of 0-4NF89 and other young regions in the Pacific at depths shallower than ~80 km (Fig. 2.9b and 2.9c). Deeper than 100 km, both the mean and minimum V_S values beneath the entire Galápagos region are consistently lower than those beneath young Pacific seafloor elsewhere (Fig. 2.9b and 2.9c).

When compared with other oceanic hotspots (Fig. 2.9d) velocities beneath the Galápagos are comparable to mantle velocities beneath Iceland (Allen et al., 2002) between 40 and 120 km depth, but lower than for Icelandic mantle deeper than 120 km. Velocities are higher (by up to 0.2 km/s) than for sublithospheric mantle beneath Hawaii (Priestley and Tilmann, 1999; Tilmann, 1999) at depths between ~120 and 200 km. When compared with shallow mantle beneath Yellowstone (Schutt et al., 2008), the Galápagos is seismically faster at depths shallower than ~100 km, but significantly slower at greater depths (Fig. 2.9d).

In Figs. 2.10, 2.11 and 2.12 we show the three-dimensional shear wave velocity anomalies constructed from the 1-D V_S models. Velocity anomalies are relative to the initial model corresponding to a 1350°C adiabat, which we term the reference model (black line in Fig. 2.10a). Fig. 2.10 shows a comparison of results as absolute shear velocity (Fig. 2.10b) and velocity perturbations (Fig. 2.10c) along an E-W cross-section at 0.2°S. In what follows we present the three-dimensional V_S model as velocity perturbations; choosing a different reference model or showing the values of absolute velocity instead do not change the results discussed below. In map view (Fig. 2.11), we

distinguish a continuous region of anomalously low velocity between 50 and 150 km depth (Fig. 2.11b-f).

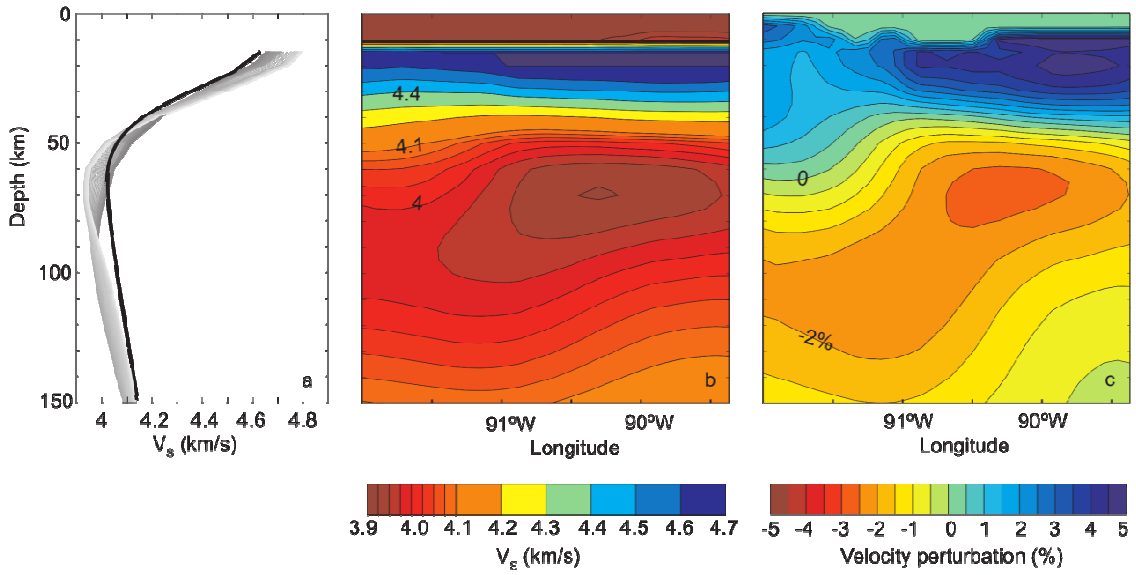

Fig. 2.10. One-dimensional V_S models and E-W cross-sections of the 3-D V_S model at latitude 0.2°S. (a) Gray lines indicate the range of 1-D V_S models, and the black line shows the reference model (1350°C adiabat, 10-My-old lithosphere, and 2-mm grain size). Gray lines go from darker to lighter from west to east. (b) Absolute V_S in km/s. (c) Velocity perturbation in percent relative to the reference model.

Fig. 2.11 (next page). Shear wave velocity perturbation at depths of 30, 50, 70, 90, 110, and 130 km. Units are percent variation with respect to the reference model. Contours are at 0.5% increments (0 and –2% contours are labeled). Thick lines delineate the Galapagos Islands (0-m isobath), and white triangles indicate the locations of seismic stations. Bold straight line to the north indicates the position of the Galápagos Spreading Center (GSC). Dashed double line in b shows the Galápagos Fracture Zone (GFZ). Gray area in b shows the southern extent of the GFZ assuming a maximum age of 3.6 My (Wilson and Hey, 1995) and a half-spreading rate of 25-30 km/My. The heavy dotted line in b and c indicates the fault-like discontinuity that Feighner and Richards (1994) suggest separates weaker lithosphere to the east from stronger lithosphere to the west and south. The black square in a, e, and f represents the center of a downward deflection of the 410-km discontinuity (Hooft et al., 2003).

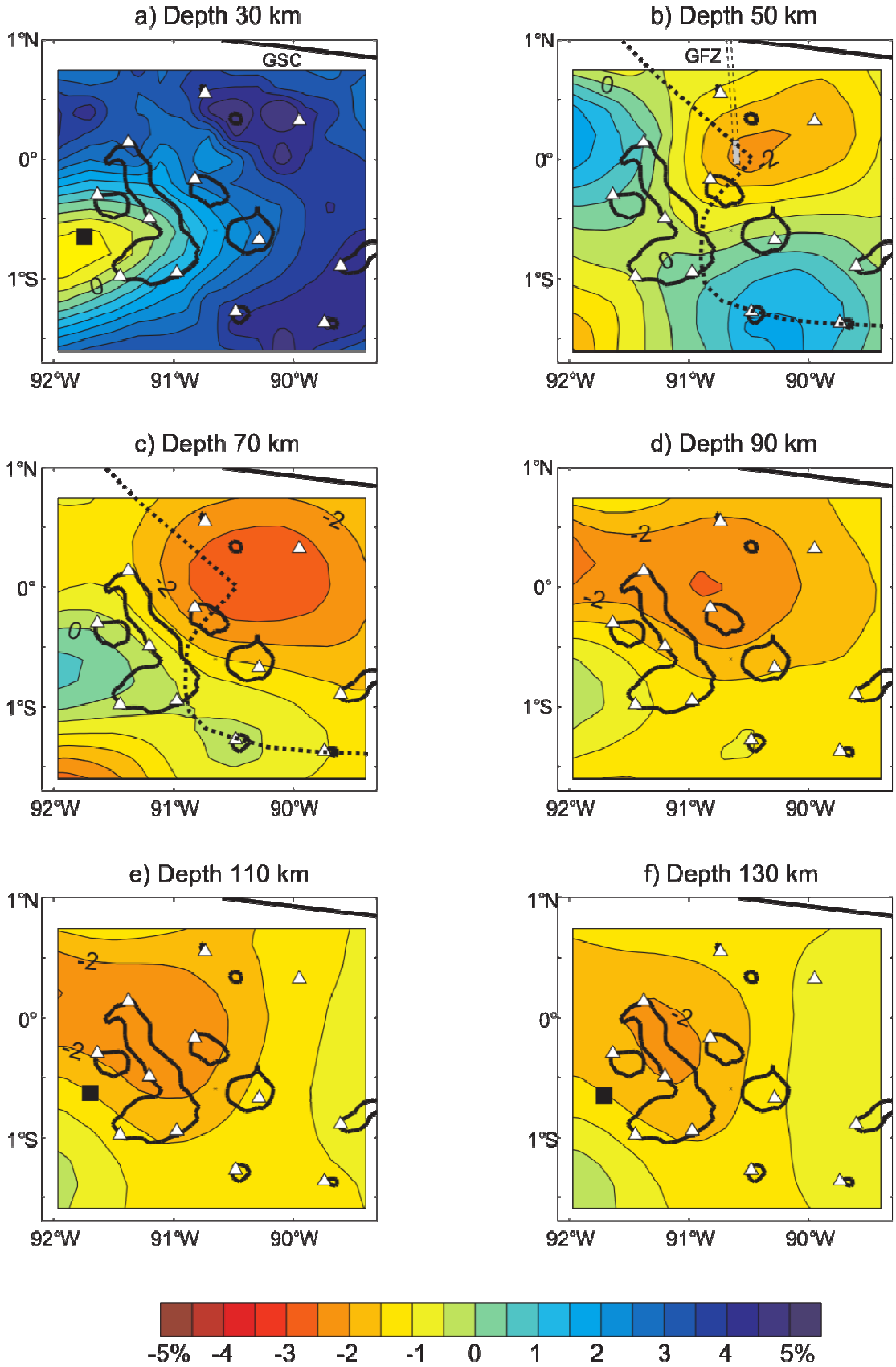
a) Depth 30 km
b) Depth 50 km
c) Depth 70 km
d) Depth 90 km
e) Depth 110 km
f) Depth 130 km
GSC
GFZ
1°N
0°
1°S
92°W
91°W
90°W
-5%
-4
-3
-2
-1
0
1
2
3
4
5%

Deeper than 100 km the lowest velocities (1-2% lower than the reference model) are localized north of 0.5°S and west of 90.5°W, beneath Fernandina and northern Isabela (Fig. 2.11e-f). Low velocities at these depths also extend to the north and northwest, toward the edge of the region of best path coverage. Spatially, this anomaly correlates well with the volcanoes of Fernandina and Isabela that are among the youngest and largest edifices in the archipelago, and where basalts show higher amounts of enrichment of incompatible elements (e.g., White et al., 1993; Harpp and White, 2001) and $^{3}He/^{4}He$ (Kurz and Geist, 1999). In addition, the lowest velocities at these depths within this anomalous region lie north-northeast of the center of a downward deflection of the 410-km discontinuity (Hooft et al., 2003) (black square in Fig. 2.11f) and above a low-velocity anomaly detected by body wave imaging at depths of 100-200 km (Toomey et al., 2002a).

Between 100 and 80 km depth, the low-velocity volume broadens in the E-W direction and intensifies toward the north, east, and west (Fig. 2.11d); this intensification may in part result from enhanced resolution at shallower depths, as discussed below. Between 80 and 50 km depth, the lowest velocities (1.5-2.5% lower than reference model) are centered at 0°, 90.5°W, beneath the islands of Genovesa, Pinta, Marchena, and Santiago (Fig. 2.11b-c). At these depths, the anomaly intensifies east of the 91°W Fracture Zone (Fig. 2.11b). This low-velocity anomaly also underlies a region that erupts depleted basalts with decreased contributions of hotspot-related incompatible elements (Harpp and White, 2001). Recent volcanic activity in this part of the archipelago is also less intense than in the western part, with less frequent eruptions and smaller volcanic

edifices. Feighner and Richards (1994) suggest that the lithosphere is weaker and possibly thinner in this region on the basis of gravity and bathymetry data (Fig. 2.11b-c).

A second low-velocity region (0-1.2% lower than reference model) is seen at shallow depths (between 20 and 40 km) in the southwestern corner of the archipelago (Fig 2.11a). This anomaly, which lies near Fernandina and southwestern Isabela and toward the edge of the area of good path coverage, lies above the center of the deflection of the 410-km discontinuity (Hooft et al., 2003) (black square in Fig. 2.11a) and a low-velocity anomaly imaged using S wave delays (Toomey et al., 2002a).

Fig. 2.12 displays vertical cross-sections though our 3-D V_S model. East-west cross-sections (Fig. 2.12a-b) show a continuous low-velocity anomaly that extends from the bottom of our model to ~40-70 km depth. Deeper than 100 km the lowest velocities are located near 91°W and are approximately confined to the west of 90.5°W (Fig. 2.12a). At 0.5°N the anomaly broadens to the west at ~100 km depth and to the east between 100 and 50 km depth (Fig. 2.12d).

North-south cross-sections (Fig. 2.12c-d) show that near 91°W the lowest velocities deeper than 100 km are located north of 1°S. At that longitude the lowest velocities are inclined from south to north as they shoal: 150 km depth at 0.5°S to 100 km depth at 0° latitude (Fig. 2.12c). At 90°W the anomalously low velocities are confined above 100 km depth (Fig. 2.12b and d).

The top of the low-velocity anomaly appears as a sharp velocity change. This boundary is present everywhere beneath the archipelago at depths from 40 to 70 km (e.g., ~4.0 km/s or 0% contours in Fig. 2.10b and c, respectively). The boundary is deepest

beneath the southwestern part of the archipelago and shoals and sharpens toward the east and north, with a more or less abrupt transition near 91.2°W in the E-W direction (Fig. 2.12a) and 0.5°S in the N-S direction (Fig 2.12c).

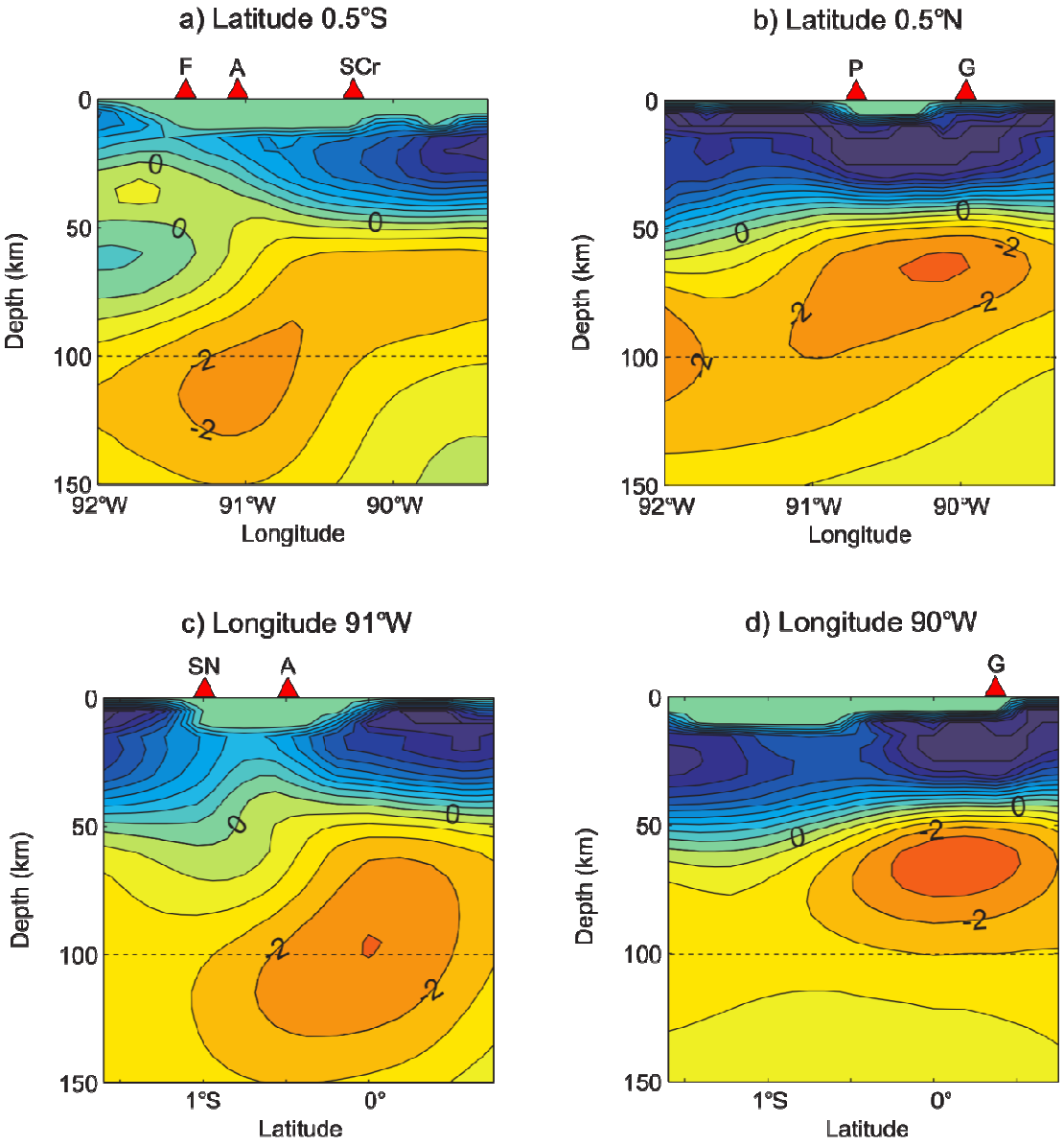

Fig. 2.12. E-W cross-sections though three-dimensional V_S model at latitudes (a) 0.5°S and (b) 0.5°N, and N-S cross-sections at longitudes (c) 91°W and (d) 90°W. Color scale and contours as in Fig. 10. Red triangles indicate approximate locations of volcanoes: SN=Sierra Negra, F=Fernandina, A=Alcedo, P=Pinta, G=Genovesa and SCr=Santa Cruz.

2.3.4. Model Resolution

Fundamental Rayleigh waves are sensitive to structure as deep as one wavelength; thus the range of frequencies used in this study could potentially provide information about structure in the entire upper mantle, to a depth of 410 km. However, resolution decreases greatly with depth, and therefore we expect that only shallow features in the upper mantle are well resolved. To test this presumption, and to test how well the depth of a sharp velocity contrast is resolved, we ran a series of inversions using synthetic three-dimensional V_S models.

In general shear wave velocity anomalies were well recovered between 30 and 80 km depth. Between 80 and 150 km depth the resolving power decreases considerably, and toward the bottom of the model (deeper than ~110 km) velocity anomalies are smeared laterally and the amplitudes can be underestimated by up to a factor of 4 for anomalies with lateral extents of less than 200 km. We assign 150 km as a maximum depth of acceptable resolution. We conclude that while the precise shapes and amplitudes of anomalies are difficult to resolve, their sign and general location are well resolved between 30 and 150 km depth.

2.3.5. Synthetic Inversions and Model Resolution

We here describe a series of inversions of synthetic data carried out to assess the resolution of the models obtained from actual data. We first obtained frequency-dependent 2-D phase velocity maps from synthetic models, and then we derived synthetic amplitude and phase data. We included the effect of a complex incoming wavefield in the

form of two plane waves with random amplitudes, phases, and deviations from great circle paths. Lastly, we added random noise to the frequency-dependent phase and amplitude data.

In the first step of the synthetic inversion we inverted the amplitude and phase data for 2-D phase velocities and compared them to the synthetic 2-D phase velocity maps. In this step we tested the efficacy of the simulated annealing algorithm in recovering the two-plane-wave information as well as the horizontal resolution imparted by path coverage and two-dimensional sensitivity kernels. We found that the incoming wavefield was well recovered by correctly estimating the wave parameters for all the primary waves and most of the secondary waves. We also found that, as expected, the horizontal resolution of phase velocity decreases with increasing period. Fig. 2.13 shows example results from the synthetic inversions for 2-D phase velocity at periods of 40 and 80 s. The synthetic model, indicated with a white square, has sides of 1° in latitude and longitude, and it represents a phase velocity anomaly of –1% at 40 s and –2% at 80 s period. The contours indicate the recovered velocity anomalies. The maximum amplitudes of the recovered anomalies are –0.83% and –0.71% for 40 and 80 s, respectively. The path coverage was adequate to recover 2-D phase velocity anomalies larger than 100 km in diameter for periods 20-50 s (Fig. 2.13a). For longer-period waves, the recovered velocity anomalies broaden progressively. For example, a 100-km-diameter synthetic phase velocity anomaly appears as a ~200-km-wide anomaly at 80 s period (Fig. 2.13b). The magnitude of the recovered anomaly also decreases progressively with period. At 80-s period we recovered only ~30% of the synthetic phase velocity anomaly (Fig. 2.13b), and at 125 s period we recovered only ~25% of the anomaly.

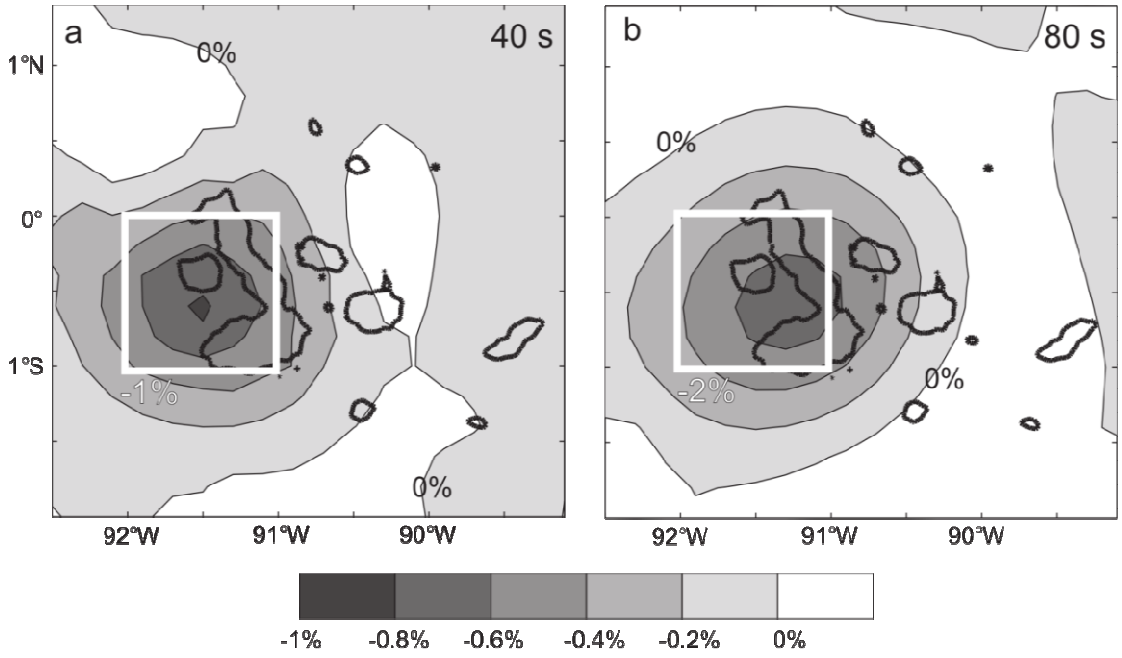

Fig. 2.13. Results of synthetic inversion for phase velocity for period of (a) 40 s and (b) 80 s. White squares indicate synthetic low velocity anomalies of -1 and -2%, respectively. Contours indicate recovered phase velocity anomaly.

In a second step we inverted the frequency-dependent phase velocities for 3-D V_S structure and compared the solution with the synthetic model. Fig. 2.14 shows examples of synthetic V_S inversions in map view and a vertical E-W cross-section. The synthetic V_S anomalies, indicated with a white rectangle in Fig. 2.14, represent a –5% anomaly. The contours represent the recovered V_S anomalies. Fig. 2.14a shows the result of a synthetic inversion for an anomaly located at depths from 40 to 100 km. The anomaly was fully recovered at depths shallower than 75 km. In addition, the sharp velocity contrast at 40 km depth is well resolved with an uncertainty of 5 to 10 km, while the 5% velocity contrast located at 100 km depth is significantly less well resolved and appears shallower in the synthetic inversions (Fig. 2.14a). Fig. 2.14b shows the synthetic inversion results for an anomaly located from 75 to 150 km depth. We recovered only

~50% of the anomaly's amplitude between 75 and 110 km depth and 25-40% between 110 and 150 km depth. The depths of the top and bottom of this velocity anomaly are not well resolved and appear shallower in the synthetic inversions.

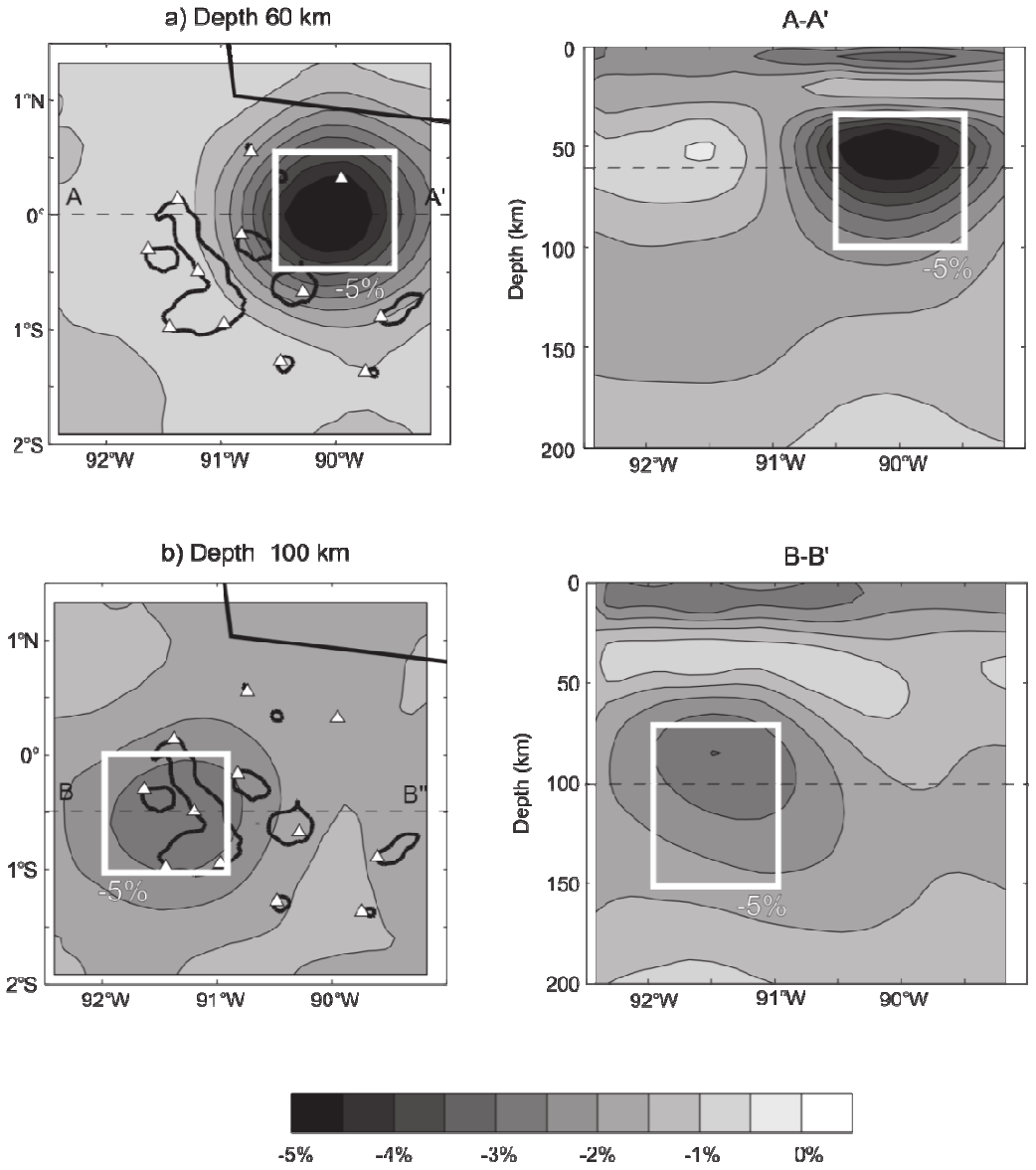

Fig. 2.14. Map views and E-W cross-sections of the results of synthetic inversion for shear wave velocity for a low-velocity anomaly of –5% located in (a) the northeastern archipelago between 40 and 100 km depth and (b) the southwestern archipelago between 70 and 150 km depth. White squares indicates synthetic anomalies. Contours indicate recovered V_S anomaly. White triangles represent seismic stations.

We find that there is little resolution at depths shallower than 20 km or deeper than 150 km. This effect can also be seen by inspecting the resolution matrix from the inversions of actual data, a direct result of the form of the phase velocity kernels shown in Fig. 2.2c. The trace or rank of the resolution matrix indicates how many parameters were independently resolved. In our inversions we obtained a maximum rank of ~3, showing that we could resolve only ~3 independent pieces of information at each grid node. Additionally, the diagonal elements of the resolution matrix indicate how well resolved each velocity parameter is in the inversion (Fig. 2.15a). Resolution is greater at shallower depths, and it rapidly decreases to zero at the bottom of our model. The values of the rows of the resolution matrix at 50, 90, and 130 km depth are shown in Fig. 2.15b. These resolution kernels or averaging functions indicate how a model parameter at a given depth depends on information from adjacent layers. Resolution length is a measure of the depth range in the model over which the average velocity is well resolved, i.e., the number of layers that need to be combined for the rank of that part of the resolution matrix to be equal to 1.0 (Weeraratne et al., 2003). The resolution length increases with depth in the inversions. For example, at 50 km depth, a 50-km-thick layer is required to recover one independent piece of information about velocity. At 90 km depth, the resolution length is 80 km, and at 130 km depth it increases to 150 km.

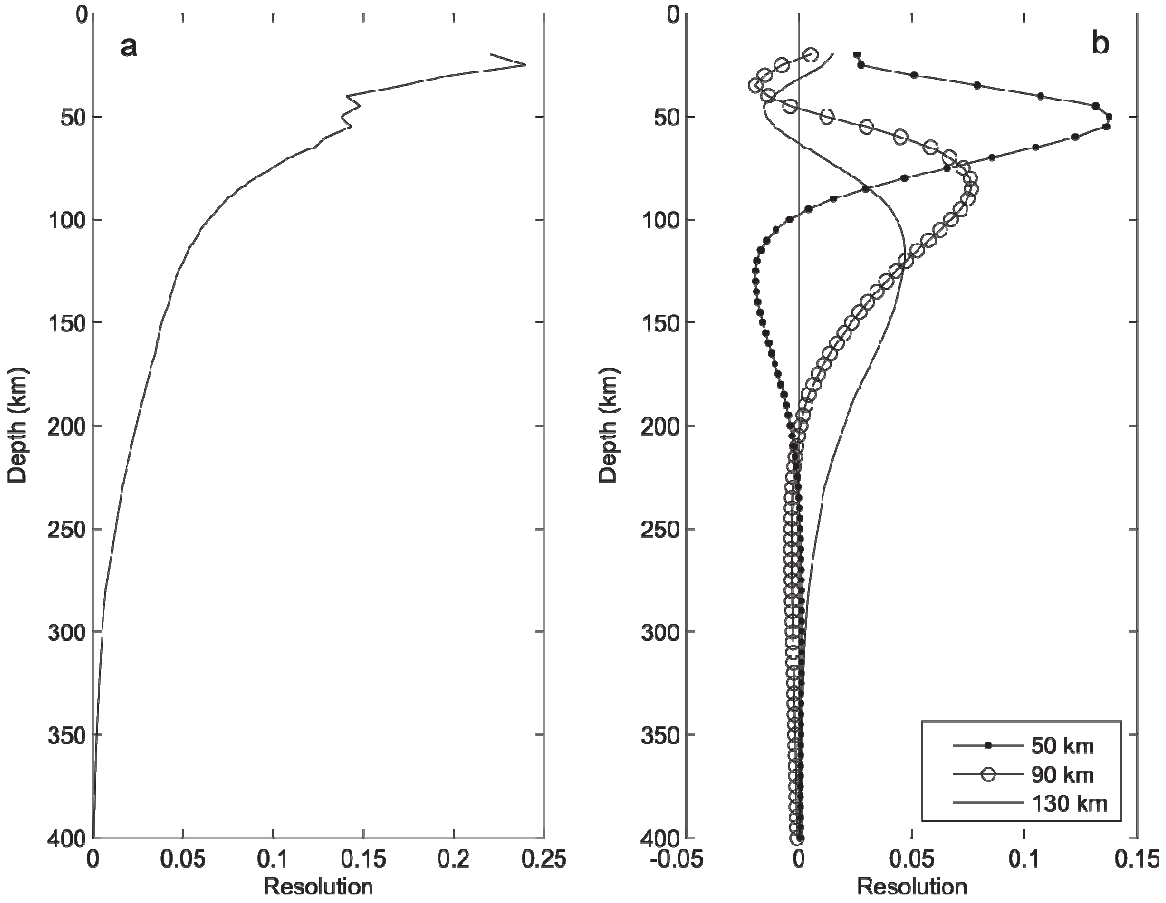

Fig. 2.15. Resolution of V_S inversion for a grid node located at 90.9°W and 0.4°S. (a) Diagonal elements of the resolution matrix as a function of depth. Total rank of the inversion is 3.14. (b) Resolution kernels (rows of resolution matrix) corresponding to depths of 50 (dots), 90 (open circle), and 130 km (solid line) as functions of depth.

Synthetic inversions using alternating positive and negative anomalies indicate that the signs of anomalies with depth extents greater than ~20 km are well recovered between 50 and 150 km depth. In particular we tested whether the velocity reversal observed beneath the southwestern archipelago at depths between 50 and 75 km (Figs. 2.11b, 2.11c and 2.12a) is an artifact of the inversion, and we found that the sign of such an anomaly can be correctly recovered in synthetic inversions. Some results show artificial velocity reversals at depths shallower than ~50 km (e.g., cross-sections A-A' and B-B' of Fig. 2.14), mainly because the inversions attempt to compensate for the poor

resolution at depths less than 20 km. This effect can be reduced by increasing the amount of damping in the shallowest part of the model during the inversion, as long as the velocities in the upper 15-20 km are well known a priori.

2.4. Properties of the Upper Mantle

Our model of shear wave velocity constrains the physical and chemical properties of the mantle beneath the Galápagos region. We first address excess temperature and melt fraction at depths of 75 to 150 km. We then examine the origin of the high-velocity lid to assess whether it is related to the formation of thermal lithosphere or to compositional variations associated with melt extraction.

2.4.1. Properties at 75-150 km Depth

Shear wave velocities beneath the Galápagos at depths between 75 and 150 km are lower than those beneath other region of comparable age in the Pacific (Fig. 2.9 b-c), suggesting that a hotter-than-normal asthenosphere underlies the Galápagos. To estimate excess mantle temperature we follow the approach of Schutt et al. (2008). We use the model of Faul and Jackson (2005), which incorporates laboratory measurements of shear modulus and attenuation made on melt-free polycrystalline olivine. Predictions of this model are dependent on grain size, temperature, activation volume (V*), and activation energy (E*).

We chose the depth range 75 to 150 km because it is everywhere below the high-velocity lid imaged in the inversions and lies mostly within the damp melting region where melt fraction is likely small. Resolution tests show that we recover only 25-50% of the velocity anomalies in this depth range, so the results are minimum estimates of excess mantle temperature.

We first calculate one-dimensional V_S models as functions of mantle potential temperature and grain size for given values of activation energy and activation volume. We assume an adiabatic temperature profile in the asthenosphere and a half-space cooling model for the lithosphere. We search for the models that best fit the results of our inversions, which permits us to bracket probable ranges in mantle temperature. Using estimates of normal mantle potential temperature, we then convert the temperature ranges to excess mantle temperature. Estimated values of potential temperature of normal mantle are 1280°C (McKenzie and Bickle, 1988), 1330°C (White et al., 1992), and 1350°C (White and McKenzie, 1995). Hereafter we choose the highest estimate of 1350°C as the nominal mantle potential temperature.

2.4.1.1. Effect of Temperature

We first constrain likely ranges of mantle potential temperature beneath the Galápagos region by assuming that the velocity variations are caused by temperature differences alone. Since there is a trade off between upper mantle temperature and grain size on shear velocity these two parameters cannot be independently constrained from a given V_S. For example, a higher potential temperature can be compensated by a correspondingly larger grain size. Grain size in the upper mantle is on the order of 1-10

mm (Hirth and Kohlstedt, 2003; Faul and Jackson, 2005). Faul and Jackson (2005) found that models for oceanic upper mantle with a 1300°C potential temperature and a constant grain size of 1 mm provide a good fit to the results of Nishimura and Forsyth (1989) for the upper 165 km in the Pacific.

We constructed 1-D V_S models for mantle potential temperatures between 1200 and 1600°C, average grain size between 1 and 10 mm, and V*=12 cm^2/mol. A comparison of our inversion results with theoretical models derived for 1350 and 1450°C potential temperatures and 2 and 10 mm grain sizes is shown in Figs. 2.16a and 2.16c. Model predictions of attenuation are shown in Figs. 2.16b and 2.16d.

We first used a value of E*=450kJ/mol derived from laboratory experiments (Karato, 1993). For an average grain size of 2 mm, estimates of temperature beneath the Galápagos region at depths between 75 and 150 km range from 1350 to 1450°C (bold and thin solid lines in Fig. 2.16a, respectively). Estimates of mantle potential temperature are greater for a grain size of 10 mm (dashed lines in Fig. 2.16a). However, model predictions using E*=450kJ/mol do not match attenuation as given by the PREM model (Dziewonski and Anderson, 1981) or as observed in other regions of young Pacific seafloor (Ding and Grand, 1993; Yang et al., 2007) (Fig. 2.16b). An alternative is to use a lower value of E*=250 kJ/mol that matches seismic observations of Q (Fig. 2.16d), as suggested by Yang et al. (2007), but which gives estimates of excess mantle temperature that are 200 to 300°C higher (Fig. 2.16c). For the following analysis we chose the laboratory estimate of E*=450 kJ/mol because it predicts conservative values of potential temperature. We note that our estimates of excess mantle temperature are thus minimum estimates.

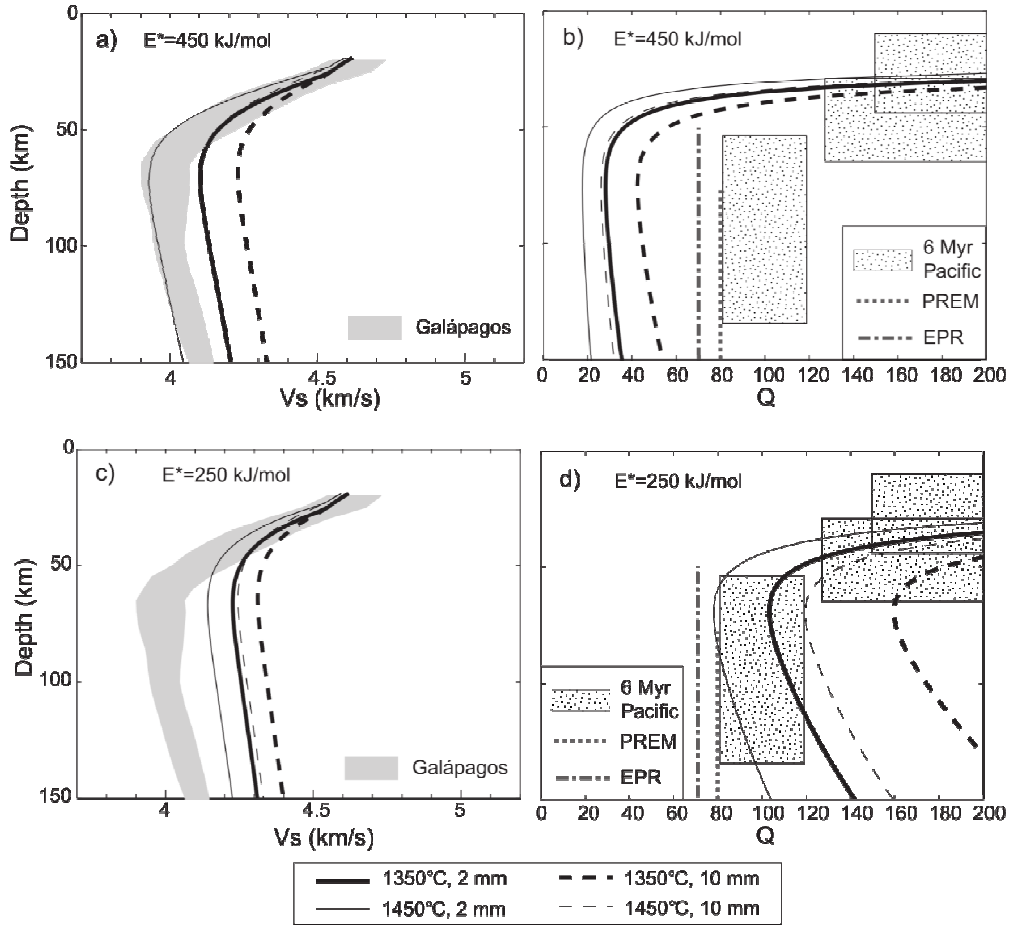

Fig. 2.16. Comparison of 1-D V_S models with models calculated using the methodology of Faul and Jackson (2005) for potential temperatures of 1350°C (bold lines) and 1450°C (thin lines) and grain size of 2 mm (solid line) and 10 mm (dashed line). (a and c) Comparison of Galápagos V_S model (gray area) with model predictions using (a) E*=450 kJ/mol and (c) E*=250 kJ/mol. (b and d) Comparison of model prediction of attenuation and seismic observations from PREM *(*Dziewonski and Anderson, 1981*)* (dotted line), EPR *(*Ding and Grand, 1993*)* (dash-dotted line), and 6 My-old Pacific from the GLIMPSE experiment *(*Yang et al., 2007*)* (dot-patterned areas) with (b) E*=450 kJ/mol and (d) E*=250 kJ/mol.

A comparison of observed V_S beneath the Galápagos region between 75 and 150 km depth and model predictions using the nominal potential temperature of 1350°C confirms that the asthenosphere shows anomalously low velocities (Fig. 2.16a). Velocity reduction varies from 0.5 to 2.5% (5 to 7%) for a grain size of 2 mm (10 mm). Fig. 2.17a shows the results of comparing the observed V_S beneath northern Isabela (where the

lowest velocities are found at depths greater than 75 km) and all the calculated V_S models for grain sizes from 1 to 10 mm. The estimated potential temperature beneath northern Isabela is 1400°C (1550°C) for 1-mm (10-mm) grain size (stars in Fig. 2.17a). The uncertainties in these values are approximately ± 20°C (30°C) for 1-mm (10-mm) grain size from the 95% χ^2 estimates (black contour in Fig. 2.17a).

We repeat this process for each 1-D V_S model. The results are summarized in Fig. 2.17b. Assuming no melt effects, the best estimates of potential temperature beneath the Galápagos region range between 1350° and 1400°C (1500 and 1550°C) for a grain size of 1 mm (10 mm), which correspond to a maximum excess mantle temperature of 50°C (200°C). The results also suggest that the range of V_S observed beneath the hotspot could be explained by lateral variations of ~50°C. This analysis takes the tomographic results at face value. However, our analysis of resolution shows that V_S anomalies are underestimated at depths between 75 and 150 km, and thus the results are minimum estimates of variations in potential temperature.

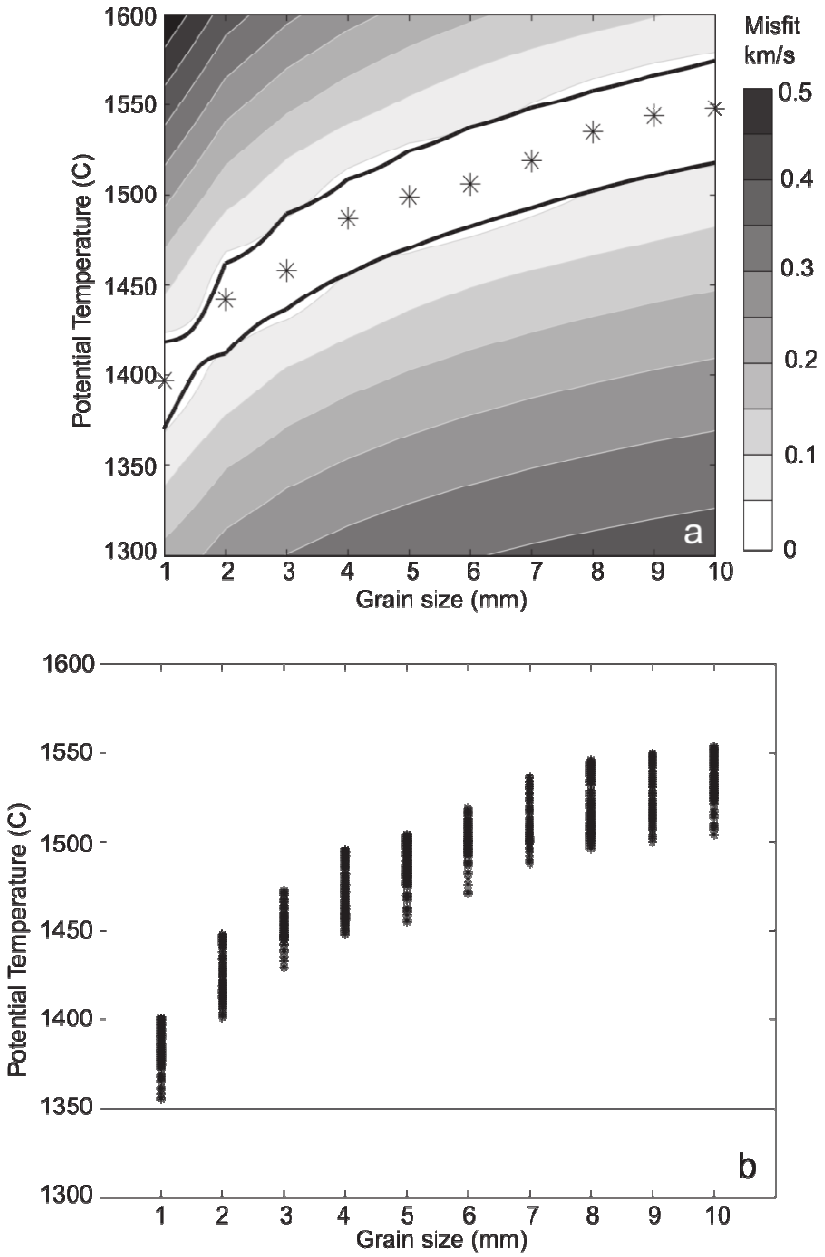

Fig. 2.17. Best fitting potential temperatures as a function of grain size assuming no melt effects on V_S. (a) Misfit between 1-D V_S model beneath northern Isabela from 75 to 150 km depth and calculated models as a function of potential temperature and grain size. The RMS misfit, which characterizes the goodness of fit between the observed V_S and the calculated model, is contoured as a function of potential temperature and grain size. Stars represent best fitting potential temperature for each grain size. Thick solid line indicates 95% χ^2 contour. (b) Best fitting potential temperature as function of grain size for each 1-D V_S model beneath the entire region. Horizontal line indicates the 1350°C potential temperature of normal mantle (White and McKenzie, 1995).

2.4.1.2. Effect of Melt Fraction

The velocity reduction observed beneath the Galápagos region is likely caused by a combination of melt and excess temperature. Here we consider the effect of partial melt on shear velocity in order to test further our estimates of excess mantle temperature. We assume that the mantle beneath the Galápagos region is buoyant and upwells, leading to decompression melting, and that the presence of volatiles initiates melting at temperatures below the dry solidus. Our goal is not to constrain absolute melt fraction, as this is not possible from V_S information alone. Instead, our main interest is to learn if, after effects of melt content are included, the low shear wave velocities still require an elevated mantle potential temperature.

We expect melt content at depths greater than 75 km to be small. Melt productivity in this region of wet melting is low, up to 25-30 times less than in the dry melting region (e.g., Asimow et al., 2004). Volatile-rich melts could be mobile at these depths even though porosity is very small (Faul, 2001). From a model of one-dimensional porous flow in a network of tubules (Turcotte and Schubert, 2002, pp. 402-405) we estimate that the melt fraction could be in the range ~0.05-0.5% at 75 km depth (section 4.2). Melt content values on the order of 0.1% are also consistent with predictions from trace element and uranium-series disequilibria models of melting at mid-ocean ridges (e.g., Lundstrom et al., 1995). We consider that for depths greater than 75 km the melt fraction is likely in the range 0.1 to 0.5%.

It is unlikely that the effect of 0.1-0.5% melt on V_S can account for the 2.5% (7%) velocity reduction observed for a grain size of 1 mm (10 mm) (Fig. 2.16a). At low melt fractions (generally less than 0.75-1%) melt is probably contained predominantly in

tubules (e.g., Hammond and Humphreys, 2000). With the melt-velocity relations of Hammond and Humphreys (2000), $\partial \ln V_S / \partial \phi = -2.7$ for melt that is contained in tubules, so 0.1 to 0.5% melt could produce 0.27% to 1.35% velocity reduction. Even if we assume a melt fraction of 1%, the velocity reduction is only 2.7%. Thus a thermal anomaly is likely at depths greater than 75 km. With a melt fraction of 0.5% between 75 and 150 km depth, our observations require a mantle excess temperature of ~30°C (~150°C) for a grain size of 1 mm (10 mm). We limit this analysis to the lower part of the model because we expect melt fraction to be higher in the dry melting region and the effect of melt on velocity to be more significant. We remark that this analysis was performed using E*=450 kJ/mol. A lower value of E*, as seems to be required by seismic observations of attenuation (Yang et al., 2007), would imply a larger temperature anomaly or a larger melt fraction.

We conclude that the anomalously low shear wave velocities detected at depths greater than 75 km are consistent with melt fractions of ~0.5% and elevated temperatures beneath the Galápagos hotspot of 30 to 150°C, depending on average grain size. Our estimate of excess mantle temperature is comparable to values suggested by other studies. The amount of thinning of the transition zone beneath the Galápagos indicates an excess temperature of 130±60 K at 410 km depth (Hooft et al., 2003); modeling of hotspot-ridge interaction for the GSC suggests 50-100 K excess temperature (Ito et al., 1997); and modeling of the source of GSC basalts affected by the hotspot indicates a mantle potential temperature of 1395°-1420°C or 45-70 K excess temperature (Asimow and Langmuir, 2003).

2.4.2. Porous Flow Model

We estimate the volume melt fraction at a depth of 75 km beneath the Galápagos region with a one-dimensional porous flow model in an idealized medium that contains a network of cylindrical tubules that is filled by melt. The pressure gradient that drives the melt upwards is the differential buoyancy of the melt relative to the solid matrix. From Darcy's law, the relative upward velocity between the melt (v_L) and the solid (v_S) is

$$v_L - v_S = -\frac{b^2 \phi (\rho_S - \rho_L)}{24\pi\mu}, \tag{2.4}$$

where b is grain size, ϕ is the melt porosity, ρ_L is the melt density, ρ_S is the density of the solid, and μ is the melt viscosity. The melt fraction flux F is defined as the ratio of the total upward mass flux of melt to the upward mass flux of rock prior to the onset of melting, or (Turcotte and Schubert, 2002)

$$F \equiv \frac{\phi \rho_L (v_L + 2v_S)/3}{\rho_S v_0}, \tag{2.5}$$

where v_0 is the upward velocity of rock prior to melting. Combining equations (2.4) and (2.5) with the equation for conservation of mass, and assuming $\phi << 1$, we obtain (Turcotte and Schubert, 2002)

$$v_S = v_0 (1 - F) \text{ , and} \tag{2.6}$$

$$v_L = -\frac{|v_S|}{2} + \left\{ \frac{9 v_s^{\,2}}{4} + \frac{F \rho_S g (\rho_S - \rho_L) b^2 |v_0|}{8\pi\mu\rho_L} \right\}^{1/2}. \tag{2.7}$$

The melt porosity ϕ can be found by solving equation (2.4). We use the parameters ρ_L=2700 kg/m^3, ρ_S=3300 kg/m^3, μ=10 Pa s and v_0=100 mm/y. We estimate

the melt fraction flux F by assuming that it is equivalent to the extent of melting (e.g., F in Langmuir et al. (1992)). Melt productivity $\partial F/\partial P$ is ~1%/GPa for water-induced melting at temperatures below the dry solidus (Asimow et al., 2004) and between 12 and 20%/GPa in the dry melting regime (Langmuir et al., 1992). We adopt constant melt productivity values of $\partial F/\partial P$=1%/GPa below the dry solidus and $\partial F/\partial P$ =15%/GPa above the dry solidus. We use the analytical dry solidus of McKenzie and Bickle (1988) to determine the depth to the solidus as a function of potential temperature. Thus ϕ is a function of both mantle potential temperature and grain size b. We estimate melt fraction to be ~0.05-0.5% at 75 km depth for grain sizes from 1 to 10 mm and mantle potential temperatures from 1300°C to 1600°C.

2.4.3. Properties at Less Than 75 km Depth

In the Galápagos region, the top of the anomalously low velocity volume is defined by a relatively sharp velocity contrast located between 40 and 70 km depth everywhere beneath the archipelago (Figs. 2.10 and 2.12). Resolution tests indicate that the depth of this boundary is known to within 5 to 10 km. The base of this high-velocity lid is deepest beneath the southwestern part of the archipelago and shoals toward the north and east.

Two possible boundaries that could be located at these depths are the bottom of the thermal lithosphere and a compositional boundary related to either depletion or dehydration resulting from melt extraction. The high-velocity lid is thicker to the west of 91.2°W and thins to the north, as expected for thermal lithospheric thickness in the region. In addition, the high-velocity lid is thinner in the northeastern part of the

archipelago, roughly matching the region of weaker and thinner lithosphere of Feighner and Richards (1994). However, estimates of thermal lithospheric thickness beneath the Galápagos region are between 30 and 45 km (calculated for a half-space cooling model and seafloor age between 5 and 15 Ma), significantly less than the 70 km depth of the boundary in the southwestern corner of the archipelago (Fig. 2.18). Thus, although we cannot rule out that the boundary corresponds to the bottom of the thermal lithosphere in the eastern archipelago, the boundary appears to be ~30 km too deep in the southwest. Anomalously high velocities beneath the southwestern archipelago at depths from 50 to 70 km are also indicated by comparisons of 1-D velocity profiles; between 50 and 110 km depth, the average velocities in the southwestern part of the archipelago are up to 2.5% higher than those in the northeast (Fig. 2.9b), and higher than those of 0-4NF89 and other young regions in the Pacific at depths shallower than ~80 km (Fig. 2.9b and 2.9c).

Our preferred explanation is that the anomalously high velocities imaged beneath the southwestern archipelago between 50 and 70 km depth correspond to a compositional change produced during melt extraction beneath the hotspot. The amplitude of the southwestern velocity anomaly is about +3%, following Faul and Jackson (2005) and for a potential temperature of 1400°C (50°C excess mantle temperature), One effect of melt depletion of peridotite is a change in modal mineralogy and major element chemistry, which can increase V_S up to 2.6% in the spinel stability field (Matsukage et al., 2005). A complementary effect is the removal of water (Karato, 1986; Hirth and Kohlstedt, 1996; Karato and Jung, 1998), which decreases anelasticity, leading to lower attenuation of seismic waves and higher seismic wave velocities. We estimate the effect of dehydration using (Karato, 1993)

$$V(\omega,T,P,C_{OH}) = V_0(T,P)\,(1-\tfrac{1}{2}\cot(\pi\alpha/2)\,Q^{-1}(\omega,T,P,C_{OH})), \qquad (2.8)$$

where $V_0(T,P)$ is the seismic wave velocity as a function of temperature (T) and pressure (P) when only elastic effects are considered; $Q^{-1}(\omega,T,P,C_{OH})$ is seismic wave attenuation and is a function of frequency (ω), T, P, and water content (C_{OH}); and the parameter α characterizes the frequency dependence of Q ($Q^{-1} \sim \omega^{\alpha}$).

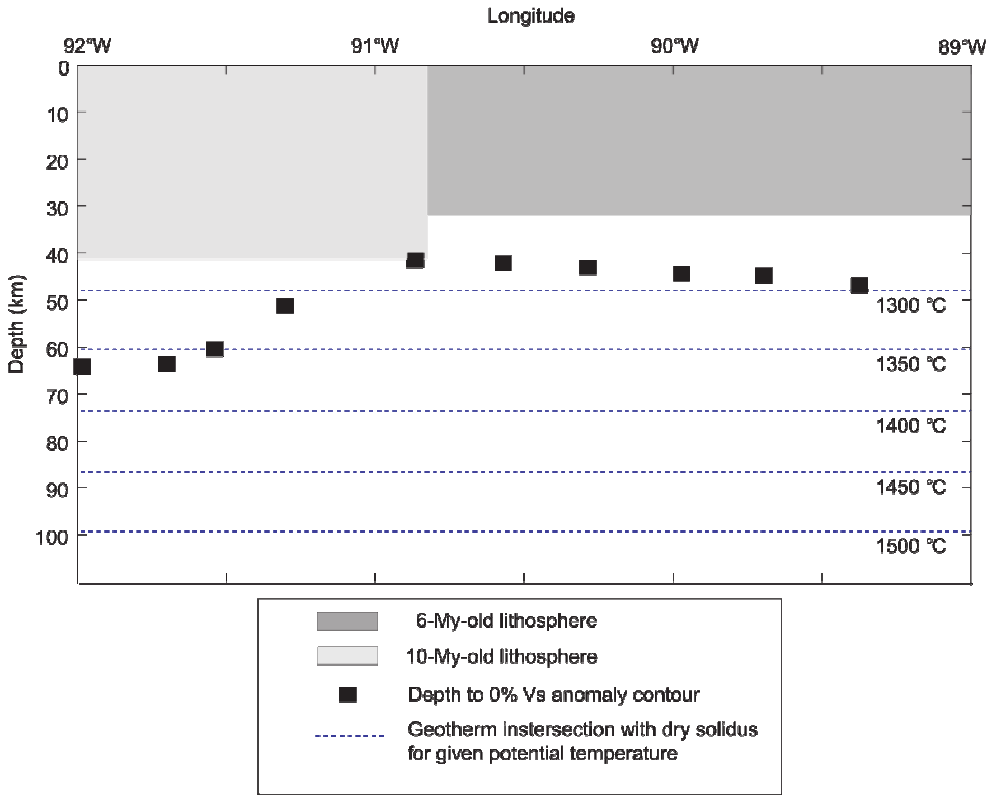

Fig. 2.18. Depth to 0% V_S change contour (squares) along an E-W profile at 0.2°S compared with the likely range in lithospheric thickness derived from a half-space cooling model (Turcotte and Schubert, 2002) and the depth to the dry solidus. Lithospheric age across this profile changes from 6 My (dark gray) toward the east to 10 My (light gray) toward the west near 90.5-91°W (southern projection of the GFZ). Dashed lines indicate depth to dry solidus as given by intersection of the analytical solidus of dry peridotite (McKenzie and Bickle, 1988) and the mantle geotherm as a function of potential temperature (Turcotte and Schubert, 2002).

We assume that dehydration increases Q from 80 to ~150 (Karato, 2003), an estimate consistent with the observed increase in Q by ~2 when dunite samples are dried prior to measurements (Jackson et al., 1992). For α between 0.1 and 0.3, we estimate that dehydration could increase V_S by 0.5 to 2%.

We conclude that the combined effects of depletion and dehydration that accompany melt extraction can explain the observed +3% velocity anomaly beneath southwestern Galápagos. By this view, the thickening of the high-velocity lid is consistent with an elevated mantle temperature of at least 1400°C (50°C excess temperature) that depresses the dry solidus and initiates dry melting at depths greater than 70 km (Fig. 2.18).

2.5. Discussion

2.5.1. A Plume in the Shallow Upper Mantle

Our results together with receiver function (Hooft et al., 2003) and body wave tomography (Toomey et al., 2002a) studies indicate that the Galápagos hotspot is underlain by a thermal plume that is continuous from the transition zone to the bottom of a high-velocity lid located at depths from 40 to 70 km. Between 120 and 150 km depth the anomalously low velocities are centered near 0.25°S and 91°W, beneath northern Isabela (Fig. 2.11f), and approximately 50 km to the northeast of the center of the deflection of the 410-km discontinuity, which marks the center of hot upwelling through the mantle transition zone (Hooft et al., 2003) (black square in Fig. 2.11f). We interpret

the low-velocity anomaly as the locus of an upwelling mantle plume. The lateral extent of the low-velocity anomaly at 130 km depth is approximately 150 km for the -1% $\partial \ln V_S$ contour (Fig. 2.11f).

The low-velocity volume appears to incline northward by approximately 45° from vertical as it shoals between 150 and 100 km depth; the plume conduit is centered at 0.5°S at 150 km depth and at 0° at 100 km depth (Fig. 2.12c). This inclination is also seen in body wave tomography, which detects a low-velocity volume near the southwestern corner of the archipelago that inclines northward as it shoals between 250 and 150 km depth (Toomey et al., 2002a).

As the upwelling mantle plume approaches the high-velocity lid, it begins to flatten and spread in conformance with the shape of the base of the lid. At depths less than ~120 km, the low velocities extend both east and west of 91°W (see -2% $\partial \ln V_S$ contour in Figures 2.11c-e and 2.12b). To the east of 90°W, low velocities are confined to depths shallower than 100 km, a depth that could correspond to the bottom of the spreading plume layer (Fig. 2.12d).

Between 20 and 40 km depth, anomalously low velocities are centered in the southwestern archipelago, above the center of the deflection of the 410-km discontinuity (Hooft et al., 2003) (Fig. 2.11a). One possible interpretation is that this anomaly indicates lithospheric thinning above the center of plume upwelling (Detrick and Crough, 1978). However, the presence of higher-than-normal velocities at depths from 40 to 70 km argues against lithospheric thinning and instead suggests a thicker than normal lid in this region. Our preferred interpretation is that this shallow low-velocity anomaly corresponds

to melt accumulation at lithospheric levels. The anomaly lies near Fernandina and Isabela, islands that contain the most active volcanoes in the archipelago, and above the main region of plume upwelling and melt production.

2.5.2. The High-Velocity Lid

The top of the low-velocity volume appears as a velocity gradient that is present everywhere beneath the archipelago at depths from 40 to 70 km. We suggest that the boundary represents stalling of plume upwelling. As the plume approaches the lid it starts to flatten and spread laterally, conforming to the shape of the lid.

The boundary is deepest beneath the southwestern part of the archipelago and shoals and sharpens toward the east and north. As argued earlier, we suggest that the thick lid observed beneath the southwestern archipelago, above the main region of plume upwelling, corresponds to depleted and dehydrated residuum produced from hotspot melting (e.g., Phipps Morgan et al., 1995; Ribe and Christensen, 1999). To the north and east, the thickness of the lid (~40 km) is less than that expected for residuum (>60 km) created by hotspot melting or ridge melting (e.g., Evans et al., 2005), which could indicate that melting at the GSC produced a weak dehydrated layer. The lid to north and east may thus represent thermal lithosphere.

The variable thickness of the high-velocity lid can be correlated to geochemical and geophysical observations in the Galápagos. The region where the lid is thickest (beneath Isabela and Fernandina) coincides with the region where basalts show higher amounts of enrichment of incompatible elements (e.g., White et al., 1993; Kurz and

Geist, 1999; Harpp and White, 2001) and $^{3}He/^{4}He$ (Kurz and Geist, 1999). Where the lid is thinner, depleted basalts with decreased contributions of hotspot-related incompatible elements are erupted (White et al., 1993; Harpp and White, 2001). The thin-lid region also coincides approximately with the region of weaker lithosphere inferred from modeling of gravity and bathymetry data (Feighner and Richards, 1994).

We suggest that the high-velocity lid has a considerable influence on both plume dynamics and melting beneath the Galápagos region. The variable thickness of the lid controls the final depth of melting and the variability in basalt composition beneath the archipelago. In the eastern archipelago, where depleted basalts erupt, a thinner lid could allow increased amounts of melting from a more depleted source at shallower depths. Conversely, basalts with higher amounts of enrichment erupt in the western archipelago where the lid is thickest. The viscosity increase associated with dehydration (Hirth and Kohlstedt, 1996) could decrease plume upwelling and melting above the dry solidus (Ito et al., 1999), and thus a thicker lid could enhance deeper melting of more enriched plume components. Since deep melting is associated with a reduced extent of melting, a relatively high plume flux would be needed to produce the more voluminous volcanism observed in the western archipelago.

2.5.3. Gravitational Spreading of the Plume

As the upwelling mantle plume approaches the high-velocity lid, it begins to flatten and spread. The low velocities extend mostly eastward at depths shallower than 100 km (Figs. 2.12a and 2.12b), in the direction of plate motion, suggesting an effect

from plate drag. However, the low velocities also appear to extend toward the west of 91.5°W at depths less than 120 km, in a direction opposite to plate motion (Figures 2.11d, 2.11e, and 2.12b). This observation of both eastward and westward plume spreading is consistent with correlated geochemical and geophysical observations along the GSC; between 83°W and 101°W geochemical and geophysical anomalies are symmetrical about 91.5°W (Schilling et al., 1982, 2003; Verma and Schilling, 1982), a longitude that is coincident with the center of plume upwelling beneath the archipelago. We attribute the expansion of the low-velocity volume both to the east and to the west to the gravitational flattening of the plume layer against the variable-thickness lid.

The gravitational spreading of a plume beneath a moving plate represents a balance between buoyancy forces and plate drag forces. This is expressed in the buoyancy number (Feighner and Richards, 1995, Kincaid et al., 1995)

$$\Pi_b = Bg/\eta_o U^2, \qquad (2.8)$$

where $B=\Delta\rho Q$ is the buoyancy flux, ρ is density, Q is the volumetric flux, g is gravity, η_o is ambient upper mantle viscosity and U is plate velocity. The spreading of plume material in a direction opposite to plate motion indicates that plume buoyancy forces dominate over plate drag forces and suggests a high buoyancy flux relative to plate velocity, a low mantle viscosity, or both.

Our observation of upstream flow beneath the Galápagos is consistent with the upper bound of estimates of the Galápagos plume buoyancy flux, which range from B=1000 kg/s (Sleep, 1990) to ~2000 kg/s (Schilling, 1991; Ribe, 1996; Ito et al., 1997). Tank experiments of sheared thermal plumes indicate that upstream plume spreading

against plate shear occurs when Π_b is greater than 70-100 (Kerr and Mériaux, 2004). For B=2000 kg/s, η_o=4 x 10^{20} Pa s (Schubert et al., 2001), and U=21 mm/yr (at 0°N, 91°W, for HS3-NUVEL1A) (Gripp and Gordon, 2002) the buoyancy number Π_b is 113, within the regime of upstream spreading. A lower estimate of B=1000 kg/s is probably insufficient to produce upstream flow (Π_b =56.5). The observation of geophysical and geochemical anomalies up to ~1000 km east of 91.5°W along the GSC suggest considerable upstream flow and Π_b>>100. Thus B=2000 kg/s is probably a minimum estimate of plume buoyancy flux.

CHAPTER III

CRUSTAL STRUCTURE BENEATH THE GALÁPAGOS ARCHIPELAGO FROM AMBIENT NOISE TOMOGRAPHY AND ITS IMPLICATIONS FOR PLUME-LITHOSPHERE INTERACTIONS

This chapter was coauthored by Douglas R. Toomey, Emilie Hooft Toomey and Sean C. Solomon

Villagómez D. R., D. R. Toomey, E. E. E. Hooft, and S. C. Solomon S. C., Crustal structure beneath the Galápagos Archipelago from ambient noise tomography and its implications for plume-lithosphere interactions, submitted to J. Geophys. Res.

3.1. Introduction

To investigate the nature of the crust beneath the Galápagos Archipelago we conducted a Rayleigh wave tomography with group velocities obtained from ambient noise records. Here we use high-frequency Rayleigh waves to image the regional seismic structure of the crust. Our results show anomalously low seismic velocities beneath the western archipelago between 3 and 13 km depth. The low velocities and the velocity-depth gradient are consistent with increased porosity and temperature in the crust beneath the western archipelago. We also integrate these findings with earlier surface-wave tomography results (Villagómez et al., 1997), recent plate reconstructions (Wilson and Hey, 1995; Barckhausen et al., 2001; Meschede and Barckhausen, 2001), and gravity

data (Sandwell and Smith, 1997). On the basis of this synthesis, we infer that many of the anomalous aspects of the Galápagos largely reflect the thickness and mechanical properties of the lithosphere that overlies the Galápagos plume.

3.2. Data and Methods

For this study we extracted continuous vertical-component records of seismic noise for 24 time periods from 11 to 50 days in duration between October 1999 and June 2002. We obtained estimates of the Rayleigh-wave group velocity between periods of 3 and 9 s from cross-correlations of pairs of noise records, from which we have inferred the shear-wave velocity structure and present thermal state of the crust.

3.2.1. Imaging of Rayleigh-Wave Group Velocity

We have used the ambient noise tomographic method to infer aspects of the seismic velocity structure beneath the archipelago. The cross-correlation of ambient noise at pairs of stations yields estimates of the inter-station Green's function, which for a station spacing between 30 and 500 km is dominated by Rayleigh waves (e.g., Shapiro and Campillo, 2004; Sabra et al., 2005; Shapiro et al., 2005). The cross-correlation technique is most effective when the noise amplitude is approximately uniform in space and time (Shapiro and Campillo, 2004; Sabra et al., 2005), so the effects of large seismic events should be minimized before calculating the cross-correlation. Two approaches can be taken to reduce the contribution of the most energetic arrivals: (1) We can

disregard the amplitude by keeping only the sign of the signals and correlating one-bit records (Larose et al., 2004; Malcolm et al., 2004); or (2) we can use a clipping threshold for each station (e.g., Sabra et al., 2005). We tried both approaches and found no significant differences in the cross-correlation signal or group velocity estimates in the observed frequency range. Here we present results from the first approach.

We measured the group velocity of Rayleigh waves derived from the station-pair cross-correlations using multiple filter analysis (MFA) (Herrmann and Ammon, 2002). MFA provides a graphical assessment of the peak group velocities in a range of periods, thus allowing a user to determine an appropriate dispersion curve. Each cross-correlation is filtered in a series of narrow passbands with a Gaussian filter of the form (Dziewonski et al., 1969):

$$H_n(\omega) = \exp\left[-\alpha\left(\frac{\omega-\omega_n}{\omega_n}\right)^2\right] \qquad (3.1),$$

where ω is frequency, ω_n is the center frequency of the filter, and α is a parameter that controls the width of the filter in the frequency domain. The group arrival time corresponds to the peak in the envelope of the filtered signal. The envelopes are contoured as functions of period and group velocity to aid in the identification of the dispersion curve. The success of the MFA method depends on the correct identification of the fundamental-mode dispersion curve and the appropriate truncation of measurements at short and long periods as the signal weakens (Herrmann and Ammon, 2002).

We used the group velocity measurements between pairs of stations to estimate both a regional average and lateral variations in group velocity. The propagation path is approximated by the geometric ray that connects the pair of stations. We consider this a good approximation to a more general approach that uses two-dimensional sensitivity kernels (Ritzwoller et al., 2002; Zhou et al., 2004), because we expect that at short periods and at regional scales both methods will recover similar structure (e.g., Ritzwoller et al., 2002).

To obtain lateral variations in group velocity (U), we parameterized the region as a series of blocks. The velocity U_L^j estimated along the j^{th} path between a pair of stations, L, can be expressed as:

$$U_L^j = \sum_{i=1}^{m} f_i^j \, U_i \qquad (3.2),$$

where f_i^j corresponds to the fraction of the j^{th} path that lies inside the i^{th} block, U_i is the velocity inside the i^{th} block, m is the total number of blocks or model parameters, and $\sum_{i=1}^{m} f_i^j = 1$.

In matrix form, equation (2) becomes

$$U_{L(nx1)} = F_{(nxm)} U_{(mx1)} \qquad (3.3),$$

where n is the total number of paths or observations, and the size of each matrix or vector is shown in parentheses. This is a linear system of equations, with a damped least squares solution (e.g., Tikhonov, 1943)

$$U = (F^T \mathrm{C_d}^{-1} F + \beta^2 I)^{-1} F^T C_d^{-1} U_L \quad (3.4),$$

where β is a weighting factor found by trial and error, and I is the identity matrix. C_d is the data covariance matrix, which, for uncorrelated velocity estimates, is equal to

$$(\mathbf{C}_d)_{ij} = \delta_{ij}\ \sigma_i^2 \quad (3.5),$$

where σ_i is the uncertainty in the determination of U_L^i and δ_{ij} is the Kronecker delta ($\delta_{ij}=0$ for $i \neq j$, $\delta_{ij}=1$ for $i=j$). For $\beta=0$, the problem reduces to a least-squares solution that depends only on the data. However, the least-squares approach to the linear problem does not guarantee positivity of the solution.

To ensure positivity we can sacrifice linearity by parameterizing the model in terms of r = ln (U) and finding a solution using an iterative method (e.g., Wilcock et al., 1995). To regularize the inversion, we included two types of model constraints. First, we penalized deviations from the starting velocity model using an a priori model covariance matrix of the form

$$(\mathbf{C}_m)_{ij} = \delta_{ij}\ \lambda_i^2 \quad (3.6),$$

where λ_i^2 is a weight equivalent to the a priori variance of the model parameters. Second, we apply a lateral smoothing constraint with a weight factor Δ as described in Wilcock et al. (1995).

To compare the results from different inversions we estimated the root mean square (RMS) misfit of the resulting model and the variance reduction with respect to a uniform velocity model, U_0. The RMS model misfit is defined as

$$\text{RMS misfit} = \sqrt{\frac{\left(U^{obs} - U^{pred}\right)^T C_d^{-1} \left(U^{obs} - U^{pred}\right)}{\text{Tr}(C_d^{-1})}} \qquad (3.7),$$

where Tr (C_d^{-1}) is the trace or sum of the diagonal elements of C_d^{-1}, U^{obs} are the observed values of U_L, and U^{pred} are the values predicted by the model. The weighted variance reduction (ν) is

$$v = 1 - \frac{\left(U^{obs} - U^{pred}\right)^T C_d^{-1} \left(U^{obs} - U^{pred}\right)}{\left(U^{obs} - U_0\right)^T C_d^{-1} \left(U^{obs} - U_0\right)} \qquad (3.8).$$

3.2.2. Inversion for Shear-Wave Velocity Structure

We inverted the estimates of group velocity as a function of period to obtain the shear wave velocity V_S as a function of depth using the methodology described in Villagómez et al. (2007). We performed inversions for one-dimensional structure for each dispersion curve by finding the best fit between the observed group velocities and those predicted by DISPER80 (Saito, 1988), which calculates normal modes for a laterally homogeneous model. The inversions solve for velocity perturbations from a starting model of V_S, P-wave velocity V_P, and density □ in an iterative process using the linearized inversion technique of Tarantola and Valette (1982). Since group velocities of Rayleigh waves are mostly sensitive to changes in shear wave velocity and less to changes in V_P or density, we solved for changes to the V_S model, and then we converted these to V_P using a fixed V_P/V_S ratio at each iteration. Because the problem is usually underdetermined, we imposed a priori information about the model parameters. We

included two types of constraints: (1) we penalize deviations from the starting velocity model using an a priori model covariance matrix with diagonal elements

$$(C_m)_{ii} = \eta_i^{\,2} \tag{3.9},$$

where η_i^2 is a weight equivalent to the a priori estimate of the standard deviation of the i^{th} velocity term in the inversion, and (2) we included a Gaussian smoothing constraint by introducing off-diagonal terms in C_m (e.g., Tarantola and Valette, 1982):

$$(C_m)_{ij} = \eta_i^{\,2}\ f_S \exp(-(D_i - D_j)^2/(2\theta^2))\ ,\ i \neq j \tag{3.10},$$

where D is depth, θ is the characteristic length of smoothing, and f_S is a weighting factor. An iterative solution is given by

$$\begin{aligned} V_{k+1} &= V_k + \delta V \\ \delta V &= [\ \mathbf{C}_m^{-1} + \mathbf{A}_{(k)}{}^T \mathbf{C}_d^{-1}\ \mathbf{A}_{(k)}\ ]^{-1}[\mathbf{C}_m^{-1}\ (V_0 - V_k) + \mathbf{A}_{(k)}{}^T \mathbf{C}_d^{-1}\ \left(U - U_{(k)}\right)] \end{aligned} \tag{3.11}.$$

where V_k is the velocity model at the k^{th} iteration, V_0 is the starting velocity model, δV is the perturbation to the velocity model, C_d is the data covariance matrix (as in equation 5), U are the group velocity observations (from equation 4), $U_{(k)}$ are the group velocities predicted by DISPER80 (Saito, 1988), and $A_{(k)}$ are the sensitivity kernels (∂U/∂V).

Provided that the constraints are appropriately weighted, the solution should converge in a few iterations. We estimated how each parameter is resolved in the inversion by inspecting the a posteriori model covariance

$$\mathbf{C_r} = [\ \mathbf{C}_m^{-1} + \mathbf{A}_{(k)}{}^T \mathbf{C}_d^{-1}\ \mathbf{A}_{(k)}\ ]^{-1} \tag{3.12}$$

and resolution

$$\mathbf{R} = [\ \mathbf{C}_m^{-1} + \mathbf{A}_{(k)}{}^T \mathbf{C}_d^{-1}\ \mathbf{A}_{(k)}\ ]^{-1}\ [\mathbf{A}_{(k)}{}^T \mathbf{C}_d^{-1}\ \mathbf{A}_{(k)}\ ] \qquad (3.13)$$

matrices. If a row of **R** is close to a delta function then the corresponding model parameter is well resolved, whereas if there are large off-diagonal elements for adjacent nodes the solution is spatially smoothed. In addition, the diagonal elements of **R** indicate how well the different model parameters are resolved, and the trace or sum of the diagonal elements of **R**, Tr (**R**), shows the number of independent pieces of information that are resolved in the inversion. We also determine the RMS misfit and variance reduction (equations 3.7-3.8) to compare the results of the different inversions.

3.3. Results

3.3.1. Estimation of Group Velocity

We applied the cross-correlation method to continuous vertical records from pairs of stations for 24 time periods that range from 11 to 50 days in duration between October 1999 and June 2002 (Table 3.1). The time periods were chosen in order to reduce the number of larger teleseismic events (surface wave magnitude $M_S > 7.0$), to avoid local swarms of earthquakes, and to maximize the number of stations available. We selected waveforms that had data gaps totaling less than 1 hour during the span of each record.

Coherent wavetrains emerge from the cross-correlation of ambient noise (Fig. 3.1). The wavetrains are two-sided, with amplitudes on either side varying in a manner dependent on the distribution of noise sources. Sabra et al. (2005) observed that for stations in southern California, given the network's vicinity to the Pacific coast, the

cross-correlation wavetrains are mostly one-sided and the signal-to-noise ratio is higher for station pairs oriented perpendicular to the coast. For the Galápagos, in order to place the side of greater amplitude at positive lag, cross-correlations between pairs of stations had to be performed using a southern-then-northern-station order for any time period considered (for example, cross-correlations of PAYG with G04, G05, G06 and G10; see Fig. 3.1a), indicating that the noise sources were located to the south of the seismic network. In addition, there are no significant temporal variations in the relative amplitude of the two sides, which suggests that the noise sources were mostly stationary. However, the relative amplitude of the two sides of the signal varies with period (Fig. 3.1b), indicating that the location of the noise sources may be frequency dependent. Additional analysis of amplitude variations with azimuth and period in a future study could help constrain the location of the sources of noise.

At the station spacing in our network (between 65 and 250 km) the cross-correlation is dominated by Rayleigh waves (Shapiro and Campillo, 2004; Sabra et al. 2005). The group arrivals are easily seen on the cross-correlations, which predictably arrive later for stations separated by greater distances (Fig. 3.1a). Filtering of the signal shows the dispersion of the Rayleigh wave velocity by period (Fig. 3.1b). Considering the entire data set, we obtained reliable measurements of group velocity for periods between ~3 and ~10 s, in the band of ocean-generated microseismic noise (Friedrich et al., 1998). For this period band, the group velocity of Rayleigh waves is primarily sensitive to V_S structure between 2 and 12 km depth (Fig. 3.2).

Time period	Number of days	Stations missing data or with data gaps
1999/10/06 - 1999/10/31	26	G09
1999/11/25 - 1999/12/05	11	G09
2000/01/18 - 2000/02/10	24	G04 G07
2000/02/01 - 2000/03/03	32	G04 G07
2000/03/05 - 2000/04/01	28	G04 G07 PAYG
2000/04/13 - 2000/05/19	37	G07 G10
2000/06/24 - 2000/07/06	13	G03 G07 G10
2000/07/18 - 2000/08/27	41	G01 G03 G07 G10
2000/10/05 - 2000/10/24	20	G01 G07
2000/10/05 - 2000/11/10	37	G01 G07
2000/11/19 - 2000/12/05	17	G01 G07 PAYG
2001/01/19 - 2001/02/12	25	G01 G03 G07
2001/03/02 - 2001/03/31	30	G01 G03 G07
2001/05/26 - 2001/06/22	28	G01 G03 G07 G10
2001/09/23 - 2001/10/18	26	G07 PAYG
2001/10/22 - 2001/12/10	50	G07 PAYG
2001/12/19 - 2002/01/10	23	G07 G09 PAYG
2002/01/11 - 2002/02/10	31	G07 G09 PAYG
2002/02/11 - 2002/03/01	19	G07 G09
2002/03/07 - 2002/03/22	16	G07 G09
2002/04/02 - 2002/04/25	24	G01 G07 PAYG
2002/04/27 - 2002/05/27	31	G01 G04 G06 G07
2002/06/04 - 2002/06/28	25	G01 G04 G06 G07

Table 3.1. Time periods used for cross-correlation of ambient noise records

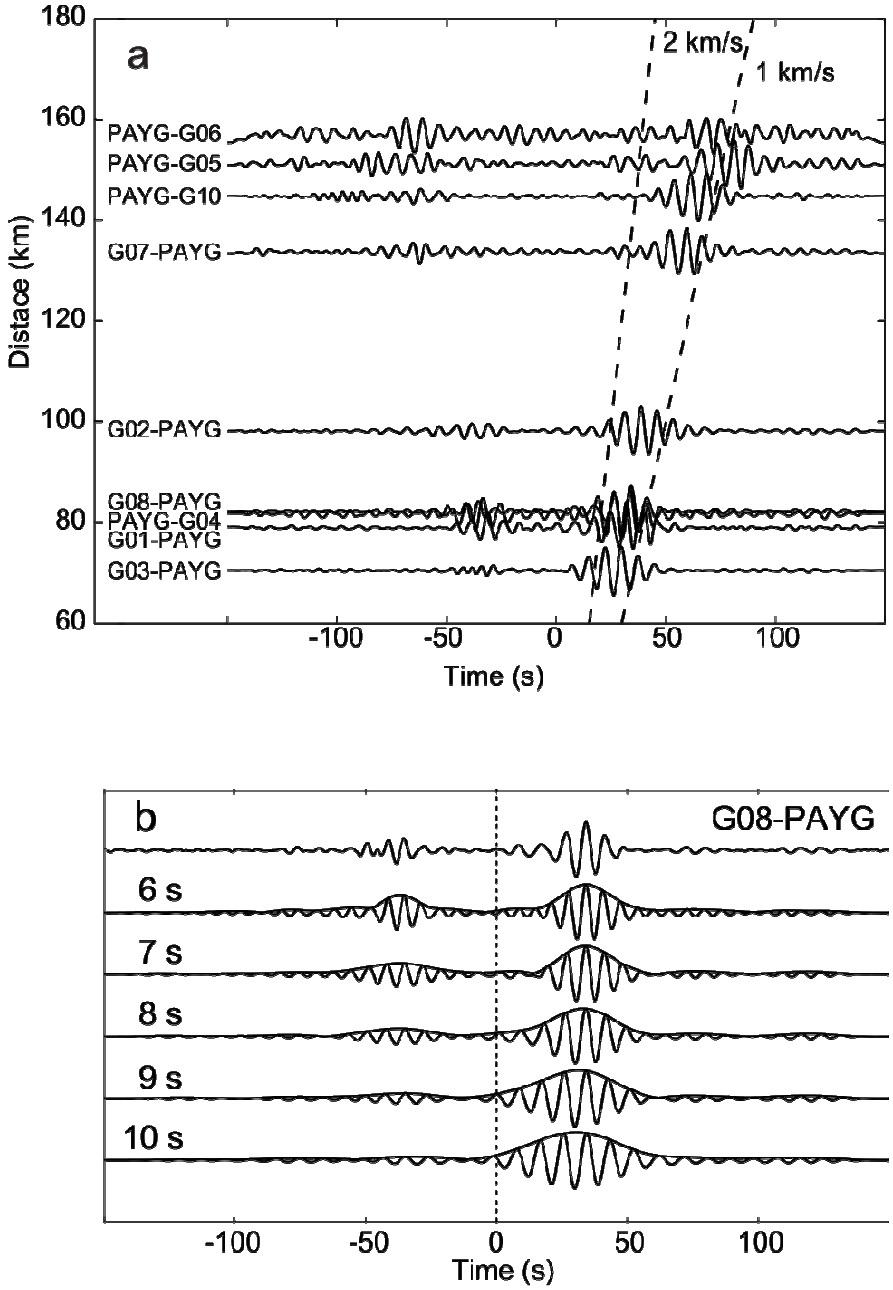

Fig. 3.1. (a) Cross-correlations of 26 days of seismic ambient noise records (1999/10/06 - 1999/10/31) for pairs of stations that include PAYG. The horizontal axis is correlation lag time, and the vertical axis is the distance between stations. Dashed lines indicate velocities of 1 and 2 km/s. (b) Unfiltered (top) and filtered signals (with envelopes) at periods of 6, 7, 8, 9, and 10 s for the G08-PAYG cross-correlations shown in Fig. 2a. The horizontal axis is the correlation time lag.

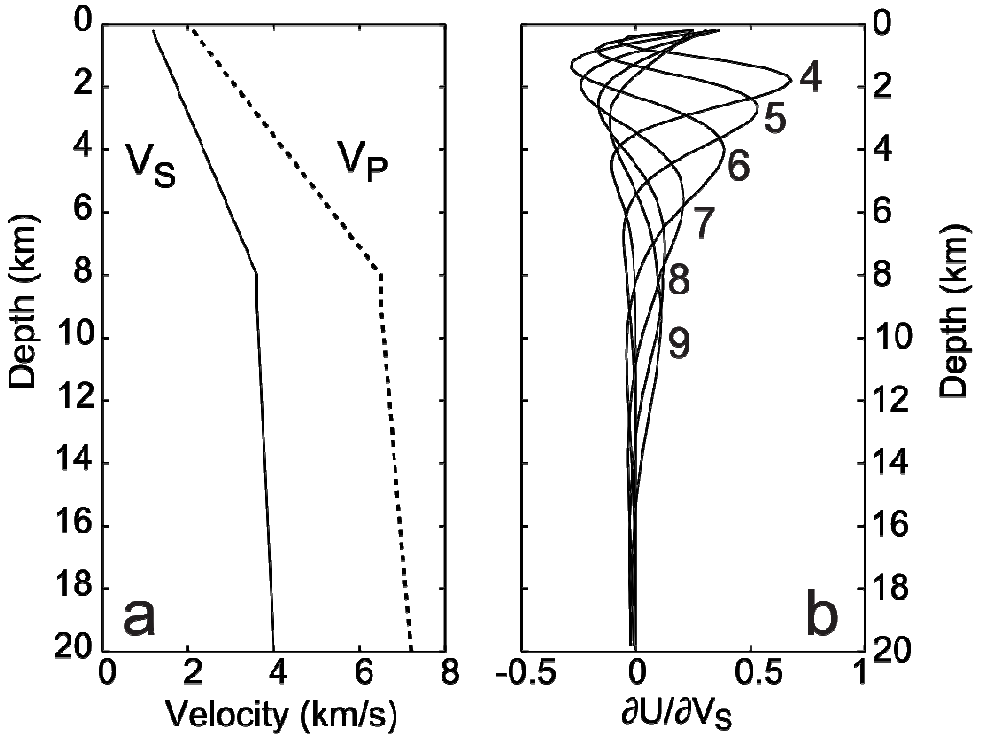

Fig. 3.2. (a) Nominal model for V_P and V_S versus depth. (b) Sensitivity of Rayleigh wave group velocity to changes in V_S for the velocity model in (a). Numbers indicate period in seconds.

Examples of group velocity measurements obtained with MFA are shown in Fig 3.3. We used the higher-amplitude half of the symmetric signal and filter it using α=25 in equation (1) for periods between 2 and 12 s. The amplitude of the envelope was contoured as a function of period and group velocity, and the local maxima of the envelope are marked. The plotting aids in the identification of the dispersion curve for the fundamental mode, which corresponds to the maximum amplitude, and helps to identify the range of periods where the signal is strongest. We chose only measurements where the amplitude is more than 10% of the maximum amplitude when estimating a dispersion curve. Fig. 3.3 shows MFA measurements of group velocity for two stations pairs, G03-

G01 and G03-G07, for the time period between 1999/10/06 and 1999/10/31. The resulting dispersion curves are shown in Figs. 3.3a and 3.3c.

We determined group velocity dispersion curves for all stations pairs and for all the time periods considered. Additionally, we stacked the cross-correlations for each station pair, and we measured the group velocities from the stacked signal (Fig. 3.4a). Stacking decreases the influence of potential seasonal variations in the source of noise and increases the signal-to-noise ratio of the cross-correlation. Although the envelope of the cross-correlation is generally broad (e.g., Fig.3.3a and 3.3c), which makes the identification of the maxima more challenging, multiple measurements of group velocity for each station pair at different time periods agree well (Fig. 3.4b). A comparison of group velocities measured from individual time periods with the stacked signal provides an estimate of uncertainty arising from repeatability of the measurement. We estimate that the group velocity uncertainty is less than ±0.15 km/s.

The average of the measurements for all station pairs gives us an average group velocity dispersion curve for the entire Galápagos platform (Fig. 3.5a). We computed the uncertainty of this measurement as a function of period by taking the RMS of all the individual station-pair uncertainties. We used only those periods where the number of paths exceeded 20 (out of the possible 55), which fell between 3.5 and 9.5 s (Fig. 3.5b). Fig 3.5a shows that the Rayleigh wave group velocity increases from 1.85 km/s to 2.45 km/s between periods of 3.5 and 9.5 s.

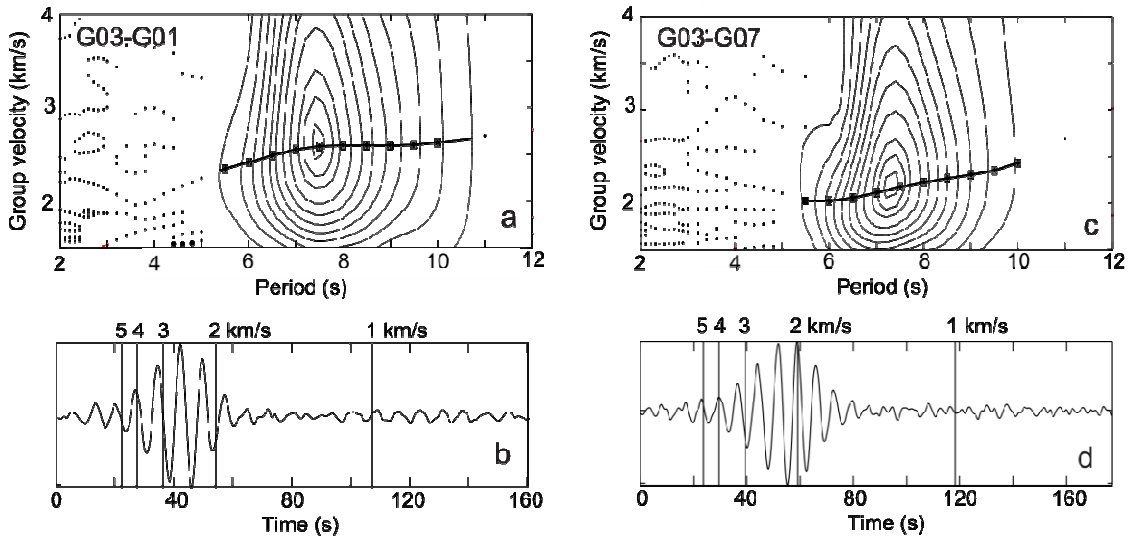

Fig. 3.3. Results of multiple filter analysis (MFA) (Herrmann and Ammon, 2002) performed on the positive side of the correlation time-lag of two cross-correlations (1999/10/06 - 1999/10/31) for the station pairs: (a-b) G03-G01 and (c-d) G03-G07. The bottom figures (b and d) show the unfiltered signal and the location in time of group velocity values from 1 to 5 km/s (red lines). The top figures (a and c) show contours of the envelope of the filtered signal as functions of period and group velocity. Contours represent 10% to 90% (in increments of 10%), 95%, and 99% of the maximum amplitude. Dots indicate locations of local maxima in the envelope. Lines with squares show the best estimates of the dispersion curves.

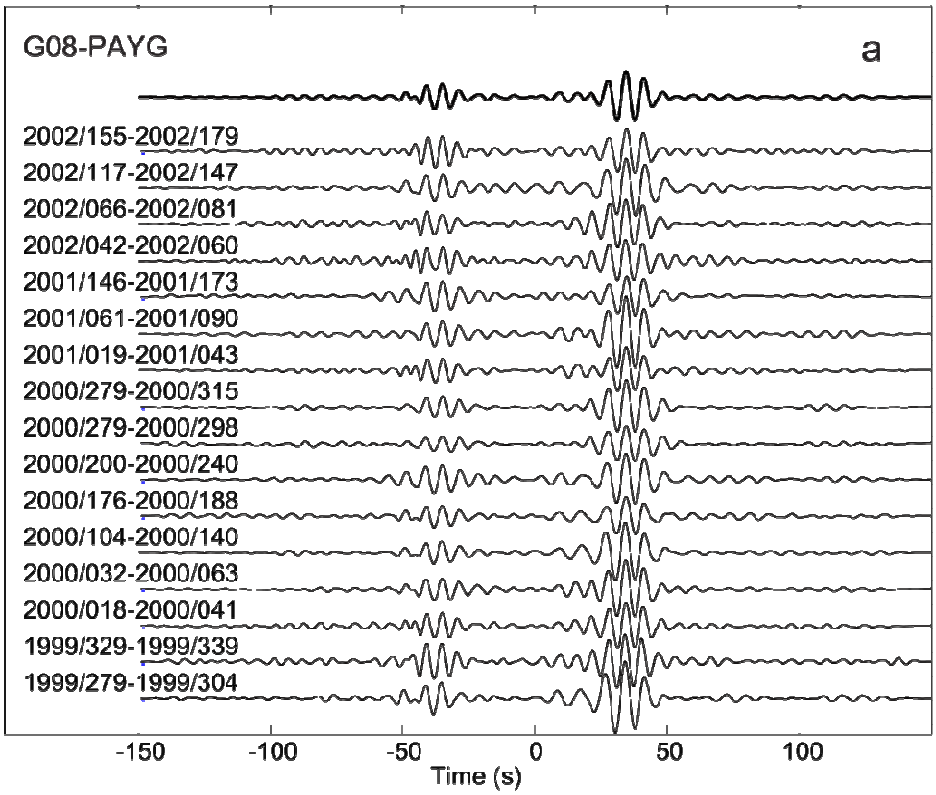

Fig. 3.4. (a) Cross-correlations of ambient seismic noise records between G08 and PAYG for time periods shown to the left. Line on top shows the stacked signal resulting from taking the mean of all cross-correlations. (b) Result of MFA performed on the right side of the cross-correlations shown in (a) at different time periods and on the stacked signal (thick line). The curves are truncated at low and high periods to keep only amplitudes greater than 10% of the maximum.

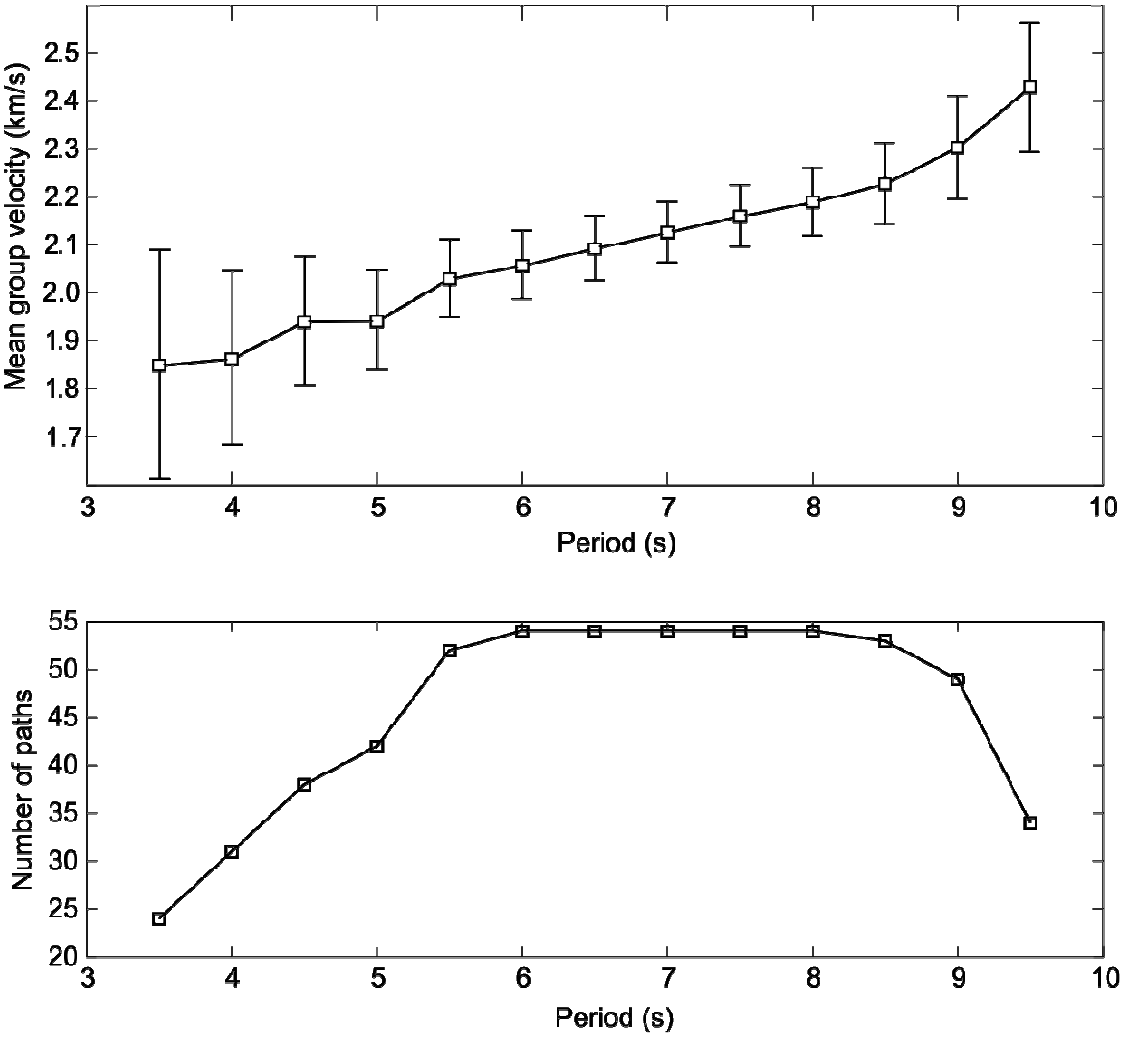

Fig. 3.5. (a) Average dispersion curve for the entire archipelago computed from MFA results from station-pair stacked cross-correlations. Error bars indicate one standard deviation. (b) Number of station pairs used to calculate the mean as a function of period.

Compared with the average velocity, the group velocities between pairs of stations in the western archipelago are generally lower than those in the eastern archipelago (Figs. 3.6 and 3.7). For example, the G04-G05, G05-G06, and G05-G07 paths in the western archipelago are 0.3-0.7 km/s lower than the average at all periods, while the G01-G03, G02-G09 and G09-PAYG paths in the eastern archipelago are 0.3-

0.4 km/s higher than the average (Fig. 3.6). The differences in group velocity between the paths in the western and eastern archipelagos are 4 to 6 times larger than the estimated uncertainty in the measurement of the group velocity (0.15 km/s). Fig. 3.7 shows all the paths between station pairs for periods between 4 and 9 s, with red lines indicating group velocities lower than the average, and blue higher than average. The difference between the eastern and western archipelago is substantial, with variations in group velocity of up to ±30% from the average (Fig. 3.6).

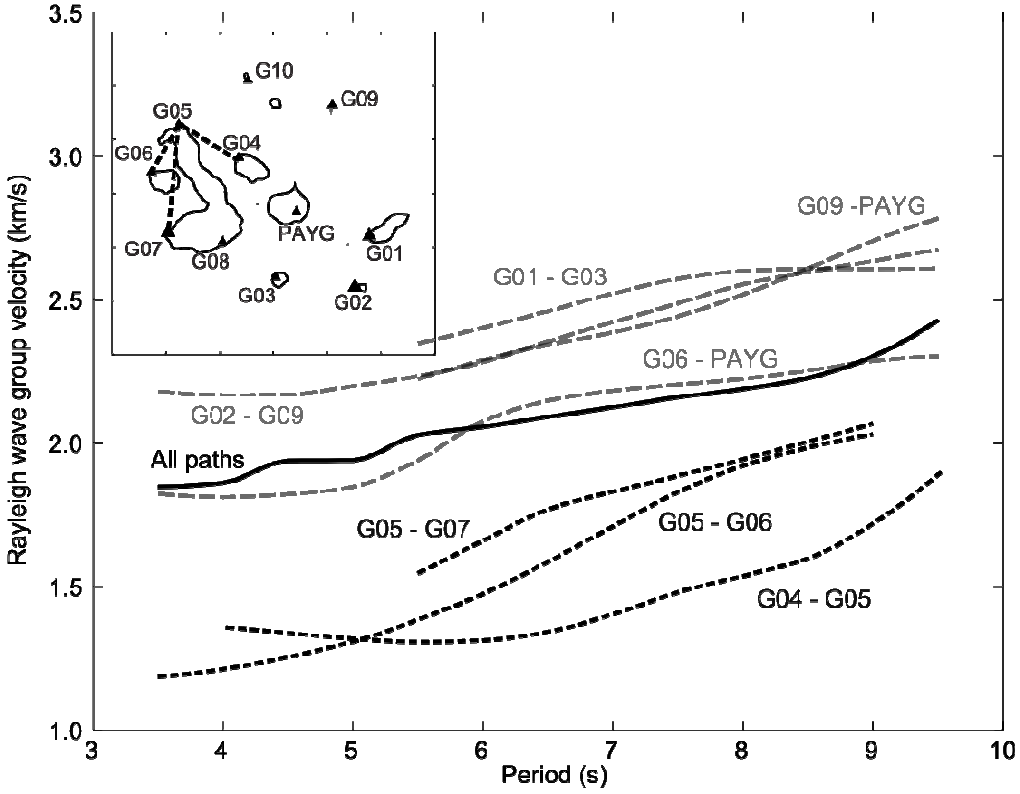

Fig. 3.6. Smoothed dispersion curves for selected station pairs compared with the average for the region (thick black line). The inset shows the locations of the stations and paths represented.

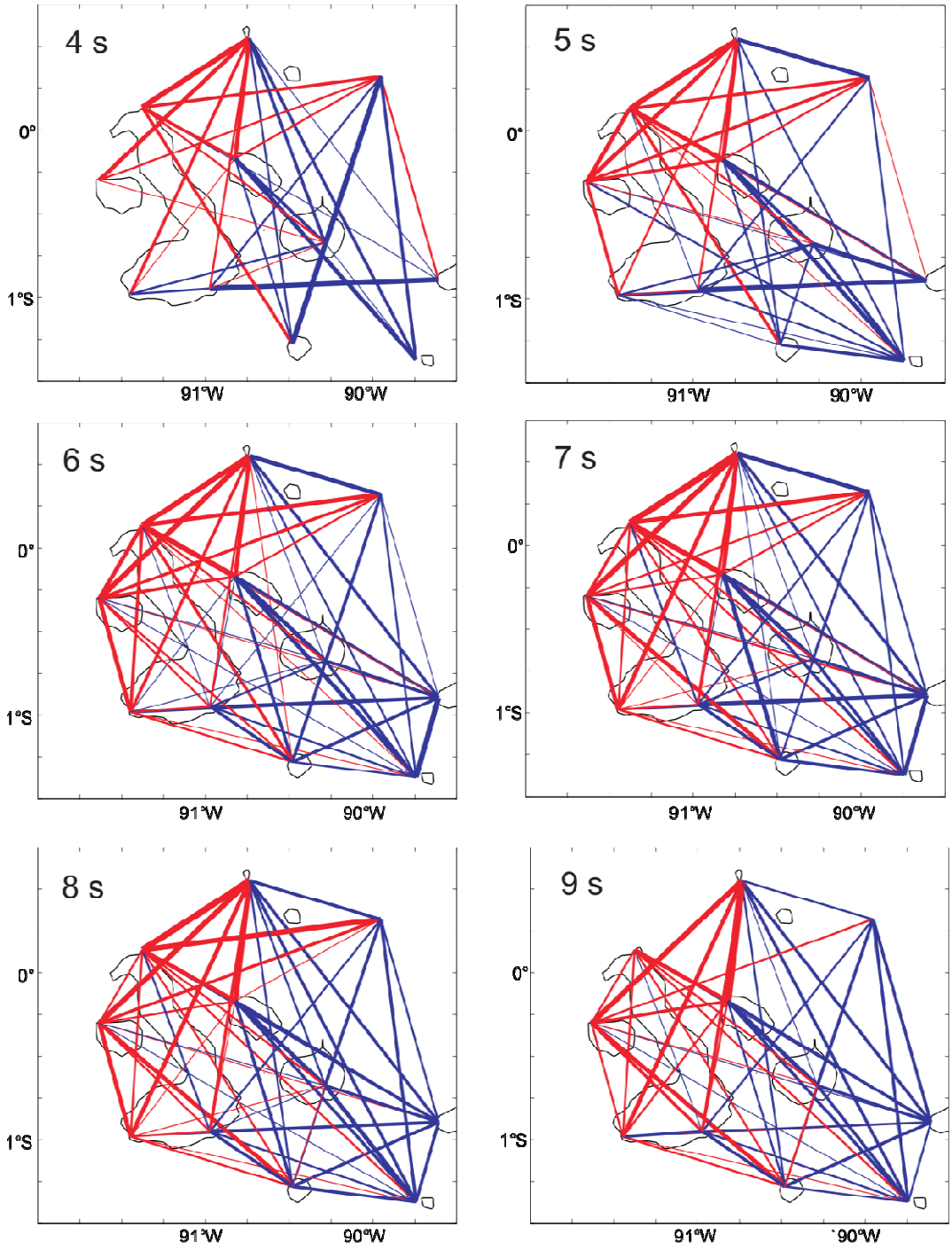

Fig. 3.7. Maps of paths along which group velocity measurements were determined at periods between 4 and 9 s. Red colors indicate that the group velocity is less than the average velocity, whereas blue colors indicate velocities higher than average. Thickness of the line is proportional to the difference between the group velocity and the average.

To determine lateral variations in group velocity structure, we inverted the group velocity measurements for all station pairs at 13 different periods (from 3.5 to 9.5 s). We used the average dispersion curve in Fig. 6a as the starting model in the inversions, and we parameterized the region using two-dimensional blocks. In initial inversions the region was parameterized as two blocks, one each in the eastern and western parts of the archipelago (Fig. 3.8a). We found the velocities using a damped least-squares approach with β=0.1 in equation (4), and we estimated model uncertainties with a Monte Carlo approach (e.g., Metropolis and Ulam, 1949; Mosegaard and Tarantola, 1995). The results of the inversion show a clear distinction between the western and eastern blocks (Fig. 3.8b). Group velocities in the western block are 40-50% lower than in the eastern block. Moreover, the variance reduction of using two blocks compared to a uniform velocity model is 59% (total RMS misfit = 0.24 km/s), indicating that most of variability in the observations is due to differences between the eastern and western archipelago.

We next parameterized the region with four blocks (southwestern or SW, southeastern or SE, northwestern or NW, and northeastern or NE) to investigate north-south differences in group velocity (Fig. 3.8c). We again used a damped least-squares approach with α=0.1. The results show that the northern blocks are about 15-25% lower in average group velocity than their respective southern blocks (Fig. 3.8d). The northwestern archipelago is the lowest-velocity region, with group velocities that are 25-45% lower than the average, while the southeastern archipelago is the highest-velocity region, with velocities that are 10-25% higher than the average. The variance reduction obtained using this model with respect to a uniform velocity model is 70% (total RMS

misfit = 0.21 km/s), suggesting that there are important differences in velocity in the north-south direction.

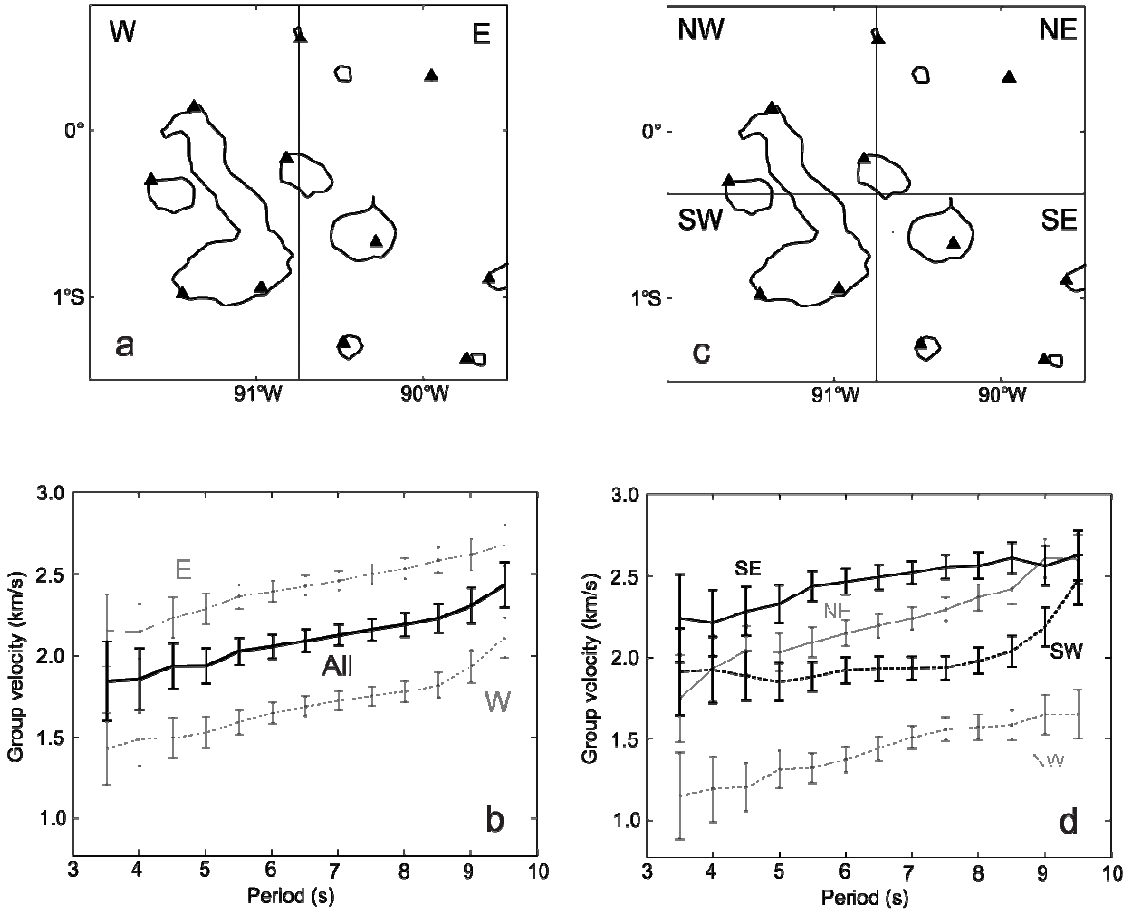

Fig. 3.8. (a and b) Results of group velocity inversions when the region is divided into the two blocks in (a). (b) Dispersion curves for the two blocks (dashed gray for western archipelago and solid gray for eastern archipelago) compared with the average dispersion curve (thick black line). (c and d) Results of group velocity inversions when the region is divided into the four blocks shown in (c). (d) Dispersion curves for the four blocks (dashed gray for NW, dashed black for SW, solid gray for NE, solid black for SE). Error bars represent one standard deviation.

We then ran inversions using blocks of 0.25° in latitude and longitude. Because damped least squares does not guarantee the positivity of the solution in each block, we parameterized the group velocity (U) in terms of $r = \ln(U)$ and used an iterative inversion (e.g., Wilcock et al., 1995). Inversions with λ_i varying between 0.01 and 0.5 and no lateral smoothing (Δ=0) show misfit varying from 0.068 to 0.152 km/s (variance reduction from 75% to 97%). The results of these inversions are consistent with those of the previous inversions, with the lowest group velocities in the northwestern archipelago. This area coincides with a region of deep bathymetry (greater than 2000 m) (Fig. 1.1), suggesting that water depth could be responsible for some of the low group velocities observed.

We conclude that most of the variance reduction was gained in the first inversion with two blocks, so the greatest spatial variability of seismic velocities is in the east-west direction. However, our inversion procedure cannot determine if the group velocity increase observed from west to east is gradual or abrupt. To address this issue, we estimated average group velocities for each station and analyzed their variations by longitude (Fig. 3.9). We calculated the averages using all the station-pair group velocities associated with a particular station. We found that the group velocity gradually increases from west to east. The average rate of increase from the best fitting line is 0.32 km/s per degree of longitude (0.27 km/s per degree) at a period of 6 s (8 s).

To study the possible effects of crustal azimuthal anisotropy on the propagation of Rayleigh waves, we analyzed the group velocity residuals for a potential cos (2θ) dependence, where θ is the azimuth from north of the station-pair path. We found no

dependence, suggesting either that the crust is azimuthally isotropic or that azimuthal anisotropy cannot be resolved with the current data set.

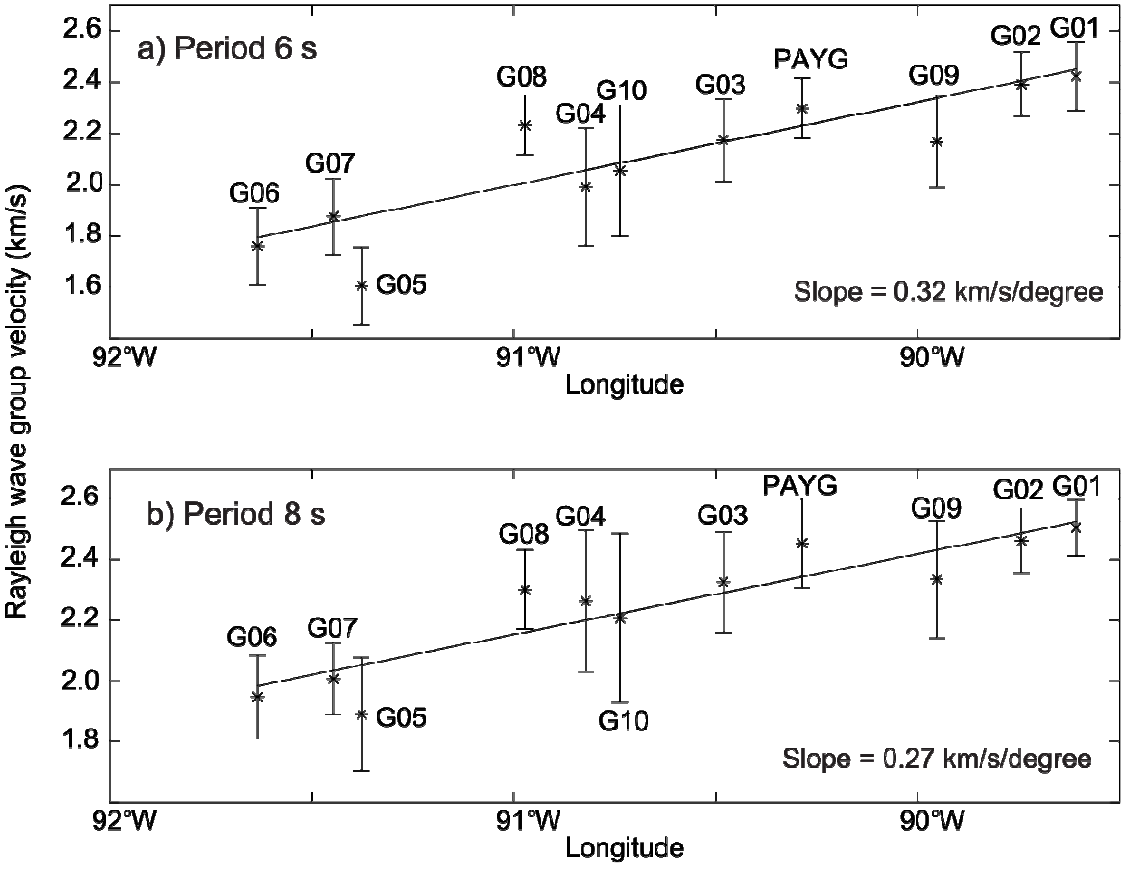

Fig. 3.9. Average value of Rayleigh-wave group velocity for each station at a period of (a) 4 s and (b) 6 s, plotted as functions of longitude. The averages are calculated from the group velocities measured for all station pairs that include the respective station. Error bars indicate one standard deviation.

3.3.2. Inversions for V_S

We inverted the average dispersion curve and those of the different subregions (Fig. 3.8) to obtain profiles of V_S versus depth. The models are parameterized at depth in increments of 250 m between 0 and 20 km depth. For the starting model and during the inversion we used a constant value of V_P/V_S=1.8, and we approximated density using ρ (kg/m^3) = 3810-6000/V_P (Carlson and Herrick, 1990). Although V_P/V_S likely varies with depth, the inversion is more sensitive to changes in V_S than to V_P or density, so different choices of V_P/V_S or density do not markedly change the results.

We first inverted the average dispersion curve (black line in Fig. 3.8b), and we analyzed the effects of changing the starting model. Fig. 3.10a shows the results of nine inversions (η_i = 0.3, θ = 7.5 km, and f_S = 0.3) using different starting models (dashed lines). The results indicate that the V_S model is independent of the starting model and relatively well constrained between 2 and 12 km depth (dashed horizontal lines). This behavior is also illustrated in Fig. 3.10b, which shows that the average resolution decreases with depth from a maximum at 2 km depth to zero at 16 km depth.

The number of observations in the inversion (n=13) indicates that we can potentially recover a maximum of 13 pieces of information about the V_S model. However, the observed group velocities are not independent observations. The trace of the resolution matrix, Tr (**R**) = 2.3, shows that we can only recover ~2 independent pieces of information about the model. To examine the dependence of different model parameters on information at adjacent layers, we inspect the rows of the resolution matrix (Fig. 3.10c). For instance, the value of V_S recovered at 8 km depth is a weighted average

of seismic structure between 4 and 12 km depth (dashed curve in Fig. 3.10c), whereas the value of V_S at 3 km depth is a weighted average of structure in the upper 6 km (solid curve in Fig. 3.10c).

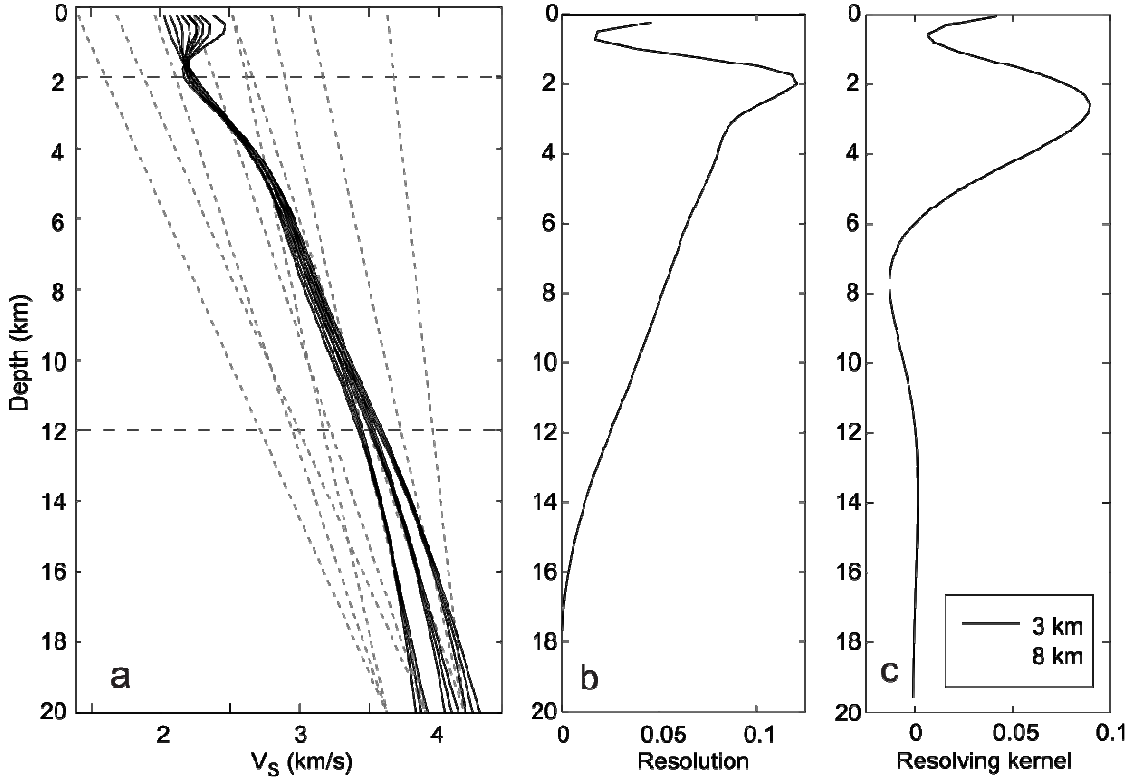

Fig. 3.10. Results of inversions for V_S of the regional average Rayleigh-wave group velocity (Fig. 6a) using η=0.3 and Δ=7.5 km. (a) Black lines show V_S as a function of depth. Dashed lines indicate starting velocity models for the inversion. Dashed horizontal lines represent the assumed depth range of best resolution. (b) Resolution (diagonal elements of resolution matrix) as a function of depth. (c) Resolution kernels (rows of the resolution matrix) at depths of 3 and 8 km.

The results of inverting the dispersion curves for the western and eastern archipelago are compared with that for the average of the entire archipelago in Fig. 3.11.

A first set of inversions (Fig. 3.11a,b) does not take into account the effect of the average water depth in the Galápagos Archipelago, which can significantly alter the group velocities of Rayleigh waves at the periods considered here. For example, Fig. 3.12 shows the effect on the group velocity estimates when the top of the velocity model shown in the figure insert is replaced by water columns of thickness 750 m and 2000 m (V_P = 1.5 km/s, V_S = 0, ρ = 1000 km/m^3). The addition of a water column having a thickness of up to 2000 m has the effect of decreasing the group velocity estimates for periods less than 12 s.

The results of the inversions when a column of water is added to the top of the model are shown in Fig. 3.11c,d. In each case we approximate the average depth to the sea floor in each block: 1250 m for the western block, 1000 m for the eastern block, and 1000 m for the entire archipelago. The addition of the column of water increases the V_S estimate by 10-20% at depths shallower than ~6 km but has little effect in the deeper part of the model. In general, the misfit improves when the inversions account for water depth (Table 3.2). Because there is no resolution in the water column, the depth range of best resolution shifts from 2-12 km to approximately 3-13 km depth (dashed horizontal lines in Fig. 3.11c). Given the inclusion of the water column in the inversions, all depth estimates discussed below are with respect to sea level.

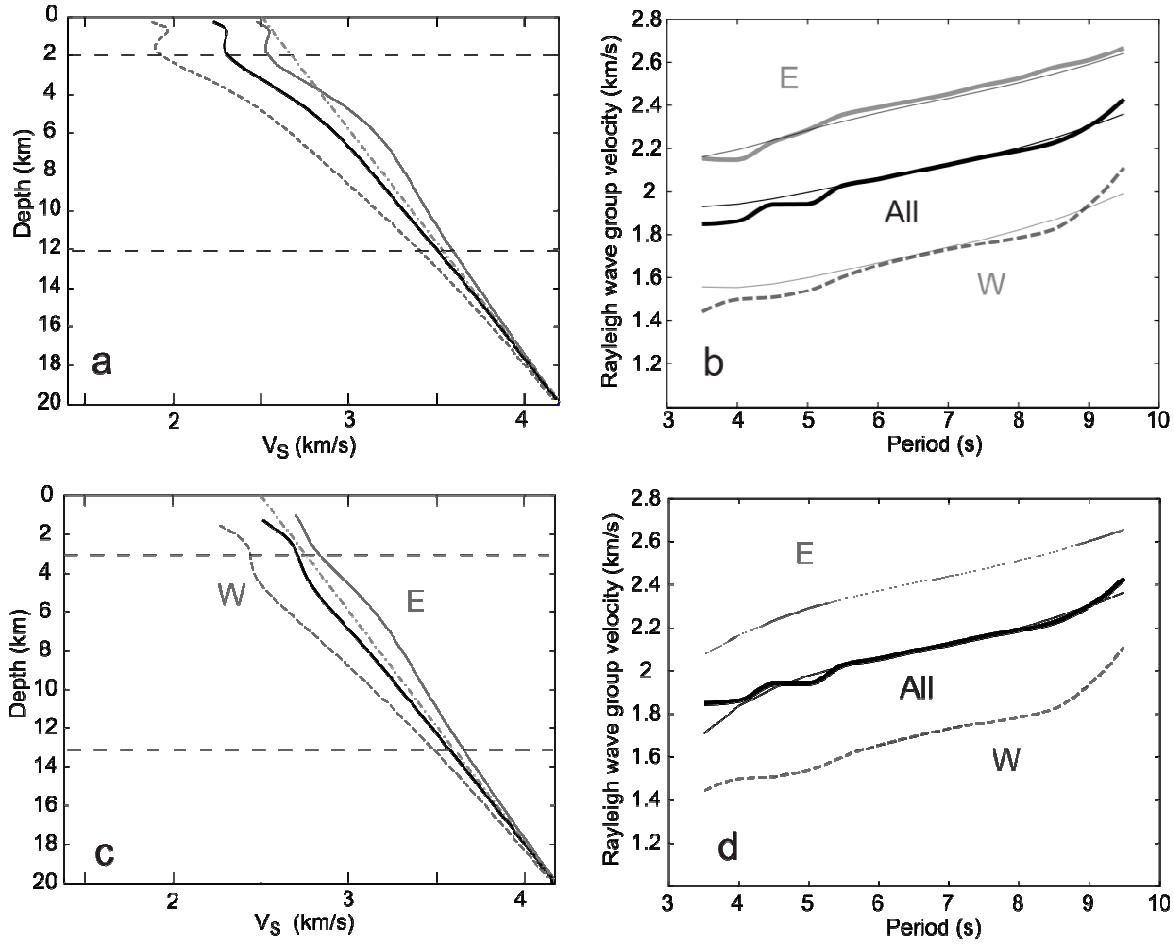

Fig. 3.11. Results of inversions for V_S of Rayleigh-wave group velocity for the regional average and the eastern and western archipelagos, (a and b) when the water column is not taken into account and (c and d) accounting for the presence of a water column at the top of the model. (a) and (c) show the resulting regional average V_S model (black line) as well as models for the western (dashed gray line) and eastern archipelagos (solid gray line). Dashed-dotted lines show the initial model used in the inversions. Dotted horizontal lines denote upper and lower bounds on the depth range of best resolution. (b and d) Observed (thick lines) and predicted (thin lines) dispersion curves.

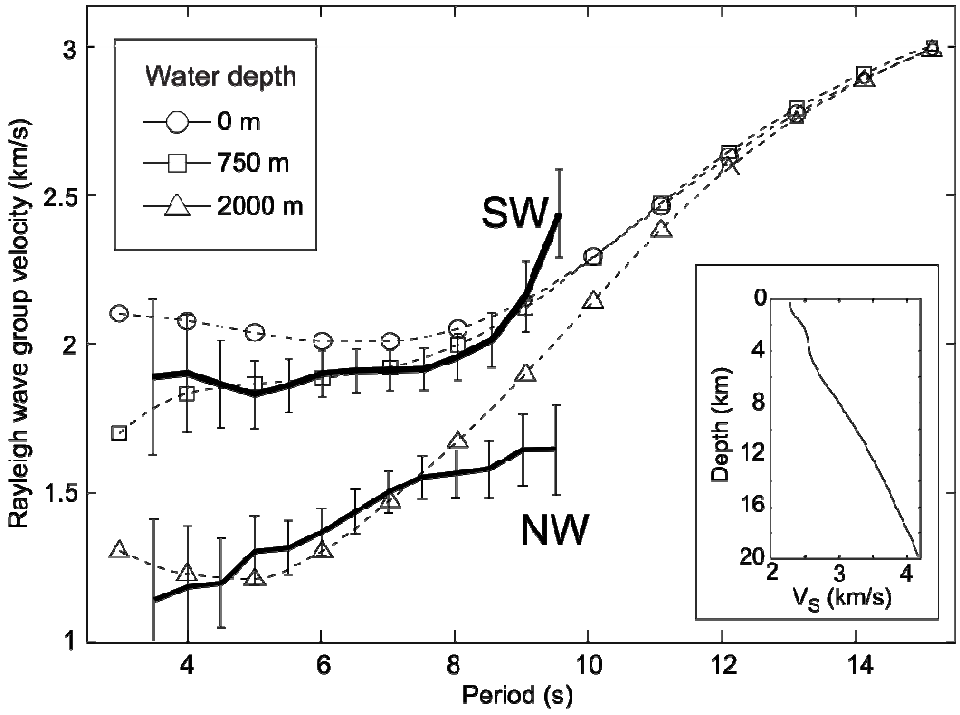

Fig. 3.12. Effect on the group velocity (dashed lines) of adding a column of water (V_P = 1.5 km/s, V_S = 0 km/s) to the top of the velocity model shown in the insert. Circles indicate no water column, squares indicate a 750-m-deep water column, and triangles indicate a 2000-m-deep water column. Thick lines with error bars show the observed group velocities beneath the SW and NW blocks.

Next we inverted the dispersion curves for the four different blocks in Fig. 3.8c-d, without and with a water column. Overall the fit to the observed group velocities improves when a water layer is added to the top of the model (Table 3.2). However, inversions for the NW block with a water layer of 2000 m fail to converge or to produce a good fit to the observations. Nevertheless, Fig. 3.12 shows that the group velocities for both the SW and NW blocks can be fit relatively well using the same velocity model (figure insert, result of the SW inversion), just by accounting for the different depth of the water layer. Hereafter we assume that this velocity profile corresponds to the entire

western archipelago. In contrast, the group velocities observed in the NE and SE blocks cannot be explained with only a single V_S model as in the west, suggesting that there are substantial north-south differences in crustal V_S in the eastern archipelago.

	RMS misfit (km/s), no water layer	RMS misfit (km/s), with water layer	Water layer (m)
Entire archipelago	0.0723	0.0640	1000
Western (W)	0.0628	0.0677	1250
Eastern (E)	0.0618	0.0552	1000
Southwestern (SW)	0.0827	0.0762	750
Northwestern (NW)	0.0832	N/A	2000
Southeastern (SE)	0.0811	0.0891	1000
Northeastern (NE)	0.0858	0.0822	1250

Table 3.2. RMS misfit of inversions for V_S

The results of the inversions for V_S are summarized in Fig. 3.13. The average V_S in the entire archipelago varies from 2.7 to 3.6 km/s between 3 and 13 km depth below sea level. On average, V_S beneath the western archipelago is 15% lower than beneath the eastern archipelago at 3-8 km depth, and 8% lower at 8-13 km depth. To the east, V_S beneath the northern block is on average 5% lower than beneath the southern block at 3-8 km depth, and 1% lower at 8-13 km depth.

The highest V_S is found beneath the southeastern archipelago (Fig. 3.8 and Fig. 3.13), a region where Feighner and Richards (1994) estimated the crust to be thickest (thickness > 16 km, their Fig. 12). To estimate the effect of crustal thickness on our velocity results, we ran a series of inversions for V_S inversions with different crustal thicknesses. We varied crustal thickness from 14 to 20 km and fixed V_S in the upper mantle to values between 4 and 4.5 km/s (V_P between 7.2 and 8.1 km/s). We found that constraining the thickness of the crust does not have an effect on V_S resolved between 3 and 13 km depth, a result consistent with the small sensitivity of the inversion to structure deeper than 13 km depth. This outcome suggests that the north-south difference in velocity that we observed beneath the eastern archipelago is dominantly the result of variations in the seismic velocity structure of the crust between 3 and 13 km depth rather than by variations in crustal thickness.

To test how the V_S model is resolved with depth, we also ran series of synthetic inversions. The results, shown in Fig. 3.14, confirm that without the addition of a water column the model is best resolved between 2 and 12 km depth (dashed horizontal lines). In addition, because the velocity in all our starting models increases linearly with depth we wanted to test how a change in velocity gradient is resolved in the inversions for V_S. We find that the change in gradient can be resolved, especially if it occurs above ~10 km depth (Fig. 3.14c), suggesting that there are no evident changes in velocity gradient with depth between 3 and 10 km depth beneath the Galápagos.

Crustal velocities beneath the Galápagos are lower than those of very young oceanic crust at the East Pacific Rise (EPR), and comparable to those of Hawaii (Fig. 3.15). Fig.3.15a shows a comparison of V_P (under the assumption that V_P/V_S=1.8) as a

function of depth relative to sea level for the Galápagos Archipelago, 0–200-kyr-old crust at 9°N at the EPR (Vera et al., 1990), and 150–350-kyr-old crust on the eastern and western sides of the EPR (at 9°10'N for the outer western profile and at 9°50'N for the outer eastern profile of Canales et al. (2003)). Crustal V_P inferred beneath the Galápagos is up to 20% lower than the western side of the EPR, and up to 25% lower than either 0–200-kyr-old EPR crust or the eastern side of the EPR (Fig. 3.15a). The difference in V_P between the Galápagos and the EPR is still substantial if V_P/V_S is taken to range from as low as 1.6 to as high as 2.0 (by as much as 45% and 15%, respectively), either for a constant V_P/V_S or allowing that ratio to vary with depth.

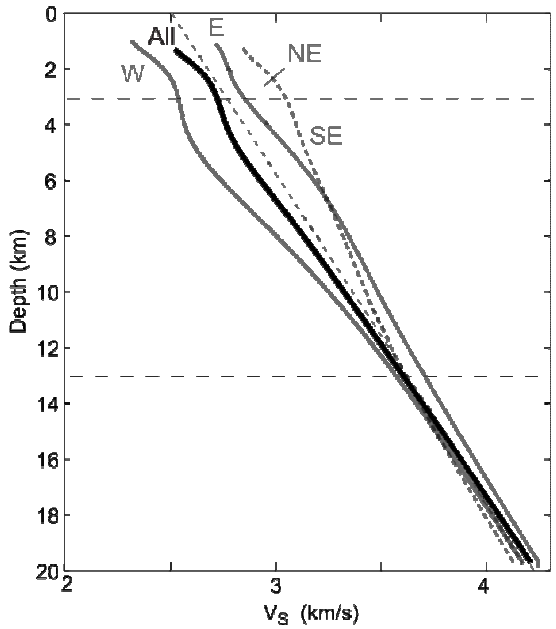

Fig. 3.13. Summary of results of inversions for V_S when the water layer is taken into account: average V_S for the entire archipelago (black line) and V_S for blocks in the west and east (solid gray), and northeast and southeast (dashed gray). Dotted horizontal lines denote upper and lower bounds on the depth range of best resolution.

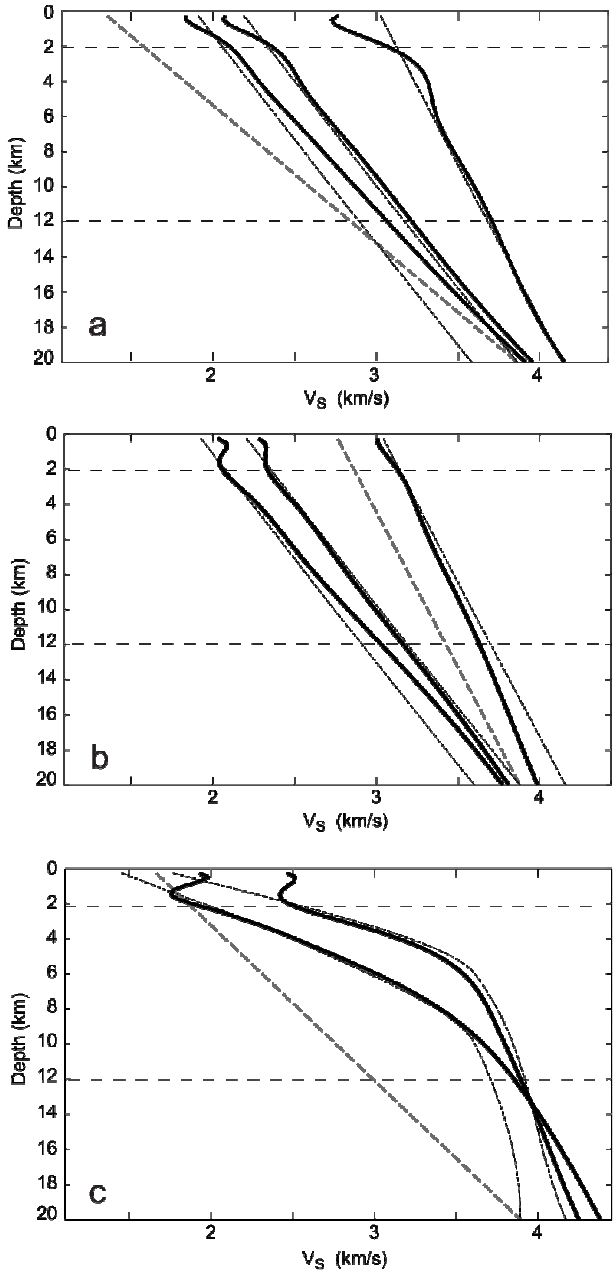

Fig. 3.14. Synthetic inversions for V_S. Thin black lines show the synthetic velocity models, and thick lines indicate the results of the inversions. Dashed lines show the starting model for the synthetic inversions in each panel. Horizontal dashed lines in (a) delimit the inferred region of best resolution (2-12 km depth).

3.4. Discussion

3.4.1. Crustal Structure

Compared with a one-dimensional V_P profile for southern Hawaii (Klein, 1981), crustal V_P inferred for the Galápagos Archipelago is up to 7% higher between 3 and 8 km depth, but similar between 8 and 13 km depth (Fig. 3.15b). In contrast, crustal V_P beneath the eastern archipelago is up to 8% lower than that of the western Carnegie Ridge at ~85°W, 250 km east of the Galápagos hotspot (Sallarès et al., 2005), and up to 10% lower than that determined at Oahu, 200 km from the Hawaiian hotspot (ten Brink and Brocher, 1987) (Fig. 3.15b).

We suggest that the lower-than-normal crustal seismic velocities beneath the Galápagos are caused by a combination of heating by increased intrusive activity in the lower crust due to the injection of hotspot material above a Galápagos plume and the construction of a highly porous volcanic platform emplaced on top of the pre-existing oceanic crust. These combined effects are responsible for the thickening of the crust beneath the Galápagos from ~6 km to the west of the archipelago to ~16 km near the center (Feighner and Richards, 1994; Toomey et al., 2001).

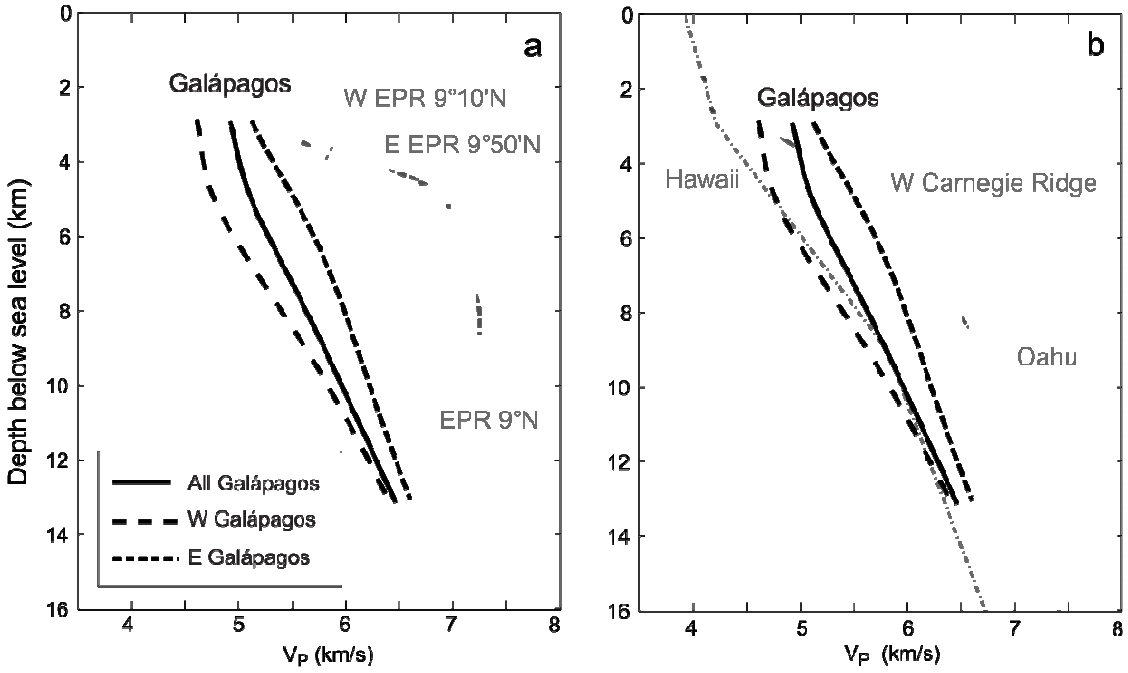

Fig. 3.15. Comparison of crustal V_P models beneath the Galápagos (solid and dashed black lines) with (a) estimates for 0–200-kyr-old crust at 9°N along the EPR (dashed grayline) (Vera et al., 1990), and of 150–350-kyr-old crust on both the eastern and western (E and W, solid gray lines) sides of the EPR (at 9°10'N for the outer western profile and at 9°50'N for the outer eastern profile of Canales et al. (2003)), and (b) those estimated beneath the western Carnegie Ridge (slid gray line) (Sallarés et al., 2005), southern Hawaii (dashed-dotted gray line) (Klein, 1981), and Oahu (dashed gray line) (ten Brink and Brocher, 1987). V_P profiles are shown as a function of depth below sea level.

A notable feature of the velocity-depth profile beneath the Galápagos is that there are no evident changes in velocity gradient with depth between 3 and 10 km below sea level. A change in gradient from a shallow region having a rapid increase in velocity with depth to a deeper region having a low velocity gradient is recognizable elsewhere in oceanic crust formed at fast-spreading ridges (often termed the boundary between seismic layers 2 and 3), where it is attributed to a downward decrease in porosity and alteration

(e.g., Detrick et al., 1994). In addition, V_P (inferred from V_S) beneath the Galápagos at depths shallower than 13 km is lower than ~6.5 km/s (Fig. 3.15). In contrast, V_P in oceanic crust at fast-spreading ridges at depths greater than 4-6 km is almost constant and generally higher than ~7 km/s (Fig. 3.15a), characteristics attributed to a relatively homogenous layer of intrusive gabbros. We suggest that most of the crust beneath the Galápagos to depths as great as 10 km is comprised of a mixture of intrusive and extrusive rocks. For comparison, seismic reflection profiles show that the Hawaiian Islands could also be underlain by 6-7 km of extrusive rocks emplaced on top of the pre-existing oceanic crust (Watts et al., 1985; Watts and ten Brink, 1989). The extensive extrusive activity could reduce the decrease in porosity and alteration with depth seen elsewhere and may explain the apparent absence of a change in velocity gradient between 3 and 10 km depth.

There is a marked variation in crustal velocities within the archipelago. V_S beneath the western archipelago is up to 15% lower than beneath the eastern archipelago at 3-8 km depth, and up to 8% lower at 8-13 km depth (Fig. 3.13). This difference is consistent with results from surface wave tomography (Villagómez et al., 2007) that show lower-than-normal seismic velocities beneath the western archipelago extending to 40 km depth. The west-to-east increase in seismic velocities seems to be gradual (Fig. 3.9). This velocity increase correlates well with distance downstream from the hotspot and our observations give an increase of Rayleigh-wave group velocity of 0.05-0.06 km/s, or about 2.5-3% per million years, at 6-8 s period (for a velocity of the Nazca plate of 21 mm/yr at 0°N, 91°W (Gripp and Gordon, 2002), and an average Rayleigh-wave group velocity of 2.0 km/s).

We attribute the lower seismic velocities observed in the western crust to a combination of higher temperatures and higher amounts of melt at mid- to lower-crustal depths and to higher porosity within the extrusive rocks. We suggest that the western crust is warmer than the eastern crust, particularly at greater depths, because it lies above the inferred position of the Galápagos mantle plume (Toomey et al., 2002; Hooft et al., 2003; Villagómez et al., 2007). However, the difference in seismic velocity between the western and eastern crust is too large to be attributed solely to temperature. For instance, for $\partial \ln V_P / \partial T = -14 \times 10^{-5}$ K^{-1} (e.g., Dunn et al., 2000), a 15% difference in seismic velocity at 3-8 km depth would imply a 1070 K difference in temperature. At depths greater than 8 km, an 8% difference in seismic velocity would imply a 570 K difference in temperature.

Larger amounts of melt within the crust of the western archipelago can account for some of the observed velocity anomaly. The western archipelago is the location of the youngest and most active volcanoes in the region (McBirney and Williams, 1968; White et al., 1993). Also, the western volcanoes are likely underlain by long-lived magma chambers (Geist et al., 1998), and some of them may overlie a thick column of gabbroic mush that extends to the Moho (Geist et al., 2005). In contrast, the eastern volcanoes have experienced only a few Holocene eruptions, and petrologic evidence suggests that they do not have long-lived crustal magma chambers (Geist et al., 1998). If the melt-containing regions beneath the western volcanoes have horizontal extents comparable to those of the overlying calderas, only about 15-25% of the lengths of the paths between western seismic stations cross these melt regions. If solely attributed to melt beneath calderas, a 15% difference in seismic velocity at 3-8 km depth would imply a 60-100%

velocity reduction in the regions influenced by crustal melt. Alternatively, our results could be consistent with more modest amounts of partial melt if a larger horizontal extent of the lower crust is partially molten.

A complementary explanation for the lower velocities observed in the western archipelago is that they reflect increased porosity of the extrusive layers. Porosity is one of the most important factors controlling seismic velocity in the uppermost oceanic crust (e.g., Spudich and Orcutt, 1980; Shaw, 1994). Beneath the Galápagos, the east-west difference in velocity is larger in the upper parts of the crust (15% lower V_S at 3-8 km depth compared to 8% lower V_S at 8-13 km depth), where higher volumetric fractions of extrusive rocks are expected.

We attribute the west-to-east crustal velocity increase with age between 3 and 13 km depth to a combination of cooling of the crust after its passage above the Galápagos plume and a gradual decrease in porosity of extrusive rocks as a result of compaction, closing of cracks, and filling of open void spaces with hydrothermally deposited minerals (e.g., Grevemeyer and Weigel, 1997). A west-to-east decrease in the amount of melt present in the crust, inferred from the apparent absence of long-lived crustal magma chambers beneath the eastern volcanoes (Geist et al., 1998), is likely also to contribute to the eastward velocity increase, although this source of change may not be gradual. Geist et al. (1998) proposed two explanations for the systematic variation in the depth of magma chambers in the region: the depth is controlled by the rate at which magma is supplied from the mantle as the crust is carried away from the plume, or the depth is controlled by regional differences in lithospheric structure (e.g., Feighner and Richards, 1994). The former explanation would be expected to lead to a gradual variation in

characteristics influenced by crustal melt, whereas the latter explanation could yield either gradual or abrupt variations in crustal properties depending on the form of the lithospheric structure variations (see also section 4.2).

Farther downstream from the hotspot, beneath the western Carnegie Ridge, 250 km east of the Galápagos, the average crustal seismic V_P (Sallarés et al., 2005) is higher than that beneath the archipelago between 3 and 13 km depth (Fig. 3.15b). At 8 km depth, V_P beneath the western Carnegie Ridge is ~0.5 km/s higher than that inferred beneath the eastern archipelago (6.5 km/s and 6 km/s, respectively), equivalent to a V_P increase of 0.041 km/s or about 0.7% per million years during the last 12 million years (for a Nazca plate velocity of 21 mm/yr and 250 km distance). With $\partial \ln V_P / \partial T = -14 \times 10^{-5}$ K^{-1} (e.g., Dunn et al., 2000), the V_P increase represents a temperature decrease of ~50 K per million years if solely attributed to temperature. We suggest that this west-to-east velocity increase, like that observed within the archipelago, represents mostly a combination of cooling and a decrease in porosity. A pattern of crustal velocity increase with age is also observed at the Hawaii Islands between southern Hawaii and Oahu (Fig. 3.15b).

An additional result of this study is the north-to-south increase in seismic velocities in the eastern archipelago. V_S in the southeastern part of the archipelago is 5% higher than in the northeastern part between 3 and 8 km depth and 1% higher between 8 and 13 km depth (Fig. 3.15). We suggest that this crustal velocity increase at depths shallower than 8 km indicates cooling and closing of pore spaces with increasing crustal age and distance from the Galápagos Spreading Center.

3.4.2. Lithospheric Strength

A distinctive characteristic of the Galápagos platform is its large spatial variation in lithospheric strength. From gravity, geoid, and bathymetry data, Feighner and Richards (1994) determined that the western and southern parts of the archipelago are underlain by elastically competent lithosphere, but the flexural rigidity of the northeastern archipelago is at least one order of magnitude smaller. Feighner and Richards (1994) attributed this pattern to (1) reheating of the northeastern lithosphere by the plume, (2) an age offset of the lithosphere resulting from the 91.5°W Galápagos Fracture Zone (GFZ), and/or (3) differing elastic strength at the time of loading. Because elastic strength strongly correlates with the thermal state of the lithosphere (e.g., Watts and Zhong, 2000), our V_S results, which broadly constrain the spatial variations in the present thermal structure of the crust, can be used to test possible explanations.

The first explanation, that the elastic thickness in the eastern archipelago was reduced because of reheating by plume material advected eastward with plate motion requires the eastern lithosphere to be warmer, which is inconsistent with the results presented here. Moreover, results of surface wave tomography show no evidence of thermal erosion of the eastern lithosphere (Villagómez et al., 2007), so this alternative may be ruled out.

The second explanation suggests that the boundary separating elastically competent lithosphere in the west from Airy isostasy in the east (Fig. 3.16) corresponds to an age discontinuity created by the GFZ, and thus requires the GFZ to extend southward to at least 1°S. Although the southern extent of the GFZ is not known

precisely, analysis of magnetic anomalies (Wilson and Hey, 1995; D. S. Wilson, pers. comm., 2007) and plate motion reconstructions (Meschede and Barckhausen, 2000) suggest that the GFZ may have initiated less than 2.6-3.6 My ago, and that its southward termination is likely to the north of 0°S (for a half-spreading rate of 25–30 km/My) (Fig. 3.17). Moreover, our results suggest that that the crustal seismic velocity increase observed from west to east is gradual, so it is unlikely to reflect a thermal structure arising from an age offset across a fracture zone. In agreement with plate reconstructions (Fig. 3.17), we suggest that there is no major east-to-west lithospheric age discontinuity beneath the Galápagos platform and thus we may also rule out this explanation.

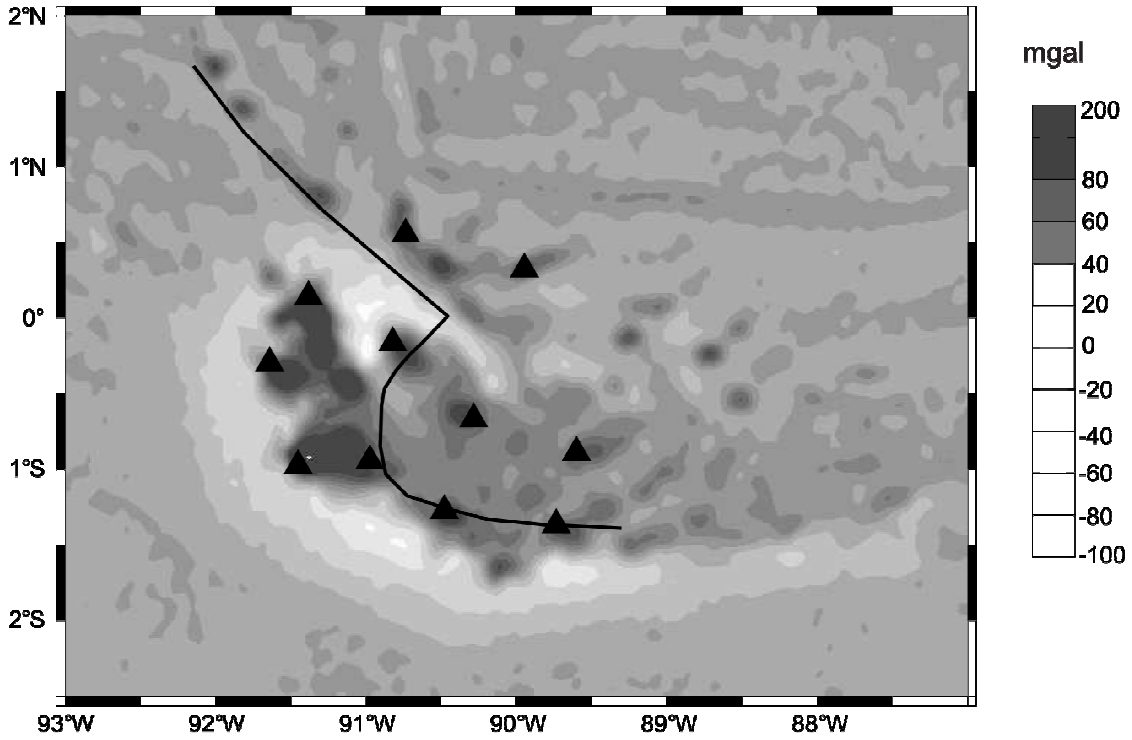

Fig. 3.16. Free-air gravity anomaly in the Galápagos region (Sandwell and Smith, 1997). Triangles indicate seismic stations, and the black line shows the locus of the transition from elastically competent lithosphere in the south and west to Airy compensation in the central platform suggested by Feighner and Richards (1994).

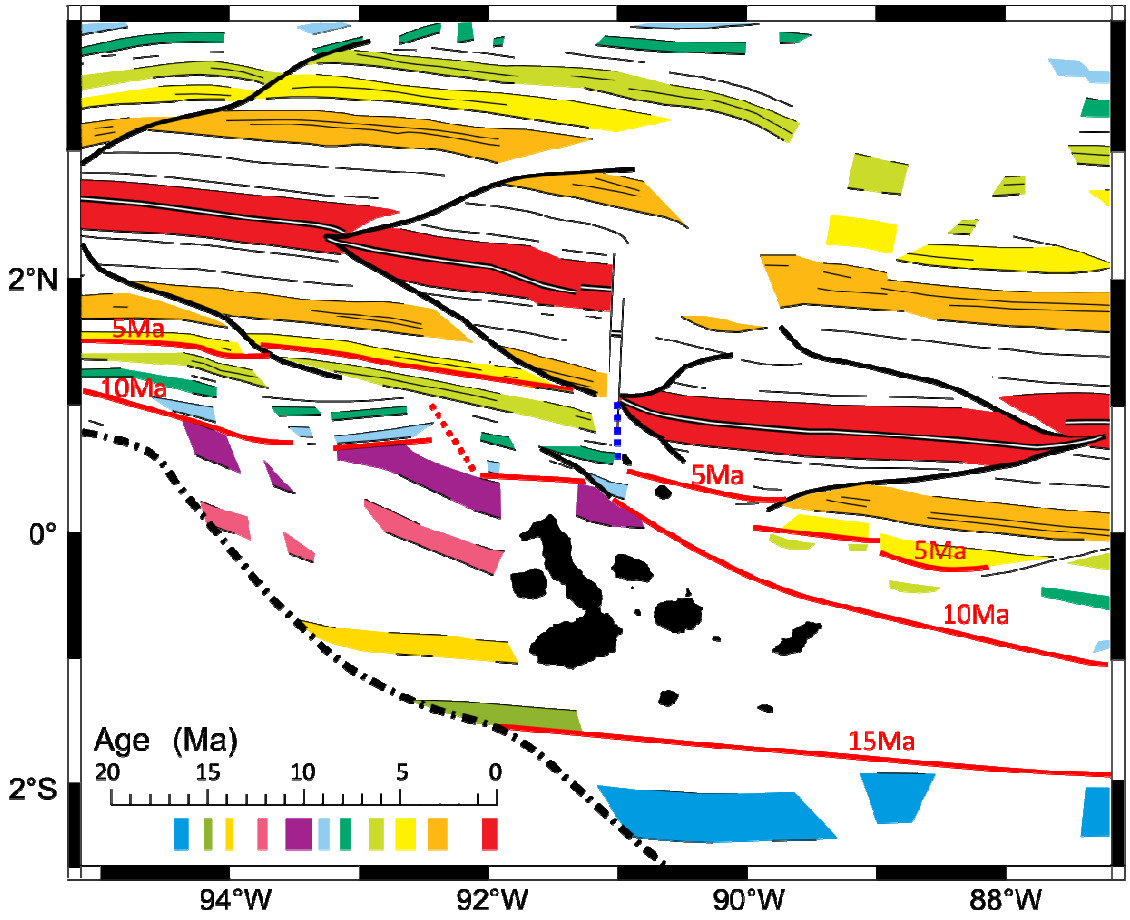

Fig. 3.17. Isochron map. Color contours and thin black lines are inferred from magnetic anomalies (Wilson and Hey, 1995; Barckhausen et al., 2001; D. S. Wilson, pers. comm., 2007). Thick black lines show propagator pseudo-faults (Wilson and Hey, 1995). The dashed-dotted black line shows the boundary that separates seafloor created at the Galápagos Spreading Center from that formed at the East Pacific Rise (Barckhausen et al., 2001). Red lines with approximate ages are our interpretation of isochrones from a reconciliation of the magnetic anomalies with paleogeographic reconstructions (Meschede and Barckhausen, 2001). The blue dashed line shows our interpretation of the extent of the Galápagos Fracture Zone (GFZ).

The most plausible explanation for the differences in lithospheric strength across the Galápagos platform is that the eastern archipelago was closer to the ridge and the lithosphere was weaker at the time of loading. Models for the deformation of an elastic

plate indicate that the flexural rigidity of the lithosphere depends on the thermal age of the lithosphere at the time of loading (Watts and Zhong, 2000; Turcotte and Schubert, 2002, pp. 331-339). In support of this interpretation, the gravity anomaly map in Fig. 3.16 shows that the flexural response to loading is present throughout the archipelago, and that this signal is strongest where the age of the lithosphere at the time of loading is oldest. The eastern lithosphere was very young and weak at the time of loading, so its flexural response is less pronounced. In contrast with the specific scenario of Feighner and Richards (1994), however, we suggest that the present spatial differences in the strength of the elastic lithospheric may be gradual rather than abrupt.

3.4.3. Plume-lithosphere Interactions

As noted earlier, the Galápagos hotspot resembles other oceanic intraplate hotspots in many respects, including its long lifetime, the chemistry of its basalts, its distinctive hotspot trails on two plates, the age progression of associated seamounts, and low seismic velocities in the underlying upper mantle. However, the Galápagos hotspot differs from other hotspots in its broad area of recent volcanic activity, approximately 300x200 km^2, and in the east-west differences in lava compositions and volcano morphology, differences thought to be related to volcano location at the time of formation (Harpp and Geist, 1998). We synthesize our results with earlier work to further elucidate the role of both the mechanical and the chemical lithospheres in controlling spatial variations in magma composition and the alignment of volcanic centers.

A possible explanation for the spatial variability in lava composition is that it reflects unusual dynamics and interaction of the mantle plume with depleted upper mantle (Geist et al., 1988; Richards and Griffiths, 1999; White et al., 1993). By this idea, the current location of the Galápagos plume beneath the western archipelago accounts for the more enriched geochemical signatures of the western volcanoes, whereas mixing of plume material with depleted upper mantle leads to the depleted signatures of the eastern volcanoes. Geist et al. (1988), Richards and Griffiths (1988), and White et al. (1993) proposed that such mixing could be caused by thermal entrainment of depleted mantle into the plume as the upwelling material is sheared eastward by plate drag. Body-wave and surface-wave tomography (Toomey et al., 2002; Villagómez et al., 2007), however, show no evidence of bending of the plume by plate drag, posing a difficulty for this model at the Galápagos hotspot. In addition, this model predicts that lavas at individual eastern volcanoes should show temporal trends from enriched to more depleted geochemical signatures. However, detailed studies have not revealed age trends in lava composition within single volcanoes (Geist et al., 1998), with the possible exception of Floreana Island in the southern part of the archipelago (Lyons et al., 2007).

A second possibility is that the spatial variability in lava composition is caused by compositional zoning of the plume (Hoernle et al., 2000; Farnetani et al., 2002; Werner et al., 2003). Hoernle at al. (2000) showed that the variability in lava composition occurs at the same relative positions along a geochemical profile across the Galápagos hotspot track off the coast of Costa Rica, suggesting that the spatial zonation of the Galápagos hotspot may be a signature of the source that could have persisted for at least 14 My.

We recently proposed, as an alternative explanation, that variations in the thickness of the thermal and chemical lithosphere contribute to variations in lava composition (Villagómez et al., 2007). Surface wave tomography has revealed a mantle lid of high seismic velocity and variable thickness beneath the Galápagos region. This lid is interpreted to be higher in viscosity than the underlying convecting mantle because of dehydration by removal of partial melt (Villagómez et al., 2007). The lid is 60-70 km thick beneath the western and southern part of the archipelago and ~40 km thick beneath the northeastern part (Fig. 3.18). We suggest that the lid to the northeast corresponds to the thermal lithosphere, whereas the bottom of the lid beneath the western and southern parts of the archipelago corresponds to a chemical boundary identified as the base of the residuum from melt removal (see Fig. 16 of Villagómez et al. (2007)). Variations in the thickness of the chemical lithosphere are probably affected by temporal changes in plume-ridge separation and the interaction between the plume and ridge melting zones. The thickness of the seismic velocity lid correlates well with geochemical anomalies (Fig. 3.18). In this scenario, spatial variations in isotopic signatures are due to differences in the amount of melting as a function of depth: enriched lavas to the west and south are consistent with a greater proportion of melting occurring at relatively greater depths, whereas more depleted geochemical signatures result from more extensive partial melting at shallower depths.

Another distinctive characteristic of the Galápagos is that several volcanic centers and seamounts are aligned mostly along northeast- and northwest-trending lineations (Fig. 1.1), known as the Darwinian lineaments. Darwin (1860) first noted that the islands exhibit aligned fractures, and McBirney and Williams (1969) showed that the volcanoes

themselves are aligned along rectilinear trends. One of the most prominent lineaments is the Wolf-Darwin lineament (WDL) located to the north of the archipelago (Fig. 1.1). Although the origin of these trends is not well known, recent studies suggest that the lineations are controlled by patterns of stress in the lithosphere (Harpp and Geist, 2002; Sinton et al., 2003; Mittelstaedt and Ito, 2005). For instance, Harpp and Geist (2002) suggested that the WDL is the result of extensional stresses emanating from the inside corner of the transform fault at 91°W. Sinton et al. (2003) and Mittelstaedt and Ito (2005) suggested that some of the lineations to the north of the archipelago, which appear to radiate from a point near 0° N, 90.7°W (e.g., Fig. 9 of Sinton et al. (2003)), are caused by gravitational stresses resulting from lithospheric uplift by an impinging plume or by the combined effects of the plume and the segmented ridge. However, these explanations do not account for many of the other lineations observed in the western and southern archipelago that do not show a radial pattern, such as the lineations on the J-shaped Isabela Island (Fig. 1.1).

We propose that the northwest- and northeast-trending Darwinian lineaments that are found throughout the archipelago may be associated with pre-existing weaknesses in lithospheric structure that are reactivated by plume-lithosphere interactions. Fig. 3.17 displays a combination of magnetic anomalies (Wilson and Hey, 1995; Barckhausen et al., 2001; D. S. Wilson, pers. comm., 2007) and plate reconstructions (Meschede and Barckhausen, 2001). These results show that the Galápagos Spreading Center has undergone a complicated series of ridge jumps and ridge propagation events. Of particular interest is that episodes of ridge propagation result in either V-shaped pseudo-

faults, where magnetic anomalies are offset, or V-shaped swaths of anomalous crust and lithosphere formed at overlapping spreading centers (OSCs).

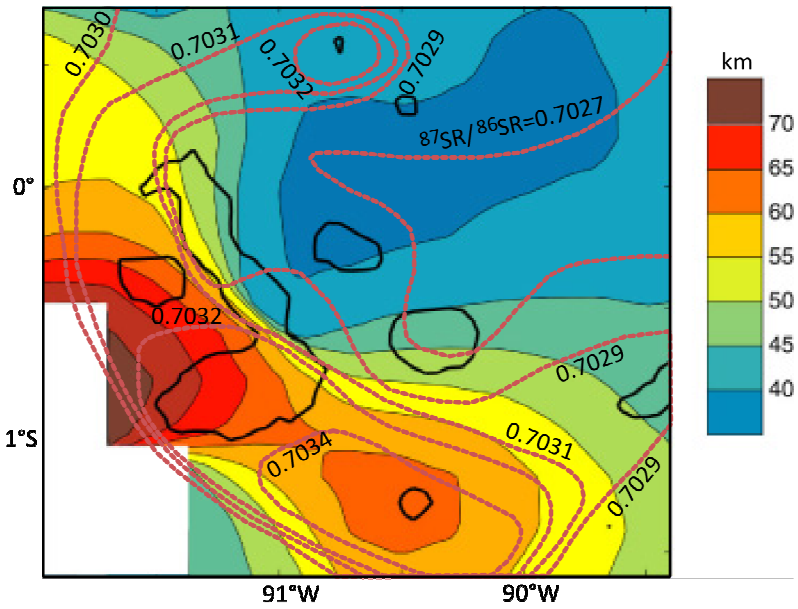

Fig. 3.18. Comparison of estimates of the thickness of the lid of high mantle seismic velocities (color contours) (Villagómez et al., 2007) with the geographic variation in the $^{87}Sr/^{86}Sr$ ratio of sampled basalts (dashed red lines) (Harpp and White, 2001).

Beneath the Galápagos Archipelago the trends of the pseudo-faults or OSC wakes would be in the northwestern and northeastern directions. Pseudo-faults associated with ridge propagation events and wakes of OSCs are likely zones of weakness in the oceanic lithosphere on which the Galápagos Archipelago is constructed. Studies of propagators and OSCs along fast- and intermediate-spreading ridges indicate that they are tectonically complex and capable of generating discordant zones several tens of kilometers across that

are characterized by extensive faulting, block rotation, and crustal alteration (Carbotte and Macdonald, 1992; Canales et al., 2003). Images of crustal-scale normal faults and the distribution of earthquakes within the Juan de Fuca plate system further indicate that propagator wake areas are likely to be more faulted and therefore more hydrated than other parts of the plate system (Nedimović et al., 2009). We thus infer that most of the northeast- and northwest-trending Darwinian lineaments may owe their origin to pseudo-faults or wakes of OSCs formed during earlier episodes of ridge propagation. By this view, stresses generated by plume-lithosphere interactions reactivated these zones of lithospheric weakness.

CHAPTER IV

UPPER MANTLE JOINT INVERSION OF BODY AND SURFACE WAVES

4.1. Introduction

A previous surface wave tomographic study of the uppermost mantle beneath the Galápagos Archipelago (Villagómez et al, 2007) detected a high velocity lid with variable thickness that correlates well with regional variations in lava geochemistry (Geist et al., 1988; White et al., 1993): The lid is thickest (70-100 km thick) beneath the southwestern part of the archipelago where the more enriched geochemical signatures are found, while it is thinner (40-60 km thick) beneath the center and eastern parts of the archipelago where the lavas tend to have a more depleted composition. This suggests that the lid may be an important regional feature controlling mantle melting and upwelling.

Villagómez et al. (2007) suggested that the high velocity lid represents residuum from melting. The depletion and dehydration caused by melt extraction can increase seismic velocity and viscosity of the mantle and form a lid that could slow plume upwelling. However, the resolution of surface waves is limited below 100-150 km depth, and thus provides poor constraints on the pattern of upwelling below 150 km depth and the interaction of the plume with the high velocity lid.

Here we present results of joint inversions of body and surface waves. By combining phase velocity measurements with body wave delay times we are able to

achieve good resolution of seismic structure as deep as ~300 km. The joint inversion successfully images velocity anomalies beneath the high velocity lid that can be used to infer patterns of mantle upwelling. The inversions also detect three distinct melting regions at different depths and geographic locations that can be used to refine models of upwelling and melting of the Galápagos mantle plume.

4.2. Tomographic Method

We present a tomographic method that allows for the simultaneous inversion of body wave delay times and Rayleigh wave phase velocities to solve for three-dimensional (3-D) isotropic P and S wave velocities. The method includes variable weighting of body and surface wave data and coupling of P and S wave structures. We follow the approach described in Toomey et al. (1994) and Hammond and Toomey (2003) to solve for isotropic P and S wave slowness perturbations, and expand the method with the addition of surface waves observations.

The inverse problem is ill-conditioned, and thus we stabilize the inversion by applying additional constraints. We add conditions of minimum model norm, spatial smoothing, and a constraint on the relative P and S velocity perturbations. For a given starting model, the method determines the perturbations that minimize the weighted sum of data norm, model norm and model roughness. We use a hypothesis testing approach that introduces a starting slowness model a priori (Jackson, 1979; Tarantola and Valette, 1982).

4.2.1. Forward Problem

The forward problem for body waves consists of the determination of the ray geometry and travel time for each event source and seismic station. We follow the implementation described in Toomey et al. (1994) to calculate ray paths and travel times through three-dimensional models. We define a model grid of nodes beneath the seismic array (that we term the model grid) with assigned P and S slowness (u_P and u_S) values at each nodal point. The ray geometry is a function of the slowness model and ray paths are calculated with the graph theory using the shortest-path algorithm of Dijkstra (1959) and Moser (1991). An important feature of this method is that given a slowness model it provides the shortest path from a starting position to all the nodes within the grid, and thus this calculation needs to be performed only once for each seismic station.

For a particular telesismic ray path, because the model grid is defined only locally beneath the seismic array, most of ray path is located outside the grid. To determine the geometry of the ray inside the model grid first we need to estimate the location where the teleseismic ray path enters the model grid. To do so, we estimate the travel time from the source of the event to each node at the bottom of the model grid using IASP91 (Kennet and Engdahl, 1991). To find the particular node of entry of the seismic ray, we add these travel times outside the grid to the corresponding travel times obtained by the shortest-path method inside the grid and find the node with the minimum combined travel time. By Fermat's principle, the path with the least time corresponds to the seismic ray path.

We calculate teleseismic delay times Δt from a perturbational slowness model Δu according to

$$\Delta t = \int_{path} \Delta u \; ds \tag{4.1}$$

where the integral is evaluated along the ray path and ds is the incremental path length. This perturbational slowness model Δu will be obtained during the inversion procedure and is defined as a grid of nodes, which we term the perturbational grid. The perturbational grid may or may not have the same density of nodes and node locations as the model grid. In some cases it is advisable to parameterize the model grid at a higher nodal density to more accurately describe the ray path geometries, but to keep the perturbation grid at a lower node density to reduce the number of inversion parameters and thus the computational time when performing the tomography.

The forward problem for surface waves consists of computing the Rayleigh wave phase velocity c(ω) at particular frequencies ω for a given one-dimensional (1-D) P and S slowness model. For each set of vertical nodes in the perturbational grid we estimate the Rayleigh wave phase velocity dispersion curve using DISPER80 (Saito, 1988), which calculates normal modes for a laterally homogeneous model.

4.2.2 Inverse Problem

We solve the non-linear tomographic inverse problem

$$\begin{bmatrix} C_{d\Delta t}^{-1/2} G \\ \lambda_C C_{d\Delta c}^{-1/2} A \end{bmatrix} \begin{bmatrix} \Delta u_P \\ \Delta u_S \end{bmatrix} = \begin{bmatrix} C_{d\Delta t}^{-1/2} \Delta t \\ \lambda_C C_{d\Delta c}^{-1/2} \Delta c \end{bmatrix} \tag{4.2}$$

for changes Δu to the slowness model, where Δt is the $n_d x1$ vector of body wave delay data, Δc is an $n_c x1$ vector containing the observed phase velocity anomalies and n_c is equal to the number of nodes on the horizontal plane for which there are phase velocity observations multiplied by the number of frequencies. $C_{d\Delta t}$ and $C_{d\Delta c}$ are the data covariance which are diagonal matrices of variances (the observations are assumed to be independent) estimated for the body wave delay times and phase velocities respectively. Δu_P and Δu_S are vectors of perturbation to model parameters. G is the Frechet matrix of partial derivatives of delay times with respect to model perturbations $\partial t_i/\partial u_j$ ($i=1,n_d$). A is the matrix of partial derivatives of phase velocity perturbations with respect to model perturbations $\partial c_k/\partial u_j$ ($k=1,n_c$). λ_C is a weight parameter that controls the amount of influence of the phase velocity data in the inversion and accounts for the difference in the number of delay times and phase velocity observations. The problem is nonlinear because the partial derivatives matrices G and A are themselves functions of the model parameters Δu. The solution requires an iterative process where the partial derivatives are calculated at each iteration until the inversion converges to a solution. We use LSQR (Paige and Saunders, 1982) to solve equation 4.2.

The relationship between travel time delays and the individual parametric nodal values defining the perturbational model can be calculated using (Toomey et al., 1994)

$$\frac{\partial t_i}{\partial u_j} = \int_{path} w_j \, ds \tag{4.3}$$

where w_j are linear interpolation weights, the integral is along the ray path and ds is the incremental path length. The weights are evaluated locally using only those parametric

nodes that are immediately adjacent to the particular node in the perturbational grid (Toomey et al., 1994). Thus the partial derivative of a travel time with respect to the slowness u_j is the length of the path influenced by the parameter, weighted by the linear interpolation coefficients.

Partial derivatives of phase velocity perturbations with respect to changes in slowness are computed using DISPER80, which solves the forward problem of estimating phase velocities c(ω) for a given slowness model. First, phase velocities are calculated at the frequencies of interest ω using the given slowness model, and then the slowness is increased by a small amount (1%) and phase velocities are calculated again. The partial derivatives $\partial c_k/\partial u_j$ are estimated by taking the difference between the phase velocities divided by the difference between the slowness values. Using this method, the partial derivatives can be estimated separately for P-wave slowness, S-wave slowness or density changes. However, changes in phase velocities of Rayleigh waves are mostly sensitive to changes in S-wave slowness, and thus we ignore sensitivity with respect to changes in P-wave slowness and density.

We introduce 2 different types of correction parameters to the inversion. First, to reduce the effect of shallow structure beneath individual stations that may produce systematic shifts in the measured delay times we add station correction parameters γ_S. At each iteration we solve for both P- and S-wave station terms.

Second, to reduce the influence of seismic structure outside of the model region that may have affected the body wave measurements, we allow for shifts to the event location and origin time. We use 2 different relocation corrections to the travel time: (a)

One correction γ_E for the location of every event. At each iteration, we solve for the best fitting changes in delta or distance to the epicenter (ΔD) and changes in the depth of the event (ΔZ). Partial derivatives of travel times with respect to D, $Y_D=\partial t_i/\partial D$ (ray parameter), and of travel times with respect to Z, $Y_Z=\partial t_i/\partial Z$, are computed numerically using IASP91 (Kennet and Engdahl, 1991). At the end of the iteration we compute $\gamma_E = (\partial t_i/\partial D)\,\Delta D + (\partial t_i/\partial Z)\,\Delta Z$. And (b) one static correction γ_T for every phase of each event. Partial derivatives of travel times with respect to γ_T, $Y_T=\partial t_i/\partial \gamma_T = \text{sign}(\partial t_i/\partial D)$. At each iteration we solve for the best fitting $\Delta\gamma_T$. After applying the corrections, the total residual delay time (r) is computed using

$$r = \Delta t - \Delta t_P - \gamma_S - \gamma_E - \gamma_T \qquad (4.4).$$

where Δt is the observed delay time and Δt_P is the predicted delay time using the perturbational slowness model. We estimate the RMS misfit of the inversion due to delay times (R) using

$$R=\sqrt{\frac{\bar{r}^{T} C_{d\Delta t} \bar{r}}{n_d}} \qquad (4.5)$$

where $\bar{r}$ is a n_dx1 vector containing all the residual delay times r.

To stabilize the inversion, we add additional constraints of minimum model norm, spatial smoothing and a constraint on the relative P and S slowness perturbations. The augmentation of equation (2) with the correction parameters and the additional constraints results in

$$\begin{bmatrix} C_{d\Delta t}^{-1/2} G \\ \lambda_C C_{d\Delta c}^{-1/2} A \\ C_{d\Delta t}^{-1/2} Y_S \\ C_{d\Delta t}^{-1/2} Y_D \\ C_{d\Delta t}^{-1/2} Y_Z \\ C_{d\Delta t}^{-1/2} Y_T \\ C_D \\ \lambda_H C_S \\ \lambda_{PS} C_{PS} \end{bmatrix} \begin{bmatrix} \Delta u_P \\ \Delta u_S \\ \Delta \gamma_S \\ \Delta D \\ \Delta Z \\ \Delta \gamma_T \end{bmatrix} = \begin{bmatrix} C_{d\Delta t}^{-1/2} \Delta t \\ \lambda_C C_{d\Delta c}^{-1/2} \Delta c \\ 0 \\ 0 \\ 0 \\ 0 \\ 0 \\ 0 \end{bmatrix} \quad (4.6),$$

where G, A, Y_S, Y_D, Y_Z and Y_T are the partial derivatives discussed above; Δu_P, Δu_S, $\Delta\gamma_S$, ΔD, ΔZ and $\Delta\gamma_T$ are changes to the model parameters: P-wave slowness, S-wave slowness, and corrections for station terms, event delta, event depth and time of event-phase combinations respectively; Δt and Δc are the body wave delay time and phase velocity anomalies respectively, and $C_{d\Delta t}$ and $C_{d\Delta c}$ are the data covariance matrices. The matrices C_D, C_S, C_{PS} and the weights λ_H and λ_{PS}, add the damping constraint, model smoothness and coupling of P and S relative slowness perturbations.

Minimization of the model norm is achieved using a damping constraint where C_D is a diagonal matrix whose elements are

$$C_{D\ ii} = \begin{bmatrix} \lambda_P / \left(\sigma_{u_p} u_{p_o}\right) \\ \lambda_S / \left(\sigma_{u_S} u_{S_o}\right) \\ \lambda_{ST} / \sigma_{\gamma_S} \\ \lambda_R / \sigma_D \\ \lambda_R / \sigma_Z \\ \lambda_R / \sigma_{\gamma_T} \end{bmatrix} \quad (4.7),$$

where the vectors σ correspond to the a priori evaluation of model parameter uncertainty, and the parameters λ_P, λ_S, λ_{ST} and λ_R specify the relative importance of the damping

constraints for P-wave slowness, S-wave slowness, station corrections and event relocation respectively. Equation 4.6 is in a simplified notation and all the vector operations and $1/\sigma$ are performed element by element. The matrix C_D has a size of mxm, where m is the total number of model parameters. The damping constraints for slowness perturbations are normalized by the initial slowness u_{Po} and u_{So} so that the perturbations are applied uniformly in terms of percent change. If left unnormalized, the damping constraint will preferentially attempt to distribute slowness perturbations in absolute terms evenly throughout the model (Wiggins, 1972), causing increased levels of heterogeneity towards the bottom of the model where seismic velocity is highest (slowness is smallest) (e.g., Toomey et al., 1994).

The matrix of smoothing constraints C_S averages perturbations with those at adjacent nodes. We compute the matrix using the approach described in Toomey et al. (1994). To control the trade-off between model variance (roughness) and model resolution, we use the weight parameter λ_S, which adjusts the amount of spatial smoothing. In practice, we use separate constraints for the horizontal and vertical directions to allow for increased control of the final smoothness of the model.

We introduce a constraint between the perturbations in P and S wave slowness that couples the perturbations and enforces the notion that the P and S wave structures may not be independent. We try 2 forms of P-S coupling: (1) the ratio of P to S velocity, V_P/V_S, is assumed to be spatially smooth and (2) the value of $\partial \ln V_P / \partial \ln V_S$ is constant throughout the model. We follow the approach and equations described in Hammond and Toomey (2003).

To implement the first constraint, we spatially average the function:

$$\delta\left(\frac{V_P}{V_S}\right)_i = \sum_{j\neq i} w_j \delta\left(\frac{V_P}{V_S}\right)_j \qquad (4.8),$$

where w_j are linear interpolation weights described in Toomey et al. (1994). In addition, we use the following approximation.

$$\delta\left(\frac{V_P}{V_S}\right) = \frac{V_S \delta V_P - V_P \delta V_S}{V_S^{\,2}} \qquad (4.9).$$

To implement the second constraint we apply the approximation

$$\frac{\partial \ln V_S}{\partial \ln V_P} \approx \frac{V_P}{V_S}\frac{\Delta V_S}{\Delta V_P} \approx \frac{V_P}{V_S}\frac{\Delta u_S}{\Delta u_P} \qquad (4.10).$$

The relative strength of the coupling constraint is specified by the parameter λ_{PS}.

4.3. Synthetic Inversions of S-wave Slowness Perturbations

We performed series of synthetic inversions to validate out methods and to assess the resolution of the surface and body wave observations. To perform a synthetic inversion we first create a 3-D synthetic model of slowness perturbations and we obtain estimates of predicted delay times and phase velocity anomalies with added random noise. We then perform the inversion using the synthetic data and compare the resulting model with the original synthetic model.

Fig.4.1 shows the results for 2 different synthetic models A and B, in S-N cross-sections at a longitude of 91°W. For each synthetic model, we tested three scenarios: surface wave data only, body wave delay times only, and joint inversion of surface and body waves. Figs. 4.1b-d show the results of the inversions for the 3 scenarios corresponding to synthetic model A shown in Fig. 4.1a, while Figs. 4.1f-h show the results of the inversions corresponding to synthetic model B shown in Fig. 4.1e.

The results of the inversion that use only surface waves (Fig. 4.1b and 4.1e) show that the resolution of surface waves decreases rapidly with depth. Surface waves can resolve seismic structure relatively well at depths less than 100 km, but resolution is limited between 100 and 200 km depth. Surface waves cannot resolve seismic structure below 200 km depth. On the other hand, body wave data shows relatively good resolution between ~100 and ~300 km depth (Fig. 4.1c and 4.1f), but resolution is poor in the shallower and deeper parts of the model where there are not enough crossing seismic rays.

Results of a joint tomography show that at the depths between 100 and 200 km, the resolution of body and surface waves are complementary. Through the combination of surface and body waves we are able to reliably recover seismic structure above ~300 km depth.

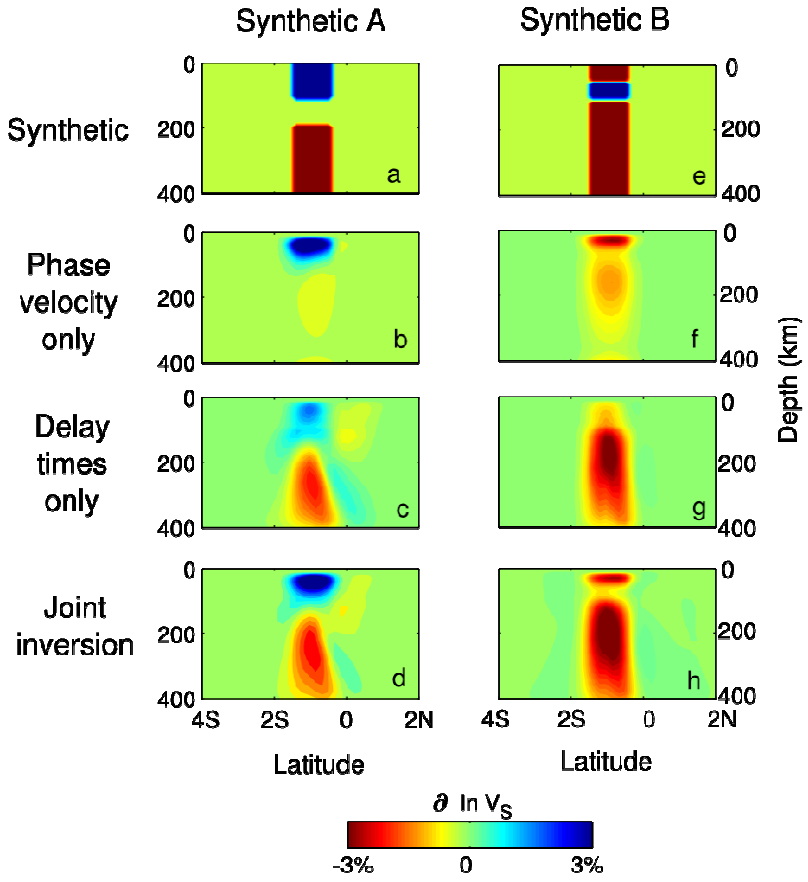

Fig. 4.1.Synthetic inversion for S-wave slowness perturbation. Color scale represent calculated shear-wave velocity perturbations. Panels are S-N cross-sections at 91°W of longitude. (a-d) Synthetic model A. (e-h) Synthetic model B. (a and d) Synthetic perturbation model. (b and f) Results of inversions using only phase velocity data. (c and g) Results of inversions using only body wave delay times. (d and h) Results of joint inversions of phase velocities and body waves delay times.

4.4. Results

4.4.1. Body Wave Delay Time Measurement

We measured 1000 S-wave and 1783 P-wave relative delay times from 11 seismic stations and 110 teleseismic events (m_b>5.5) that occurred between 1999 and 2003. P-

wave delay times were identified in the vertical seismometer channel, while S-wave delay times were estimated using horizontal channels, in radial or transverse directions with respect to the station-to-event azimuth. Prior to measuring delay times, waveforms were corrected for instrument response and filtered in varying period bands using a order 3 Butterworth filter forward and backward to provide a zero phase response. We measured relative delay times with respect to the IASP91 one-dimensional seismic Earth model (Kennet and Engdahl, 1991), using cross correlation of up to three cycles of the waveform (VanDecar and Crosson, 1990).

Fig. 4.2 shows the coverage of seismic rays for the S-wave delay time measurements beneath the seismic network. During the inversion, the delay times can help resolve seismic structure in parts of the model grid with a higher density of crossing seismic rays.

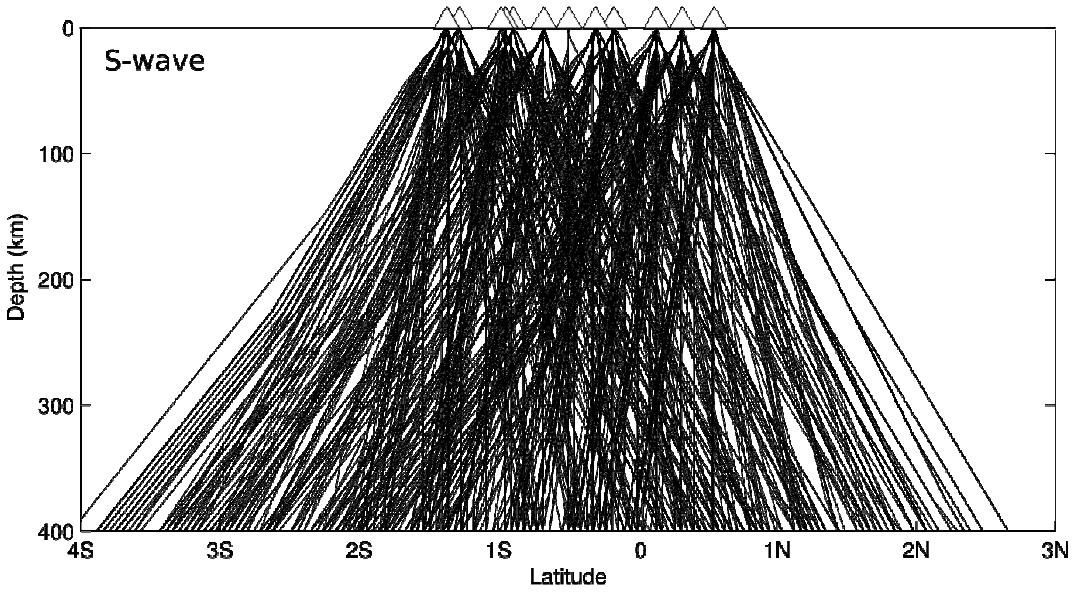

Fig. 4.2. S-wave seismic rays in W-E projection.

Histograms of the distributions of the effective P-wave and S-wave delay times are shown in Fig. 4.3. To reduce the effect of systematic timing errors or shallow seismic structure beneath particular stations on the delay times, the relative delays are adjusted by subtracting the inferred station time delay correction from the measured delay times. When comparing the average size of the delay times (by taking the absolute value), the average S-wave delay time (0.48 s) is 2.4 times bigger than the average P-wave delay time (0.20 s).

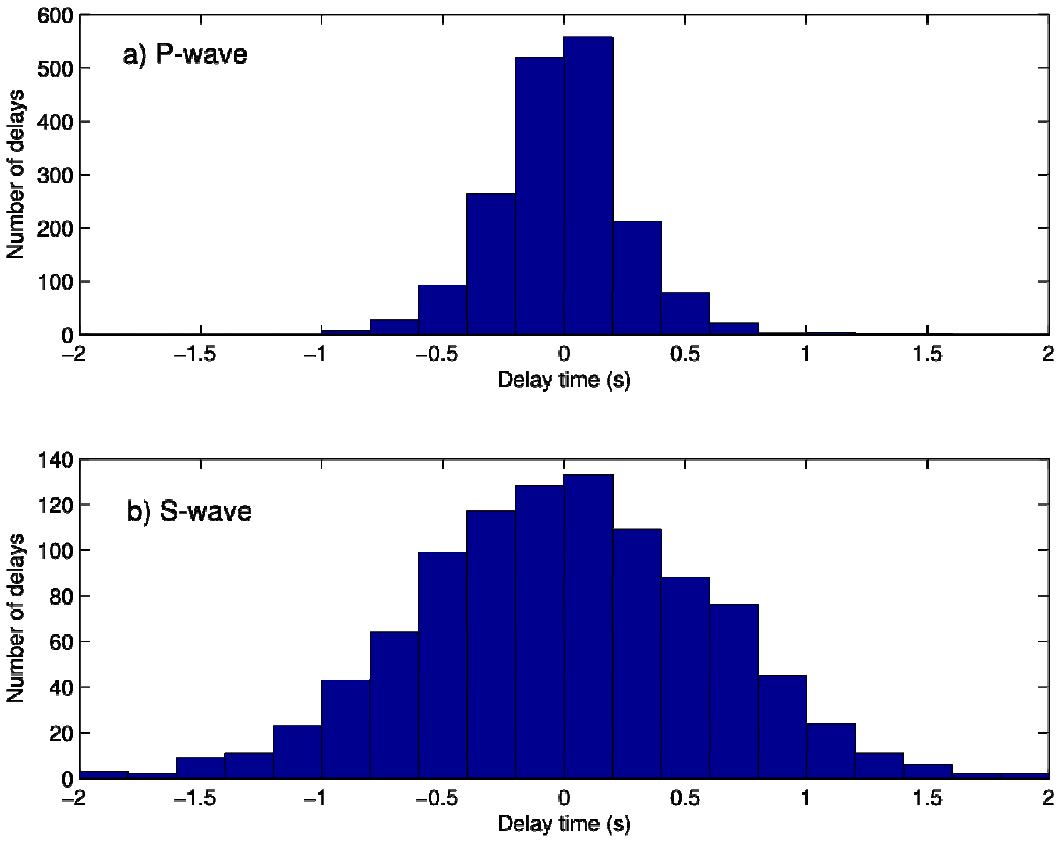

Fig. 4.3. Distribution of relative delay times (in seconds) for a) P-waves and b) S-waves.

Fig.4.4 shows the size of the corrected delay time observed for each seismic ray, plotted at the point where the ray intersects the bottom of the model grid at 400 km depth. Red circles represent a positive relative delay time (late arrival), blue circles represent a negative delay time (early arrival), and the size of the circle is proportional to the size of the delay. This visualization of the distribution of the piercing points of the rays at the bottom of the model grid is useful for interpreting the results of the inversions and the resolution of the tomography. For instance, delay times tend to be positive towards the western part of the archipelago, between 90°W and 92°W, while they tend to be late toward to the west of 92°W and north of ~1°N.

4.4.2. Phase Velocity Measurement and Inversion for Absolute V_S

We used 2-D Rayleigh-wave isotropic phase velocity maps for the Galápagos from Villagómez et al. (2007). The maps were obtained at periods between 20 s to 125 s (frequency between 0.008 Hz and 0.05 Hz) from the inversion of measurements of phase and amplitude of Rayleigh waves. Villagómez et al. (2007) used a two-plane wave approximation technique (Forsyth and Li, 2005), in which the incoming wavefield at each frequency (ω) is represented as the sum of two incoming plane waves with different azimuths, amplitudes and phases. This representation can account for wave-propagation effects outside of the seismic network such as multipathing, and can provide up to 30-40% variance reduction when compared to the standard one-plane wave method (e.g., Li et al., 2003).

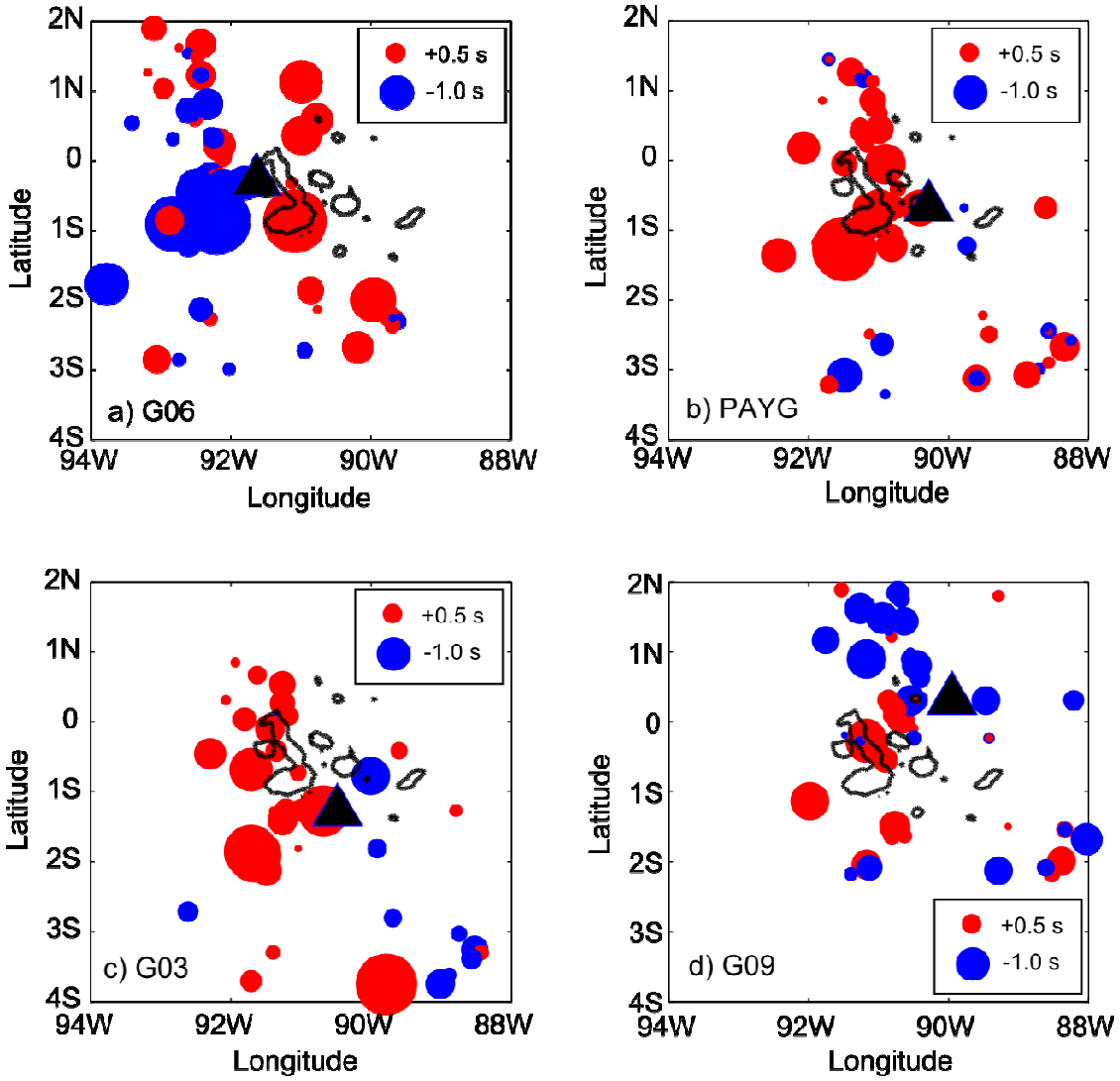

Fig. 4.4. Distribution of piercing points of S-wave seismic rays at bottom of model grid (400 km depth) for (a) G06, (b) PAYG, (c) G03 and (d) G09. Black triangles show reference seismic stations. Blue circles represent early arrivals (negative delay times) and red circles represent late arrival (positive delay times). Size of circle is proportional to the size of the delay. Delay times have been corrected by adding station corrections.

Because of their finite frequency, surface waves are sensitive to seismic structure near the propagation path. To account for these effects, two-dimensional sensitivity kernels for fundamental Rayleigh waves were calculated by means of a single-scattering

(Born) approximation (Zhou et al., 2004; Yang and Forsyth, 2006). For each frequency, the amplitude and phase kernels were incorporated into the phase velocity inversion. The frequency-dependent measurements of phase and amplitude of Rayleigh weaves were inverted for 1-D and 2-D phase velocity structures separately for each frequency. 2-D phase velocity anomalies (Δc) are obtained by subtracting the 1-D phase velocities (regional average) from the 2-D phase velocities. Fig. 4.5 shows 2D maps of Δc for 20 s, 40 s and 80 s periods.

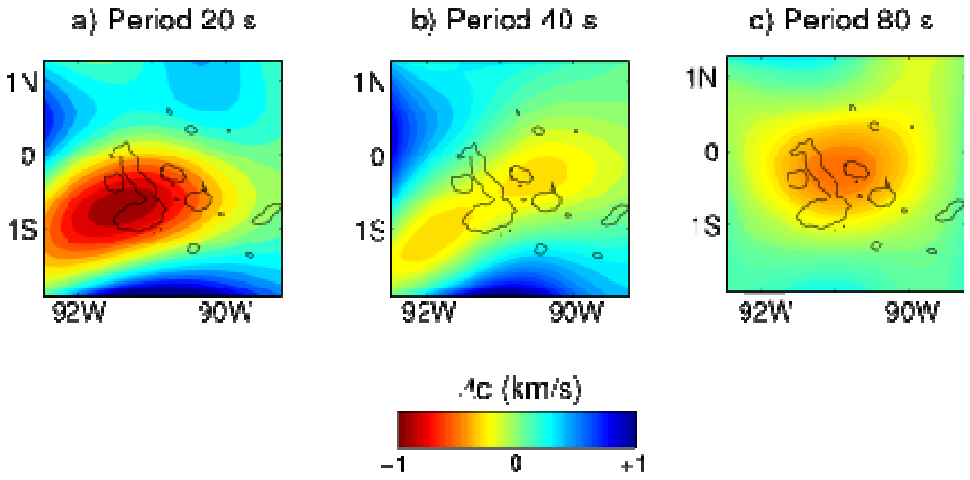

Fig. 4.5. Two-dimensional (2-D) maps of Δc for a) 20 s, b) 40 s and c) 80 s period.

Phase velocity measured at a range of periods can constrain the absolute value of V_S as a function of depth. Villagómez et al. (2007) inverted the 1-D and 2-D phase velocity measurements to obtain a 1-D and a 3-D V_S model between 20 and 150 km depth. Fig. 4.6a shows the regional phase velocities (1-D) as a function of period (T). Fig.

4.6b shows the sensitivity kernels ($\partial c/\partial V_S$) for selected periods between 0 and 400 km depth. The peak sensitivity of Rayleigh waves phase velocity occurs at 4/3T km depth. For this range of periods, 20-125 s, the waves are mostly sensitive to V_S structure shallower than ~150 km depth.

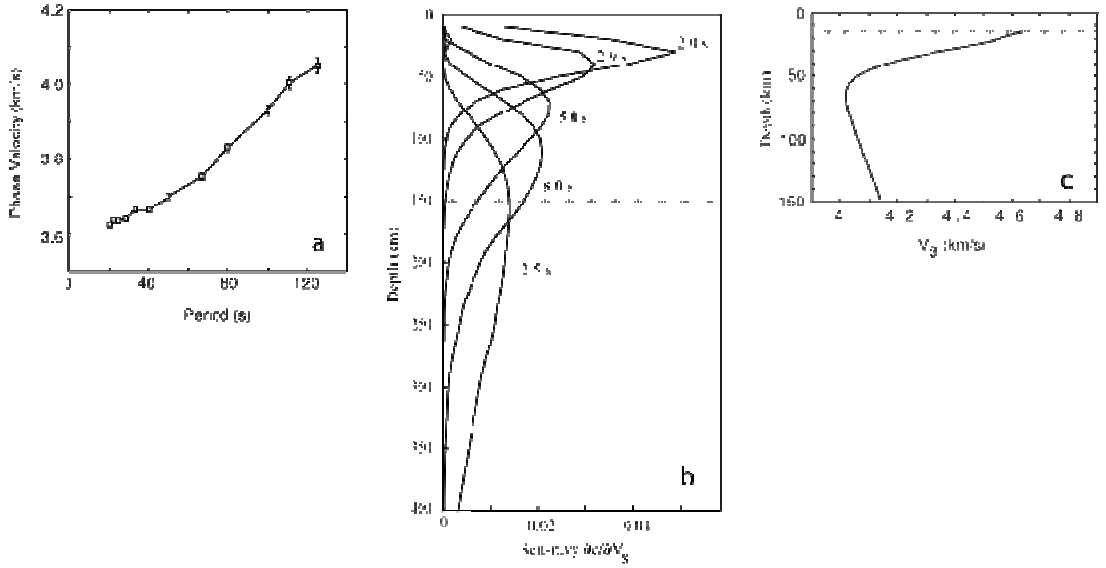

Fig. 4.6. Inversion for 1-D absolute V_S (Villagómez et al., 2007) a) 1-D dispersion curve (regional average) of Rayleigh wave phase velocity. b) Sensitivity kernels ($\partial c/\partial V_S$) for 20 s, 29s, 50s, 80s and 125 s period. Horizontal dashed line indicates maximum depth of good resolution. c) 1-D V_S model for the uppermost mantle between 15 km and 150 km depth. Horizontal dashed line represent bottom of the crust (15 km).

Fig. 4.6c shows the result of the inversion for the regional average V_S (1-D) as a function of depth (Villagómez et al., 2007). The seismic velocity within the oceanic crust was constrained in the inversion to velocities derived from a seismic reflection profile (Toomey et al., 2001), and was kept constant during the inversion. The horizontal dashed line in Fig. 4.6c represents the bottom of the crust in the model (15 km depth). The initial

mantle velocity model corresponds to a model constructed for a 1350°C mantle adiabat, 10 My-old lithosphere, and 2-mm grain size using the methodology described in Faul and Jackson (2005). A description of the resulting velocity model as well as a comparison with other oceanic regions and hotspots is discussed in Villagómez et al. (2007).

4.4.3. Joint Inversions for Slowness Perturbations

We performed a series of inversions for slowness perturbations with varying values of the weighting parameters. The tomographic method requires adjusting seven inversion parameters (λ_C, λ_P, λ_S, λ_{PS}, λ_H, λ_{ST} and λ_R from equation 4.7) and thus needs a significant amount of interaction from the user. The method allows for greater flexibility from the user perspective but at the potential cost of increased variability of the inversion results. The choice of inversion parameters need to be judicious to achieve the proper balance among the contributions of the different types of observations and also the importance of minimizing the data norm versus the model norm and smoothness. The final constraint is the geological plausibility of the resulting perturbational models.

We performed a large parameter search by varying the choice of inversion parameters and found a suitable range where the results are reasonably stable and geologically plausible. The inversion weights properly scale the relative importance of the different constraints with the a priori assumptions of model parameter uncertainty, observations uncertainties, relative size of partial derivatives of body and surface waves, and the relative size of the body and surface waves data sets. Unless noted otherwise, the

following figures show inversions using λ_C=40, λ_P=λ_S=λ_{ST}=λ_R=200, λ_H=5000 and λ_{PS}=10000.

The inversion also requires the choice of an initial slowness model to compute ray paths and predicted phase velocities. We used the 1-D V_S resulting from the inversion of the regional average Rayleigh wave dispersion curve (Fig. 4.6c). The result of each inversion is a slowness perturbation model, which we transform to velocity perturbation for inspection and display of the results.

Results of the joint tomography for S-wave slowness perturbation show low velocity anomalies that extend from the surface to the maximum depth of resolution (~300 km) (Fig. 4.7). Between 300 and 100 km depth the low-velocity anomaly tilts northward as it shoals; at 300 km depth it is centered ~75 km to the south of Isabela, whereas at 100 km depth it is centered beneath that island. This V_S anomaly reaches a magnitude of -2%. At depths between 200 and 300 km, the resolution of the anomaly is mainly constrained by the body wave delay time data. Fig. 4.4 consistently shows late arrivals for rays with piercing points at 400 km depth to the south of Isabela (between 0° and 2°S in latitude and between 92°W and 90.5°W in longitude), suggesting that the location of the anomaly is well resolved.

Between 50 and 100 km depth, V_S is higher-than-normal beneath southern Isabela, at the top of near-cylindrical low-velocity volume. The magnitude of this high shear-wave velocity anomaly recovered by the inversion is +1% (Fig. 4.7b and d). However, synthetic inversions show that the magnitude of a narrow (~50 km thick) high

velocity anomaly is difficult to resolve at these depths (Fig.4.1e–h), suggesting that the value of +1% may be an underestimation of the real magnitude of the anomaly.

Between 50 and 100 km depth, the low-velocity anomaly is located beneath the northeastern part of the archipelago (Fig. 4.7b), where the V_S anomaly has a magnitude of -1%. The depth of the anomaly is well constrained by the surface wave data (e.g., Fig. 4.5c). The lateral extent of the anomaly is well constrained inside the seismic array, but the northern end is less well constrained due to a decrease in the number of crossing Rayleigh wave paths outside of the seismic array (Villagómez et al., 2007). As recovered by the inversion, the low-velocity extends northward up to ~1°N (Fig. 4.7b).

At depths shallower than 50 km, the tomography detects a pronounced low-velocity anomaly (maximum V_S anomaly of -3%) beneath the southwestern part of the archipelago (Fig. 4.7a and d). This anomaly is resolved primarily by the surface wave data (e.g., Fig. 4.1a). The recovered lateral extent of this anomaly is ~200 km in the E-W direction, and ~100 km in the N-S direction. However, although its spatial extent is relatively well constrained to the north and east, it is less well constrained to the west and south outside of the seismic array.

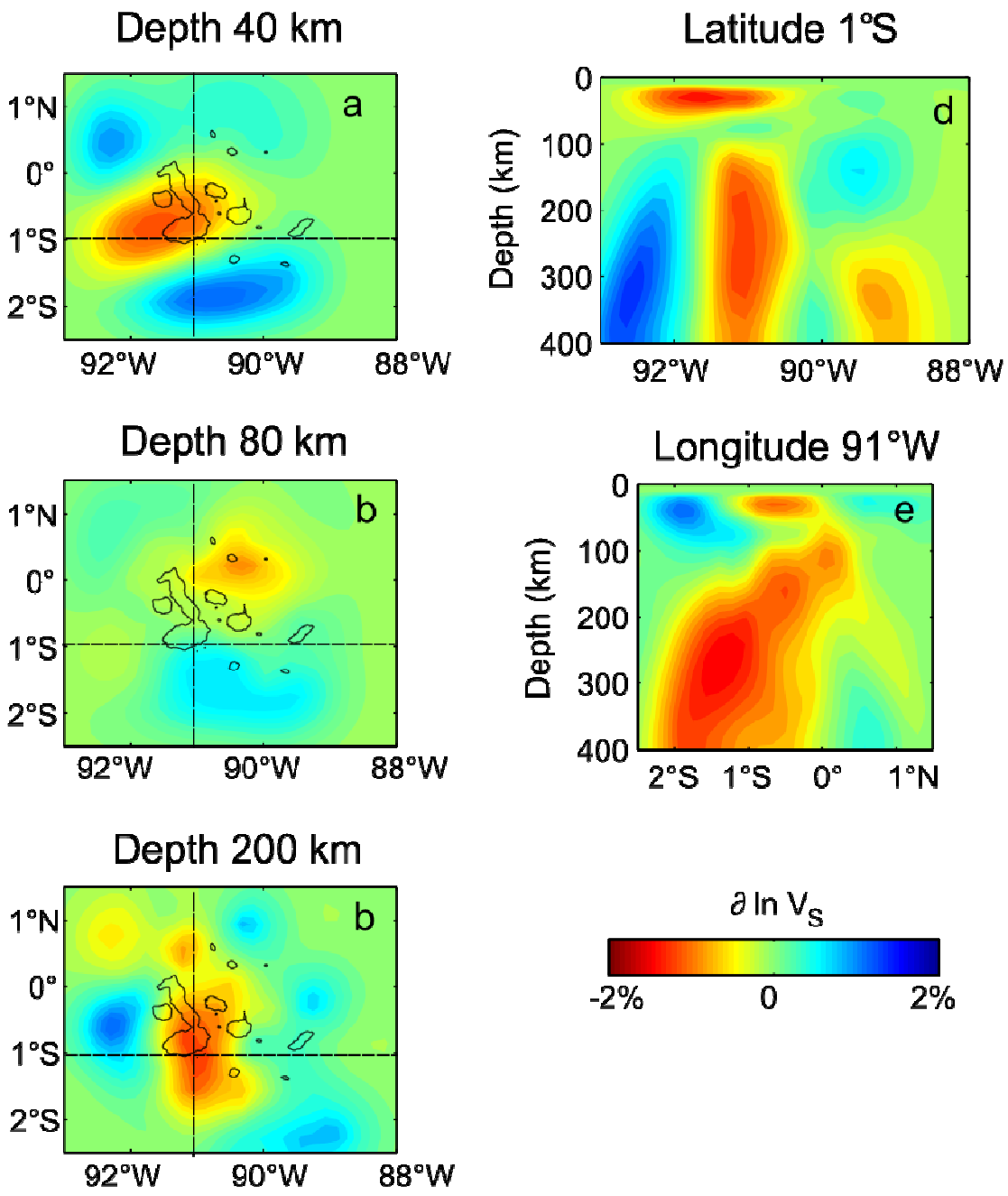

Fig. 4.7. Results of inversions for S-wave slowness perturbations. Color scale indicates estimated V_S anomalies. Map view cross-section at a) 40 km depth, b) 80 km depth and c) 200 km depth. d) W-E cross section at 1°S. e) S-N cross-section at 91°W. Dashed lines in (a-c) indicate locations of cross-sections d and e.

Results of inversions for P-wave and S-wave slowness perturbations are shown in Fig. 4.8. We performed inversions with no coupling between P and S waves (λ_{PS}=0) (Fig. 4.8 a-c). For this case, the result for S-wave perturbations (Fig. 4.8b) is equivalent to that of inversions for S-wave perturbations only (Fig. 4.7e). The result of the inversion for P-wave slowness (Fig. 4.8a) shows that the distribution of low V_P anomalies is roughly similar to that of V_S anomalies, with several distinctions. Between 100 and 300 km depth, both low V_P and V_S anomalies show the same northward tilt, but V_P appear to be higher than normal at 200 km depth, between 0° and 1°S (Fig. 4.8a), in a location where V_S appears to be lower than normal (Fig. 4.8b). This discrepancy appears as a region of higher than average V_P/V_S (Fig. 4.8c). In addition, between 50 km 100 km depth V_P appears to be lower than normal from 0° to 1°S (Fig. 4.8a), in contrast to the relatively higher than normal velocities observed for S-waves (Fig. 4.8b). This discrepancy occurs because the surface wave data, which resolves the higher than normal velocities at these depths, is coupled only with S-wave delay times and not with those of P-waves. Overall, the estimated magnitude of V_P anomalies seems to be about half of the magnitude of V_S anomalies.

Coupled P and S wave inversions using a smooth V_P/V_S constraint and λ_{PS}=10000 are shown in Fig. 4.8d-f. The results show that the location and magnitude of the velocity anomalies roughly match the results for the inversions with no coupling (Fig. 4.8a-c). One of the main differences between the 2 inversions is that the relatively high S-wave velocity volume observed in inversion with no coupling between 50 and 100 km depth (Fig. 4.8b) is less evident in the inversion with P-S coupling (Fig. 4.8e). This is caused by the decrease in influence of the surface wave data in the inversions, which is due to the

added coupling of P and S waves. A consistent element between these inversions is the relatively high V_P/V_S volume observed deeper than 100 km depth at around 1°S (Fig. 4.8f).

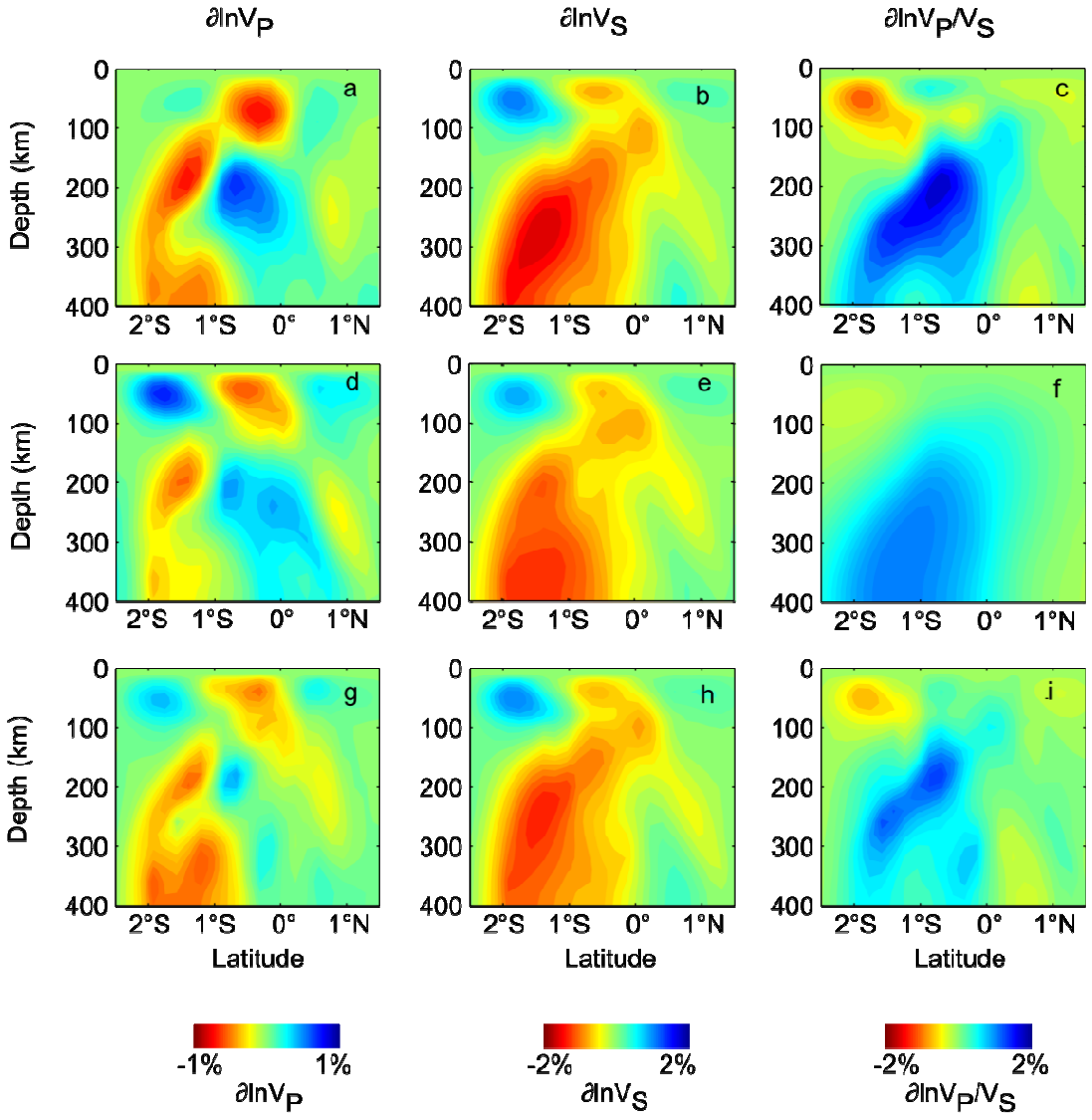

Fig. 4.8. Results of inversions for P-wave and S-wave slowness perturbations. S-N cross section at 91°W. (a-c) No P and S coupling, λ_{PS}=10000, (d-f) Smooth V_P/V_S, λ_{PS}=10000, (g-i) constant $\partial \ln V_P/\partial \ln V_S$=2.2, λ_{PS}=10000. (a,d and g) show $\partial \ln V_P$. (b,e and h) show $\partial \ln V_S$. (c,f and i) show $\partial \ln(V_P/V_S)$.

Coupled P and S wave inversions using a constant $\partial \ln V_P / \partial \ln V_S = 2.2$ and $\lambda_{PS} = 100000$ are shown in Fig. 4.8g-i. This type of constrain preserves the influence of the surface waves data better than the smooth V_P/V_S constrain, and thus the low V_S anomalies recovered shallower than 100-150 km depth (Fig. 4.8h) are similar to those of the inversions with no coupling (Fig. 4.8b). On the other hand, this constrain reduces the magnitude of the high V_P anomaly observed at 200 km depth between 0° and 1°S (Fig. 4.8g).

The results of all 3 inversions (no P-S coupling, smooth V_P/V_S constrain and constant $\partial \ln V_P / \partial \ln V_S$) show relatively high V_P/V_S values deeper than 100 km depth (Fig. 4.8c, f and h). This volume follows the shape of the low V_S volume, tilting northward with decreasing depth. The location of the high V_P/V_S volume is well constrained between 100 and 300 km depth by the third inversion (Fig.4.8i). On the other hand, the low V_S volume that appears above 50 km depth does not seem have a corresponding high V_P/V_S.

4.5. Discussion

The results of the joint inversion show low V_S anomalies extending from the surface to a depth of at least 300 km. Between 100 and 300 km depth the anomaly has a magnitude of -2% in V_S. We attribute this anomaly to an upwelling thermal mantle plume. We suggest that the velocity reduction represents a combination of increased temperatures and the presence of partial melt. Based solely on surface wave data,

Villagómez et al. (2007) inferred that the anomaly may represent excess temperature of 30 to 150 K.

This low-velocity volume tilts northward as it shoals. From 300 km to 100 km depth, the center of the anomaly shifts to the north by ~75 km. We attribute the northward tilt of the plume as it rises is due to background mantle flow toward the Galápagos Spreading Center. Some models of upwelling and melting of the Galápagos plume require that the plume tilts eastward to explain the distinct pattern of geochemical anomalies (Geist et al., 1988; White et al., 1993). However, we do not find evidence of eastward tilting of the plume in response to plate drag.

This low V_S volume also appears in coupled P-S inversions as a region with high V_P/V_S (e.g., Fig. 4.8i). We suggest that V_P/V_S anomalies may be a good representation of the upwelling mantle plume, and may outline the velocity anomalies better than just using V_S. $\partial \ln V_P/V_S$ can be thought of as a measurement of $\partial \ln V_S$ corrected by $\partial \ln V_P$, and thus it may provide a clearer image of velocity anomalies. However, with the current methodology we cannot explain the relative high V_P observed at 200 km depth (Fig. 4.8g), in the same region where V_S is lower than normal (Fig. 4.8h). A future study that incorporates the effects of seismic anisotropy on P and S delay times may clarify this discrepancy.

Based on analysis of receiver functions, Hooft et al. (2003) detected an anomalously thin transition zone beneath the Galápagos which is attributed to a mantle plume that is upwelling from depths greater than 410 km. This anomaly is consistent with an excess temperature of 130±60 K. Based on the location of the piercing points of the

seismic rays at the bottom of the transition zone (660 km), Hooft et al. (2003) inferred that the spatially averaged thickness of the transition zone is significantly less than normal centered at 91.7±0.8°W, 0.7±0.8°S. Given our present results, we place the center of the low V_S anomaly at 300 km depth at 91°W and 1°S (Fig 4.7c), about 70 km to the east from the receiver functions estimate (measured at 660 km depth). Our current estimate thus matches the one from receiver functions within the uncertainty boundaries.

Our results indicate that, immediately above this low-velocity region, at ~100 km depth, V_S increases abruptly. This velocity increase forms a relatively high-velocity volume that extends between 50 and 100 km depth beneath southern Isabela. The magnitude of the anomaly is not well constrained, but resolution tests suggest that the V_S increase may be larger than 1%. Regionally, we detect this high-velocity anomaly elsewhere beneath the archipelago. Its bottom is located at varying depths across the archipelago; it is deepest beneath the southern end of Isabela (~100 km depth) and it shoals to ~50 km towards the north and east. We refer to this volume as the high-velocity lid. We suggest that the base of this lid is anomalously thick beneath the southwestern archipelago and attribute this to residuum from melting above the upwelling mantle plume. By this view, the V_S increase represents a compositional change produced by the combined effects of depletion and dehydration resulting from melt extraction. Villagómez et al. (2007) discussed that depletion of peridotite can increase V_S up to 2.6% in the spinel stability field (Matsukage et al., 2005), while the removal of water (Karato, 1986; Hirth and Kohlstedt, 1996; Karato and Jung, 1998) can potentially increase V_S by 0.5% to 2% due to decreased anelasticity leading to lower attenuation of seismic waves. We suggest that effects of depletion and dehydration are greater at these depths than the

effects of increased temperature and partial melt. In addition, we suggest that the viscosity increase associated with such dehydration (Hirth and Kohlstedt, 1996) may decrease or stall mantle upwelling, resulting in lateral spreading of the plume beneath the lid.

Between 50 and 100 km depth the low-velocity anomaly is located beneath the northeastern part of the archipelago (Fig. 4.7b). We attribute this anomaly to melting produced as upwelling mantle spreads towards a region with a thinner lid. The depth of the anomaly is well constrained by the surface wave data (e.g., Fig. 4.1c). The inversion places the northern boundary of this anomaly at ~1°N. However, resolution of the surface waves is limited north of 1°N, and thus we suggest that the anomaly possibly extends farther north towards the spreading center.

Shallower than 50 km depth the low velocity anomaly is centered beneath the southwestern part of the archipelago (Fig. 4.7a and d). We attribute this anomaly to decompression melting associated with mantle upwelling that is driven by the buoyancy of the plume as well as by the spreading and thinning of the layer of buoyant residuum. The anomaly is centered near 91.7°W and 1°S, at the western edge of Isabela and ~50 km to the south of Fernandina (Fig. 4.7a). The inversion places the western boundary of this anomaly at ~92.5°W, but the lateral extent of the anomaly towards the west is not well constrained by the surface waves data.

In summary, the joint tomography reveals three distinct low-velocity regions that represent potential mantle melting zones. We suggest that the southwestern part of the archipelago taps 2 different melting zones: the main plume conduit at depths greater than

~100 km and a melting region that is shallower than ~50 km depth. The former region may represent decompression melting of hydrous or carbonated mantle peridotite (e.g., Dasgupta and Hirschmann, 2006). The latter may correspond to decompression melting of anhydrous mantle. In contrast the northeastern part of the archipelago taps only one melting region located at depths between ~50 and ~100 km depth.

CHAPTER V

CONCLUSIONS

We presented results of three different seismic tomography studies beneath the Galápagos Archipelago that image the three-dimensional seismic structure between 3 and 300 km depth. The tomographic images reveal an upwelling mantle plume that tilts northward (towards Galápagos Spreading Center) as it rises and that spreads laterally when it reaches the bottom of a high-viscosity lid. The lid, which we attribute to residuum from melting, is thickest away from the spreading center, suggesting that ridge processes may affect the generation and the amount of thinning of the residuum layer. In addition, the thickness of the lid correlates well with the geographical pattern of geochemical anomalies of erupted lavas, suggesting that the lid may influence the final depth of decompression melting. We conclude that many of the distinct characteristic of Galápagos compared to other oceanic hotspots, such as the broad geographical extent of recent volcanism and the unusual pattern of geochemical anomalies, can be attributed to the interaction of the upwelling plume with the lid and the nearby ridge.

5.1. Crustal Structure between 3 and 13 km Depth

We detected lateral variations in the seismic velocity of the crust beneath the Galápagos Archipelago from Rayleigh-wave group velocities derived from the cross-correlation of records of ambient seismic noise. Our results show that the lowest seismic velocities between 3 and 13 km depth are present beneath the western archipelago, suggesting that the crust in this region is warmer, contains more melt, and is more porous

than that beneath the eastern archipelago. The warmer crust lies above the inferred current locus of the Galápagos plume, suggesting that the temperature difference reflects increased magmatic activity and the injection of heat to shallow levels beneath the western archipelago. The west-to-east seismic velocity increase appears to be gradual and correlates well with distance downstream from the hotspot. We propose that the crustal velocity increase is the result of cooling and closing of pore volume.

On the basis of our results, which constrain the broad-scale thermal and chemical structure of the crust and lithosphere, as well as a synthesis of recent plate reconstructions and gravity data, we suggest that both the age of the lithosphere at the time of loading and its thickness and internal structure played major roles in shaping the location of hotspot volcanism and the morphology of volcanic landforms in the Galápagos Archipelago. Variations in the flexural response to loading in the Galápagos, which are correlated with volcano size and morphology, cannot be explained simply by the current thermal state of the lithosphere and more likely reflect varying lithospheric strength at the time of loading.

We attribute the northwest- and northeast-trending Darwinian lineaments that are found throughout the archipelago to pre-existing zones of weakness in the lithosphere. Such zones of weakness could have formed as pseudo-faults or wakes of OSCs during past episodes of ridge jumps and ridge propagation and then been reactivated more recently by stresses generated by plume-lithosphere interactions.

5.2. Mantle Structure between 20 and 300 km Depth

We obtained three-dimensional estimates of absolute shear-wave velocity (V_S) between 20 and 150 km depth from the inversion of Rayleigh-wave phase velocities measured at periods from 20 to 125 s. From these results we inferred the physical state of the uppermost mantle. We find a low-velocity asthenosphere at depths between 75 and 150 km depth. Shear wave velocities beneath the Galápagos are lower than those beneath other regions of comparable age in the Pacific and consistent with and excess temperature of 30 to 150°C and ~0.5% melt. We attribute the excess temperature and presence of melt to an upwelling thermal mantle plume. In addition, we find that the Galápagos hotspot is underlain by a high-velocity lid. Seismic velocities are anomalously high beneath the southwestern part of the archipelago at depths between 50 and ~75 km: they are 2.5% higher than those in the northeast, and higher than those of young regions in the Pacific (e.g., Nishimura and Forsyth, 1989). We attribute the high velocities to residuum from melting above the upwelling mantle plume, and suggest that the V_S increase represents a compositional change produced by the combined effects of depletion and dehydration resulting from melt extraction. We also suggest that the viscosity increase associated with such dehydration (Hirth and Kohlstedt, 1996) may decrease or stall mantle upwelling, resulting in lateral spreading of the plume beneath the lid.

Lastly, we obtained three-dimensional images of shear-wave velocity perturbations from the combination of Rayleigh wave phase velocity measurements and body wave delay time observations. The results reveal low-velocity anomalies extending from 20 to 300 km depth. Between 300 and 100 km depth the low-velocity anomaly is quasi-cylindrical with a radius of ~75 km, which we suggest represents the Galápagos

mantle plume. A pronounced low-velocity anomaly is seen at depths shallower than 50 km beneath the southwestern part of the archipelago that we attribute to a melting region produce by mantle upwelling caused by the buoyancy of the mantle plume as well as by the spreading and thinning of the layer of buoyant residuum.

These results also reveal a high-velocity anomaly beneath the southwestern part of the archipelago at depths between 50 and 100 km, which we term the high-velocity lid. This lid appears to be an important feature of the Galapagos mantle that affects the pattern of melting and upwelling of the plume. For instance, the thickness of the lid correlates well with the geographical pattern of geochemical anomalies or erupted lavas. We suggest that spatial variations in isotopic signatures of lavas can be attributed to differences in the amount of melting with depth associated with variations in the thickness of the lid. We also suggest that the thickness of the lid is affected by changes in plume-ridge separation and the interaction between the plume and ridge melting zones.

REFERENCES CITED

Allen, R. M., G. Nolet, W. J. Morgan, K. Vogfjord, B. H. Bergsson, P. Erlendsson, G. R. Foulger, S. Jakobsdottir, B. R. Julian, M. J. Pritchard, S. Ragnarsson, and R. Stefansson (2002), Imaging the mantle beneath Iceland using integrated seismological techniques, J. Geophys. Res., 107 (B12), 2325.

Asimow, P. D., and C. H. Langmuir (2003), The importance of water to oceanic mantle melting regimes, Nature, 421, 815-820.

Asimow, P. D., J. E. Dixon, and C. H. Langmuir (2004), A hydrous melting and fractionation model for mid-ocean ridge basalts: Application to the Mid-Atlantic Ridge near the Azores, Geochem. Geophys. Geosyst., 5, Q01E16.

Barckhausen U., C. R. Ranero, R. von Huene, S. C. Cande, and H. A. Roeser (2001) Revised tectonic boundaries in the Cocos plate off Costa Rica: Implications for the segmentation of the convergent margin and for plate tectonic models, J. Geophys. Res., 106, 19,207-19,220.

Canales, J. P., R. S. Detrick, and D. R. Toomey (2003), Segment-scale variations in the crustal structure of 150-300 kyr old fast spreading oceanic crust (East Pacific Rise, 8º15'N-10º5'N) from wide-angle seismic refraction profiles, Geophys. J. Int., 152, 766-794.

Carbotte, S. M., and K. C. Macdonald (1992), East Pacific Rise 8º-10º30'N: Evolution of ridge segments and discontinuities from SeaMARC II and three-dimensional magnetic studies, J. Geophys. Res., 97, 6959-6982.

Carlson, R. L., and C. N. Herrick (1990), Densities and porosities in the oceanic crust and their variations with depth and age, J. Geophys. Res., 95, 9153-9170.

Christensen, N. I. (1984), The magnitude, symmetry and origin of upper mantle anisotropy based on fabric analyses of ultramafic tectonites, Geophys. J. Roy. Astron. Soc., 76, 89-111.

Darwin, C. (1860), The Voyage of the Beagle, Random House USA, New York, NY, 496 pp.

Dasgupta, R. and M.M. Hirschmann (2006) Melting in the Earth's deep upper mantle caused by carbon dioxide, Nature, 440, 659-662.

DeMets, C., R. G. Gordon, D. F. Argus, and S. Stein (1994), Effect of recent revisions to the geomagnetic reversal time scale on estimates of current plate motions, Geophys. Res. Lett., 21, 2191-2194.

Detrick, R. S., and S. T. Crough (1978), Island subsidence, hot spots, and lithospheric thinning, J. Geophys. Res., 83, 1236-1244.

Detrick, R., J. Collins, R. Stephen, and S. Swift (1994), In situ evidence for the nature of the seismic layer 2/3 boundary in oceanic crust, Nature, 370, 288-290.

Detrick, R. S., J. M. Sinton, G. Ito, J. P. Canales, M. Behn, T. Blacic, B. Cushman, J. E. Dixon, D. W. Graham, and J. J. Mahoney (2002), Correlated geophysical, geochemical, and volcanological manifestations of plume-ridge interaction along the Galápagos Spreading Center, Geochem. Geophys. Geosyst., 3 (10), 8501.

Dijkstra, E.W. (1959) A note on two problems in connection with graphs, Numer. Math., 1, 269-271.

Ding, X., and S. P. Grand (1993), Upper mantle Q structure beneath the East Pacific Rise, J. Geophys. Res., 98, 1973-1985.

Dunn, R. A., V. Lekić, R. S. Detrick, and D. R. Toomey (2005), Three-dimensional seismic structure of the Mid-Atlantic Ridge (35°N): Evidence for focused melt supply and lower crustal dike injection, J. Geophys. Res., 110, B09101.

Dziewonski, A., S. Bloch, and M. Landisman (1969), A technique for the analysis of transient seismic signals, Bull. Seism. Soc. Am., 59, 427-444.

Dziewonski, A. M., and D. L. Anderson (1981), Preliminary reference Earth model, Phys. Earth Plan. Inter., 25, 297-356.

Evans, R. L., G. Hirth, K. Baba, D. Forsyth, A. Chave, and R. Mackie (2005), Geophysical evidence from the MELT area for compositional controls on oceanic plates, Nature, 437, 249-252.

Farnetani, C. G., B. Legras, and P. J. Tackley (2002), Mixing and deformations in mantle plumes, Earth Planet. Sci. Lett., 196, 1-15.

Faul, U. H. (2001), Melt retention and segregation beneath mid-ocean ridges, Nature, 410, 920-923.

Faul, U. H., and I. Jackson (2005), The seismological signature of temperature and grain size variations in the upper mantle, Earth Planet. Sci. Lett., 234, 119-134.

Feighner, M. A., and M. A. Richards (1994), Lithospheric structure and compensation mechanisms of the Galápagos archipelago, J. Geophys. Res., 99, 6711-6729.

Feighner, M. A., and M. A. Richards (1995), The fluid dynamics of plume-ridge and plume-plate interactions: An experimental investigation, Earth Planet. Sci. Lett., 129, 171-182.

Fontaine, F. R., E. E. E. Hooft, P. G. Burkett, D. R. Toomey, S. C. Solomon, and P. G. Silver (2005), Shear-wave splitting beneath the Galápagos archipelago, Geophys. Res. Lett., 32, L21308, doi:10.1029/2005GL024014.

Forsyth, D. W., and A. Li (2005), Array analysis of two-dimensional variations in surface wave phase velocity and azimuthal anisotropy in the presence of multipathing interference, in Seismic Earth: Array Analysis of Broadband Seismograms, edited by A. Levander and G. Nolet, Geophysical Monograph 157, pp. 81-97, AGU, Washington, DC.

Forsyth, D. W., S. C. Webb, L. M. Dorman, and Y. Shen (1998), Phase velocities of Rayleigh waves in the MELT experiment on the East Pacific Rise, Science, 280, 1235-1238.

Friedrich A., F. Krüger F., and K. Klinge (1998), Ocean-generated microseismic noise located with the Gräfenberg array, J. Seism., 2, 47-64.

Gaherty, J. B., T. H. Jordan, and L. S. Gee (1996), Seismic structure of the upper mantle in a central Pacific corridor, J. Geophys. Res., 101, 22291-22310.

Geist, D. J., W. M. White, and A. R. McBirney (1988), Plume-asthenosphere mixing beneath the Galapagos archipelago, Nature, 333, 657-660.

Geist, D. J., T. R. Naumann, and P. Larson (1998), Evolution of Galápagos magmas: Mantle and crustal fractionation without assimilation, J. Petrol., 39, 953-971.

Geist, D. J., T. R. Naumann, J. J. Standish, M. D. Kurz, K. S. Harpp, W. M. White, and D. J. Fornari (2005), Wolf Volcano, Galápagos Archipelago: Melting and magmatic evolution at the margins of a mantle plume, J. Petrol., 46, 2197-2224.

Granet, M., M. Wilson, and U. Achauer (1995), Imaging a mantle plume beneath the French Massif Central, Earth Planet. Sci. Lett., 136, 281-296.

Grevemeyer, I., and W. Weigel (1997), Increase of seismic velocities in upper oceanic crust: The “superfast” spreading East Pacific Rise at 14°14'S, Geophys. Res. Lett., 24, 217-220.

Gripp, A. E., and R. G. Gordon (2002), Young tracks of hotspots and current plate velocities, Geophys. J. Int., 150, 321-361.

Gu, Y. J., S. C. Webb, A. Lerner-Lam, and J. B. Gaherty (2005), Upper mantle structure beneath the eastern Pacific Ocean ridges, J. Geophys. Res., 110, B06305.

Hammond, W. C., and E. D. Humphreys (2000), Upper mantle seismic wave velocity: Effects of realistic partial melt geometries, J. Geophys. Res., 105, 10,975-10,986.

Hammond, W. C., and D. R. Toomey (2003), Seismic velocity anisotropy and heterogeneity beneath the Mantle Electromagnetic and Tomography Experiment (MELT) region of the East Pacific Rise from analysis of P and S body waves, J. Geophys. Res., 109 (B4).

Harpp, K. S., and D. J. Geist (1998), Galápagos plumology, Noticias de Galápagos, 59, 23-28.

Harpp, K. S., and W. M. White (2001), Tracing a mantle plume: Isotopic and trace element variations of Galapagos seamounts, Geochem. Geophys. Geosyst., 2 (6), doi:10.1029/2000GC000137.

Harpp, K. S., and D. J. Geist (2002), Wolf–Darwin lineament and plume–ridge interaction in northern Galápagos, Geochem. Geophys. Geosyst., 3 (11), 8504, doi:10.1029/2002GC000370.

Hauff, F., K. Hoernle, H.-U. Schmincke, and R. Werner (1997), A mid Cretaceous origin for the Galápagos hotspot: Volcanological, petrological and geochemical evidence from Costa Rican oceanic crustal segments, Int J. Earth Sci. (Geologische Rundschau), 86, 141-155.

Herrmann, R., and C. Ammon (2004), Computer Programs in Seismology, Saint Louis University, St. Louis, http://www.eas.slu.edu/People/RBHerrmann/CPS330.html.

Hey, R. (1977), Tectonic evolution of the Cocos-Nazca spreading center, Geol. Soc. Am. Bull., 88, 1404-1420.

Hirth, G., and D. L. Kohlstedt (1996), Water in the oceanic upper mantle: Implications for rheology, melt extraction and the evolution of the lithosphere, Earth Planet. Sci. Lett., 144, 93-108.

Hirth, G., and D. L. Kohlstedt (2003), Rheology of the upper mantle and the mantle wedge: A view from experimentalists, in Inside the Subduction Factory, edited by J. M. Eiler, Geophysical Monograph 138, pp. 83-105, AGU, Washington, D.C.

Hoernle, K., R. Werner, J. Phipps Morgan, D. Garbe-Schönberg J. Bryce, and J. Mrazek (2000), Existence of complex spatial zonation in the Galapagos plume for at least 14 m.y., Geology, 28, 435-438.

Hoernle, K., P. van den Bogaard, R. Werner, B. Lissinna, F. Hauff, G. Alvarado, and D. Garbe-Schönberg (2002), Missing history (16–71 Ma) of the Galápagos hotspot: Implications for the tectonic and biological evolution of the Americas, Geology, 30, 795-798.

Hooft, E. E. E., D. R. Toomey, and S. C. Solomon (2003), Anomalously thin transition zone beneath the Galápagos hotspot, Earth Planet. Sci. Lett., 216, 55-64.

Ito, G., J. Lin, and C. W. Gable (1997), Interaction of mantle plumes and migrating mid-ocean ridges: Implications for the Galapagos plume-ridge system, J. Geophys. Res., 102, 15,403-15,417.

Ito, G., Y. Shen, G. Hirth, and C. J. Wolfe (1999), Mantle flow, melting, and dehydration of the Iceland mantle plume, Earth Planet. Sci. Lett., 165, 81-96.

Ito, G., J. Lin, and D. Graham (2003), Observational and theoretical studies of the dynamics of mantle plume-mid-ocean ridge interaction, Rev. Geophys., 41 (4), 1017.

Jackson D. D. (1979), The use of a priori data to resolve non-uniqueness in linear inversion, Geophys. J. Royal Astronomical Soc., 57 (1), 137-157.

Jackson, I., M. S. Paterson, and J. D. FitzGerald (1992), Seismic wave dispersion and attenuation in Aheim dunite, Geophys. J. Int., 108, 517-534.

Jordan, T. H. (1979), Mineralogies, densities and seismic velocities of garnet lherzolites and their geophysical implications, in The Mantle Sample: Inclusions in Kimberlites and Other Volcanics, edited by F. R. Boyd, and H. O. A. Meyer, pp. 1-19, AGU, Washington, D.C.

Karato, S. (1986), Does partial melting reduce the creep strength of the upper mantle?, Nature, 319, 309-310.

Karato, S. (1993), Importance of anelasticity in the interpretation of seismic tomography, Geophys. Res. Lett., 20, 1623-1626.

Karato, S. (2003), Mapping water content in the upper mantle, in Inside the Subduction factory, edited by J. M. Eiler, Geophysical Monograph 138, pp. 135-152, AGU, Washington, D.C.

Karato, S., and H. Jung (1998), Water, partial melt and the origin of the seismic low velocity and high attenuation zone in the upper mantle, Earth Planet. Sci. Lett., 157, 193-207.

Kennett B.L.N. and E.R. Engdahl (1991), Traveltimes for global earthquake location and phase identification, Geoph. J. Int., 105 (2), 429-465.

Kerr, R. C., and C. Mériaux (2004), Structure and dynamics of sheared mantle plumes, Geochem. Geophys. Geosyst., 5, Q12009, doi:10.1029/2004GC000749.

Kincaid, C., G. Ito, and C. Gable (1995), Laboratory investigation of the interaction of off-axis mantle plumes and spreading centers, Nature, 376, 758-761.

Klein, F. W. (1981), A linear gradient crustal model for south Hawaii, Bull, Seism. Soc. Am., 71, 1503-1510.

Kurz, M. D., and D. Geist (1999), Dynamics of the Galapagos hotspot from helium isotope geochemistry, Geochim. Cosmochim. Acta, 63, 4139-4156.

Langmuir, C. H., E. M. Klein, and T. Plank (1992), Petrological systematics of mid-ocean ridge basalts: Constraints on melt generation beneath ocean ridges, in Mantle Flow and Melt Generation at Mid-Ocean Ridges, edited by J. Phipps Morgan, D. K. Blackman, and J. M. Sinton, Geophysical Monograph 71, pp. 183-280, AGU, Washington, D.C.

Larose, E., A. Derode, M. Campillo, and M. Fink (2004), Imaging from one-bit correlations of wideband diffuse wave fields, J. Appl. Phys., 95, 8393–8399.

Larson, E. W. F., and G. Ekström (2002), Determining surface wave arrival angle anomalies, J. Geophys. Res., 107 (B6), 2127.

Li, A., and R. S. Detrick (2003), Azimuthal anisotropy and phase velocity beneath Iceland: Implication for plume-ridge interaction, Earth Planet. Sci. Lett., 214, 153-165.

Li, A., and R. S. Detrick (2006), Seismic structure of Iceland from Rayleigh wave inversions and geodynamic implications, Earth Planet. Sci. Lett., 241, 901-912.

Li, A., D. W. Forsyth, and K. M. Fischer (2003), Shear velocity structure and azimuthal anisotropy beneath eastern North America from Rayleigh wave inversion, J. Geophys. Res., 108 (B8), 2362.

Lonsdale, P., and K. D. Klitgord (1978), Structure and tectonic history of the eastern Panama Basin, Geol. Soc. Am. Bull., 89, 981–999.

Lundstrom, C. C., J. Gill, Q. Williams, and M. R. Perfit (1995), Mantle melting and basalt extraction by equilibrium porous flow, Science, 270, 1958-1961.

Lyons, J., D. Geist, K. Harpp, B. Diefenbach, P. Olin, and J. Vervoort (2007), Crustal growth by magmatic overplating in the Galápagos, Geology, 35, 511-514.

Malcolm, A. E., J. A. Scales, and B. A. van Tiggelen B. A. (2004), Extracting the Green function from diffuse, equipartitioned waves, Phys. Rev., 70, 015601.

Matsukage, K. N., Y. Nishihara, and S. Karato (2005), Seismological signature of chemical differentiation of Earth's upper mantle, J. Geophys. Res., 110, B12305.

McBirney, A. R., and H. Williams (1969), Geology and Petrology of the Galápagos Islands, Memoir 118, 197 pp., Geological Society of America, Boulder, Colo.

McKenzie, D., and M. J. Bickle (1988), The volume and composition of melt generated by extension of the lithosphere, J. Petrol., 29, 625-679.

Meschede, M., and U. Barckhausen (2000), Plate tectonic evolution of the Cocos-Nazca spreading center, in Proc. ODP, Sci. Results, 170, edited by E. A. Silver, G. Kimura, and T. H. Shipley, Ocean Drilling Program, College Station, Tex., pp. 1–10.

Metropolis, N., and S. Ulam (1949), The Monte Carlo method, J. Amer. Statist. Assoc., 44, 335–341.

Mittelstaedt E., and G. Ito (2005), Plume-ridge interaction, lithospheric stresses, and the origin of near-ridge volcanic lineaments, Geochem. Geophys. Geosyst., 6, Q06002, doi:10.1029/2004GC000860.

Montagner, J. P., and T. Tanimoto (1990), Global anisotropy in the upper mantle inferred from the regionalization of phase velocities, J. Geophys. Res., 95, 4797–4819.

Morgan, W. J. (1971), Convection plumes in the lower mantle, Nature, 230, 42-43.

Morgan W. J. (1972), Deep mantle convection plumes and plate motions, Bull. Am. Assoc. Petrol. Geol., 56, 617-618.

Mosegaard, K., and A. Tarantola (1995), Monte Carlo sampling of solutions to inverse problems. J. Geophys. Res., 100, 12431-12447.

Moser, T.J. (1991), Shortest path calculation of seismic rays, Geophysics, 56, 59-67.

Nedimović, M. R., D. R. Bohnenstiehl, S. M. Carbotte, J. P. Canales, and R. P. Dziak (2009), Faulting and hydration of the Juan de Fuca plate system, Earth Planet. Sci. Lett., 284, 94-102.

Nishimura, C. E., and D. W. Forsyth (1988), Rayleigh wave phase velocities in the Pacific with implications for azimuthal anisotropy and lateral heterogeneities, Geophys. J., 94, 479-501.

Nishimura, C. E., and D. W. Forsyth (1989), The anisotropic structure of the upper mantle in the Pacific, Geophys. J. Roy. Astron. Soc., 96, 203-229.

Phipps Morgan, J., W. J. Morgan, and E. Price (1995), Hotspot melting generates both hotspot volcanism and a hotspot swell?, J. Geophys. Res., 100, 8045-8062.

Press, W. H., S. A. Teukolsky, W. T. Vetterling, and B. P. Flannery (1992), Numerical Recipes in FORTAN: The Art of Scientific Computing, 2nd ed., 963 pp., Cambridge Univ. Press, New York.

Priestley, K., and F. Tilmann (1999), Shear-wave structure of the lithosphere above the Hawaiian hot spot from two-station Rayleigh wave phase velocity measurements, Geophys. Res. Lett., 26, 1493-1496.

Ribe, N. M. (1996), The dynamics of plume-ridge interaction: 2. Off-ridge plumes, J. Geophys. Res., 101, 16,195-16,204.

Ribe, N. M., and U. R. Christensen (1994), Three-dimensional modeling of plume-lithosphere interaction, J. Geophys. Res., 99, 669-682.

Ribe, N. M., and U. R. Christensen (1999), The dynamical origin of Hawaiian volcanism, Earth Planet. Sci. Lett., 171, 517-531.

Ribe, N. M., and W. L. Delattre (1998), The dynamics of plume-ridge interaction - III. The effects of ridge migration, Geophys. J. Int., 133, 511-518.

Richards, M. A., and R. M. Griffiths (1999), Thermal entrainment by deflected mantle plumes, Nature, 342, 900-902.

Ritter, J. R. R., M. Jordan, U. R. Christensen, and U. Achauer (2001), A mantle plume below the Eifel volcanic fields, Germany, Earth Planet. Sci. Lett., 186, 7-14.

Ritzwoller, M. H., N. M. Shapiro, M P. Barmin, and A. L. Levshin (2002), Global surface wave diffraction tomography, J. Geophys. Res., 107(B12), 2335.

Sabra, K. G., P. Gerstoft, P. Roux, W. A. Kuperman, and M. C. Fehler (2005), Extracting time-domain Green's function estimates from ambient seismic noise, Geophys. Res. Lett., 32, L03310.

Saito, M. (1988), DISPER80: A subroutine package for calculation of seismic normal-mode solutions, in Seismological Algorithms; Computational Methods and Computer Programs, edited by D. J. Doornbos, pp. 293-319, Academic Press, San Diego, Calif.

Sallarés, V., P. Charvis, E. R. Flueh, J. Bialas, and the SALIERI Scientific Party (2005), Seismic structure of the Carnegie Ridge and the nature of the Galápagos hotspot, Geophys. J. Int., 161, 763– 788.

Sandwell, D. T., and W. H. F. Smith (1997), Marine gravity from Geosat and ERS 1 satellite altimetry, J. Geophys. Res., 102, 10039–10054, doi:10.1029/96JB03223.

Schilling, J. G. (1991), Fluxes and excess temperatures of mantle plumes inferred from their interaction with migrating mid-ocean ridges, Nature, 352, 397-403.

Schilling, J. G., R. H. Kingsley, and J. D. Devine (1982), Galapagos hot spot-spreading center system; 1, Spatial petrological and geochemical variations (83°W-101°W), J. Geophys. Res., 87, 5593-5610.

Schilling, J. G., D. Fontignie, J. Blichert-Toft, R. Kingsley, and U. Tomza (2003), Pb-Hf-Nd-Sr isotope variations along the Galápagos Spreading Center (101°-83°W): Constraints on the dispersal of the Galápagos mantle plume, Geochem. Geophys. Geosyst., 4 (10), 8512, doi:10.1029/2002GC000495.

Schubert, G., D. L. Turcotte, and P. Olson (1991), Mantle Convection in the Earth and Planets, 940 pp., Cambridge Univ. Press, New York.

Shapiro, N. M., and M. Campillo (2004), Emergence of broadband Rayleigh waves from correlations of the ambient seismic noise, Geophys. Res. Lett.., 31, L07614.

Shapiro, N. M., M. Campillo, L. Stehly, and M. Ritzwoller (2005), High-resolution surface wave tomography from ambient seismic noise, Science, 307, 1615-1618.

Shaw, P. R. (1994), Age variations of oceanic crust Poisson's ratio: Inversion and a porosity evolution model, J. Geophys. Res., 99, 3057-3966.

Simkin, T., and L. Siebert (1994), Volcanoes of the World; A Regional Directory, Gazetteer, and Chronology of Volcanism during the Last 10,000 Years, 349 pp., Geoscience Press, Tucson, Ariz.

Sinton, C. W., D. M. Christie, and R. A. Duncan (1996), Geochronology of Galápagos seamounts, J. Geophys. Res., 101(B6), 13,689–13,700, doi:10.1029/96JB00642.

Sinton J., R. Detrick, J. P. Canales, G. Ito, and M. Behn (2003), Morphology and segmentation of the western Galápagos Spreading Center, 90.5°–98°W: Plume-ridge interaction at an intermediate spreading ridge, Geochem. Geophys. Geosyst., 4(12), 8515.

Sleep, N. H. (1990), Hotspots and mantle plumes: Some phenomenology, J. Geophys. Res., 95, 6715-6736.

Sleep, N. H. (1996), Lateral flow of hot plume material ponded at sublithospheric depths, J. Geophys. Res., 101, 28,065-28,083.

Smith, M. L., and F. A. Dahlen (1973), The azimuthal dependence of Love and Rayleigh wave propagation in a slightly anisotropic medium, J. Geophys. Res., 78, 3321-3333.

Spudich, P., and J. Orcutt (1980) A new look at the seismic velocity structure of the oceanic crust, Rev. Geophys., 18, 3, 627-645.

Tarantola, A., and B. Valette (1982), Generalized nonlinear inverse problems solved using the least squares criterion, Rev. Geophys., 20, 219-232.

ten Brink U. S., and T. M. Brocher (1987), Multichannel seismic evidence for a subcrustal intrusive complex under Oahu and a model for Hawaiian volcanism, J. Geophys. Res., 92, 13,687-13,707.

Tikhonov, A. N. (1943), On the stability of inverse problems, Dokl. Akad. Nauk SSSR, 39 (5), 195-198.

Tilmann, F. J. (1999), The seismic structure of the upper mantle beneath Hawaii, Ph.D. thesis, Queens' College, Cambridge.

Toomey D.R., S.C. Solomon and G.M. Purdy (1994) Tomographic imaging of the shallow crustal structure of the East Pacific Rise at 9°30'N, J. Geophys. Res., 99 (B12), 24135-24157.

Toomey, D. R., E. E. E. Hooft, and R. S. Detrick (2001), Crustal thickness variations and internal structure of the Galápagos Archipelago, Eos Trans. AGU, 82 (47), Fall Meeting Suppl., Abstract T42B-0939.

Toomey, D. R., E. E. E. Hooft Toomey, S. C. Solomon, D. E. James, and M. L. Hall (2002a), Seismic evidence for a plume beneath the Galápagos hotspot, Eos Trans. AGU, 83 (47), Fall Meet. Suppl., Abstract S72C-02.

Toomey, D. R., W. S. D. Wilcock, J. A. Conder, D. W. Forsyth, J. D. Blundy, E. M. Parmentier, and W. C. Hammond (2002b), Asymmetric mantle dynamics in the MELT region of the East Pacific Rise, Earth Planet. Sci. Lett., 200, 287-295.

Turcotte, D. L., and G. Schubert (2002), Geodynamics, 2nd ed., 456 pp., Cambridge University Press, New York.

VanDecar J.C. and R.S. Crosson (1990), Determination of teleseismic phase arrival times using multi-channel cross-correlation and least squares, Bull. Seism. Soc. Am., 80 (1), 150-169.

Vera, E. E., J. C. Mutter, P. Buhl, J. A. Orcutt, A. J. Harding, M. E. Kappus, R. S. Detrick, and T. M. Brocher (1990), The structure of 0- to 0.2-m.y.-old oceanic crust at 9°N on the East Pacific Rise from expanded spread profiles, J. Geophys. Res., 95, 15,529–15,556, doi:10.1029/JB095iB10p15529.

Verma, S. P., and J.-G. Schilling (1982), Galapagos hot spot-spreading center system, 2. $^{87}Sr/^{86}Sr$ and large ion lithophile element variations (85°W-101°W), J. Geophys. Res., 87, 10,838-10,856.

Vidale, J. E. (1986), Complex polarization analysis of particle motion, Bull. Seismol. Soc. Am., 76, 1393-1405.

Villagómez D. R., D. R. Toomey, E. E. E. Hooft, and S. C. Solomon S. C. (2007), Upper mantle structure beneath the Galápagos Archipelago from surface wave tomography, J. Geophys. Res., 112, B07303.

Watts, A. B., and U. S. ten Brink (1989), Crustal structure, flexure, and subsidence history of the Hawaiian Islands, J Geophys Res, 94, 10,473-10,500.

Watts, A. B., and S. Zhong (2002), Observations of flexure and the rheology of oceanic lithosphere, Geophys, J. Int., 142, 855-875.

Watts, A. B., U. S. ten brink, P. Buhl, and T. M. Brocher (1985), A multichannel seismic study of lithospheric flexure across the Hawaiian–Emperor seamount chain, Nature, 315, 105-111.

Weeraratne, D. S., D. W. Forsyth, K. M. Fischer, and A. A. Nyblade (2003), Evidence for an upper mantle plume beneath the Tanzanian craton from Rayleigh wave tomography, J. Geophys. Res., 108 (B9), 2427, doi:10.1029/2002JB002273.

Weeraratne, D. S., D. W. Forsyth, Y. Yang, and S. C. Webb (2007), Rayleigh wave tomography beneath intraplate volcanic ridges in the South Pacific, J. Geophys. Res., submitted.

Werner, R., K. Hoernle, P. van der Bogaard, C. Ranero, R. von Huene and D. Korich (1999), Drowned 14-m.y.-old Galápagos archipelago off the coast of Costa Rica: Implications for tectonic and evolutionary models, Geology, 27, 499-502.

Werner, R., K. Hoernle, U. Barkckhausen, and F. Hauff (2003), Geodynamic evolution of the Galápagos hot spot system (Central East Pacific) over the past 20 m.y.: Constraints from morphology, geochemistry, and magnetic anomalies, Geochem. Geophys. Geosyst., **4**(12), 1108, doi:10.1029/2003GC000576.

White, R. S., and D. McKenzie (1995), Mantle plumes and flood basalts, J. Geophys. Res., 100, 17,543-17,586.

White, R. S., D. McKenzie, and R. K. O'Nions (1992), Oceanic crustal thickness from seismic measurements and rare earth element inversions, J. Geophys. Res., 97, 19,683-19,715.

White, W. M., and A. W. Hofmann (1978), Geochemistry of the Galapagos Islands: Implications for mantle dynamics and evolution, in Year Book 77, pp. 596-606, Carnegie Institution of Washington, Washington, D.C.

White, W. M., A. R. McBirney, and R. A. Duncan (1993), Petrology and geochemistry of the Galapagos Islands; portrait of a pathological mantle plume, J. Geophys. Res., 98, 19,533-19,563.

Wiggins, R.A. (1972) The general linear inverse problem: Implication of surface waves and free oscillations for Earth structure, Rev. Geophys., 10, 251-285.

Wilcock W. S. D., S. C. Solomon, G. M. Purdy, and D. R. Toomey (1995), Seismic attenuation structure of the East Pacific Rise near 9°30'N, J. Geophys. Res., 100, 24147-24166.

Wilson, D. S., and R. N. Hey (1995), History of rift propagation and magnetization intensity for the Cocos-Nazca spreading center, J. Geophys. Res., 100, 10,041-10,056.

Wolfe, C. J., I. T. Bjarnason, J. C. VanDecar, and S. C. Solomon (1997), Seismic structure of the Iceland mantle plume, Nature, 385, 245-247.

Wolfe, C. J., and S. C. Solomon (1998), Shear-wave splitting and implications for mantle flow beneath the MELT region of the East Pacific Rise, Science, 280, 1230-1232.

Wolfe, C.J., S.C. Solomon, G. Laske, J. A. Collins, R.S. Detrick, J. A. Orcutt, D. Bercovici and E.H.Hauri (2009), Mantle shear-wave velocity structure beneath the Hawaiian hot spot, Science, 326 (5958), 1388-1390.

Yale, M. M., and J. Phipps Morgan (1998), Asthenosphere flow model of hotspot-ridge interactions: A comparison of Iceland and Kerguelen, Earth Planet. Sci. Lett., 161, 45-56.

Yang, Y., and D. W. Forsyth (2006), Regional tomographic inversion of the amplitude and phase of Rayleigh waves with 2-D sensitivity kernels, Geophys. J. Int., 166, 1148-1160.

Yang Y., D. W. Forsyth, and D. S. Weeraratne (2007) Seismic attenuation near the East Pacific Rise and the origin of the low-velocity zone, Earth Planet. Sci. Lett., submitted.

Zhou, Y., F. A. Dahlen, and G. Nolet (2004), Three-dimensional sensitivity kernels for surface wave observables, Geophys. J. Int., 158, 142-168.